SPIN PHYSICS IN THE AGE OF QUANTUM SIMULATION: FROM EMERGENCE TO CHAOS

by

Bilal Khalid

A Dissertation

Submitted to the Faculty of Purdue University

In Partial Fulfillment of the Requirements for the degree of

Doctor of Philosophy

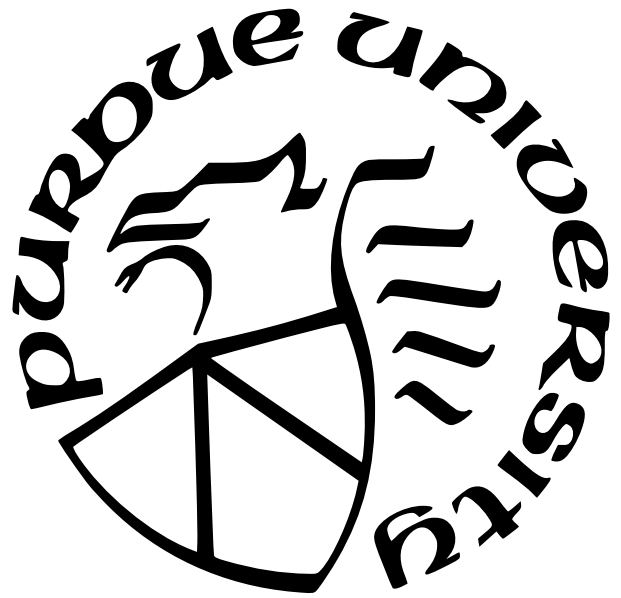

Department of Physics and Astronomy

West Lafayette, Indiana

August 2025

THE PURDUE UNIVERSITY GRADUATE SCHOOL
STATEMENT OF COMMITTEE APPROVAL

Dr. Sabre Kais (Co-chair)

Department of Electrical and Computer Engineering,

North Carolina State University

Dr. Nima Lashkari (Co-chair)

Department of Physics and Astronomy

Dr. David D. Nolte

Department of Physics and Astronomy

Dr. Jukka Vayrynen

Department of Physics and Astronomy

Dr. Nicolas Gisin

Department of Applied Physics,

University of Geneva

Approved by:

Dr. Gabor A. Csathy

To my parents

ACKNOWLEDGMENTS

بِسْمِ ٱللَّهِ ٱلرَّحْمَٰنِ ٱلرَّحِيمِ

In the Name of Allah — the Most Compassionate, Most Merciful.

First of all, the greatest gratitude I owe to anyone besides God Almighty for anything I am able to do in my life is to my parents. It is only their sacrifices and lifelong struggles that have enabled me to stand on my own two feet with dignity. For my Ph.D. in particular, they have selflessly endured my separation for over five years. The toll this has taken on them is quite visible but I have never heard them complain. I am also extremely grateful to my brothers, Saad and Zain, and their families for being a constant source of support and comfort during my Ph.D. as they have been for the rest of my life. I will always cherish my frequent visits to them during these years as some of the best times of my life.

The time of my Ph.D. has been a source of great blessings. Perhaps, the greatest one is my wife who I met two years ago. Not only has she been a constant source of encouragement during the most difficult times of my Ph.D., but she has also contributed to this dissertation in material terms. While she is not a physicist, she has the remarkable ability to translate her artistic insight into the language of the sciences. Many ideas that have gone into this dissertation have been refined over and over through my discussions with her.

The other great blessing that my Ph.D. has brought me is having come across my teacher, Dr. Basit Bilal Koshul, who has completely transformed me as an individual. I met him four years ago in one of his workshops, and anyone who has been to his workshops would attest that you aren't the same person once you leave his lecture, for good or for bad. He has taught me the ethics of thought and articulation, but above all, he has taught me how to be a decent human being. Not that I claim to have become one by any means, but at the very least I have become able to appreciate the enormity of this task. During the course of my Ph.D., the research directions that I have pursued and my thought processes around them have received direct inspiration from him.

I am also extremely indebted to my advisor Prof. Sabre Kais for his kindness and patience over the last five years. Without his unwavering support and constant encouragements, this

work would simply be impossible, period. The freedom that he afforded me to pursue my research and grow as a scholar, I don't think I could have had that anywhere else. His unbreakable faith in me despite all the setbacks that I have endured in the last 2 years is the reason I was able to push my Ph.D. over the line. Every time I have felt hopeless in my research, his words have given me the reassurance and the strength to continue. I don't think I can ever return what he has done for me, all I can hope for is to be able to make him proud one day.

I would also like to acknowledge the wonderful input of my advisory committee: Prof. Nicolas Gisin, who was kind enough to take out the time to be a part of my committee despite being thousands of miles away. His work in physics has had a deep impact on me, and much of the work in this dissertation is directly based on his line of thought; Prof. Nima Lashkari, who agreed to be my co-advisor and has given me extremely valuable feedback for the last year or so. I have also learned a great deal of physics from his courses; Prof. David Nolte and Prof. Jukka Vayrynen for their guidance and suggestions as well. Much of my knowledge about chaos comes from Prof. Nolte's blog and book *Introduction to Modern Dynamics: Chaos, Networks, Space and Time*.

I would also like to acknowledge the contribution of *Acacia Education Foundation* in shaping this dissertation. Over the last couple of years, I have regularly attended the *Julaybeeb workshops* led by Dr. Basit Koshul and others, held under the umbrella of this foundation. I also thank my colleagues Nauman Ibrahim and Huzaifa Siddiqi, who are affiliated with *Acacia*. The work presented in Chapter 4 proceeded directly from our yearlong discussions on the research works of Prof. Nicolas Gisin. Nauman Bhai has been a constant blessing in my life since we met during our undergraduate at *LUMS*. His calming presence and kind demeanor have consistently inspired me over the years.

There are some other individuals from the Department of Physics who have been very instrumental in shaping my journey at Purdue. Amer AbdAlGhaffar has been my constant companion for the last 5 years. We joined the department as graduate students at the same time and have since bonded like brothers. His company has been a great source of comfort in these difficult years away from my family. Irakli Giorgadze has been another close friend in the Physics department. We ended up as housemates by chance when Irakli moved to the

US and I couldn't be more grateful for that. We have had some very enriching discussions on physics and other topics and his presence has been such a blessing during these years. I would also like to thank Dr. David Sederberg for being a good friend and for always taking care of me as if I were his family, especially during the isolation of COVID. And finally, Prof. Arnab Banerjee mentored me for one and a half year early on in my Ph.D.. His mentorship has been very instrumental in my development as a researcher. He always treated me like a younger brother and I will always remember his kindness.

I am immensely thankful to all my colleagues and co-workers during these years: Shree Hari Sureshbabu, Manas Sajjan, Norhan Mahmoud Eassa, Phil Lotshaw, Paul Kairys, Sabri Efe Gurleyen. Without their input and hard work, this dissertation would not be possible. I would also like to acknowledge my funding sources for the last 5 years: Department of Physics and Astrononmy at Purdue, National Science Foundation (NSF), U.S. Department of Energy (DOE), Quantum Science Center (QSC) and Quantum Photonic Integrated Design Center (QUPIDC).

I am also extremely grateful to the Muslim community here in West Lafayette for being the center of my spirituality during these five difficult years. In times of trouble, I have always taken refuge in *Islamic Center of Greater Lafayette (ISGL)* which thankfully is located right on campus. I thank all the volunteers who take out the time to maintain the masjid. I would especially like to thank Br. Zaim Khalid and Br. Sohail Sadiq for devoting so much attention to the needs of the community during the time I have been here. May Allah bless the founders and the maintainers of the masjid and their generations to come.

This dissertation would also have been impossible without the Pakistani community here at Purdue. They have been my family away from home. I would especially like to mention Bilal Ahmad, Arslan Khan, Syed Hamid Ali, Faraz Ahmad, Saud Ur Rehman, Shah Zaib Farooq, Br. Ata Ur Rehman and Dr. Assad Yousafzai. They have always been there to support and assist me whenever I have needed them.

Lastly, I am immensely grateful to the American people for giving me the opportunity to pursue my Ph.D. in their wonderful country. They have treated me with extreme kindness and care. The humility of some Americans has inspired me to a depth that is difficult for me to express in words. Just being in the company of these people has unveiled a whole new range

of experience for me. I would especially like to thank Travis Stockton for the conversations we have had towards the end of my Ph.D. I will forever cherish these memories.

قطرہ میں دجلہ دکھائی نہ دے اور جزو میں کل
کھیل لڑکوں کا ہوا دیدۂ بینا نہ ہوا

مرزا غالب

Non-poetic English Translation: "If you can't divine the river (Tigris) in a single drop and the whole in the part, all your wisdom is mere child's play."

Poet: Mirza Ghalib

ABSTRACT

The remarkable rise of quantum simulation as a viable strategy for studying many-body phenomena has introduced an entirely new dimension to research in quantum mechanics. These platforms offer unprecedented versatility and control over the interactions between their fundamental degrees of freedom. Thus, they present an opportunity for the first time to experimentally investigate arbitrary Hamiltonian systems, even those that might not occur naturally. The vast majority of these platforms employ a *qubit* architecture, that is, their fundamental degree of freedom is a single qubit that can mathematically be described by a spin algebra. Therefore, the most natural Hamiltonians to study using these architectures are spin Hamiltonians.

Spin is the intrinsic angular momentum associated with quantum particles that dictates their magnetic moments and quantum statistics. However, Hamiltonians involving other kinds of degrees of freedom may also be mathematically described by a spin algebra; the Hamiltonians used in quantum simulators being a prominent example. Spin Hamiltonians have been known to demonstrate an incredible variety of phases of matter, ranging all the way from the well-known magnetic phases such as ferromagnets and paramagnets to the recently discovered exotic quantum phases such as quantum spin liquids. They have been the subject of extensive theroretical and experimental studies for many decades and have revealed fundamental insights into the *emergence* of quantum phases and phase transitions.

Moreover, spin systems have also proved to be ideal settings for investigating the manifestations of *chaos* in quantum systems such as through the dynamical generation of entanglement. Given the significance of these two themes, emergence and chaos, for physics in the 21st century, the availability of quantum simulation architectures presents an almost miraculous opportunity for carrying out deeper explorations into the emergence of phases of matter and quantum chaos using spin systems as our guideline. This is precisely the goal of this dissertation. This dissertation is based on three projects:

(i) Finite-size scaling on a digital quantum simulator using quantum restricted Boltzmann machine,

(ii) Simulations of frustrated Ising Hamiltonians using quantum approximate optimization,

(iii) A classical analogue of entanglement for a kicked top.

TABLE OF CONTENTS

1. INTRODUCTION

One of the most surprising properties of quantum particles that separate them from their classical counterparts is their intrinsic angular momentum, known as *spin*. Spin imparts a magnetic moment to these particles and governs their statistical properties – it determines whether the particles are *bosons* or *fermions*. Spin of electrons is the basis for *Pauli's exclusion principle* which explains the stability of matter. In atomic and molecular physics, it accounts for the higher resolution details of the energy spectra such as *fine and hyperfine structure.* In condensed matter physics, the spin of electrons and nuclei is essential in explaining the magnetism of materials, superconductivity, superfluidity and many other exotic phases of matter. In quantum field theory, the language of the *Standard model*, the spin of a particle determines the nature of the quantum field that must be invoked to describe it. Introduced by Wolfgang Pauli in 1924, it is an indispensable ingredient in accounting for physical phenomena on all scales ranging from the astronomical all the way down to particle physics.

Emergence and *chaos* are two themes that have been on the forefront of physics research for the last few decades. *Emergence* is concerned with the study of novel phenomena that arise as we move up on the scale of complexity to larger and larger collections of atoms and molecules. Remarkably, each new level of complexity demands the formulation of entirely new properties and laws for a description of the associated phenomena [1, 2]. The standard example of this is found in the description of *phases of matter* and *phase transitions* in condensed matter. *Chaos*, on the other hand, is concerned with the dynamical behavior of physical systems; in classical physics, among other features, it is characterized by the extremely sensitive dependence of trajectories on initial conditions. The quantum ramifications of chaos, however, are not yet as well understood, and this is a subject currently undergoing rapid growth. Although still in nascent stages of their development, both emergence and chaos are radically new modes of viewing physical phenomena, inviting us to revisit the long-standing problem of *classical-quantum correspondence* that pervades all of modern physics [3].

Meanwhile, the study of quantum many-body phenomena is also being revolutionized through the remarkable recent advances in *quantum simulation* technologies. A quantum simulation is carried out by mapping a given system to a versatile quantum architecture that is much easier to control and manipulate in a laboratory setting. Classical simulations of similar systems run into difficulties due to the exponential scaling of Hilbert spaces. Quantum simulations bypass these limitations by using an architecture that is fundamentally quantum. These architectures allow us to track the emergence of phases of matter and chaotic dynamics in quantum systems with a degree of control that would have been unimaginable a couple of decades ago. The most natural candidates to map onto these simulators are spin Hamiltonians since the scaling of spin Hilbert spaces is identical to these platforms. Our goal in this dissertation is to explore the interplay of quantum simulation techniques and spin Hamiltonians for a careful study of emergence and chaos in spin systems. In this chapter, we have outlined in detail our motivation for pursuing this research. We first introduce spin, emergence and chaos in Secs. 1.1, 1.2 and 1.3 respectively. We then synthesize the three themes in Sec. 1.4 to motivate the research direction pursued in this dissertation. Finally, we briefly outline the contents of the subsequent chapters in Sec. 1.5.

1.1 What is Spin?

In classical physics, the state of a particle is completely specified by its position and momentum $(\mathbf{r}, \mathbf{p})$; where each of the components of $\mathbf{r}$ and $\mathbf{p}$ are taken to be real numbers. In quantum physics, on the other hand, the state $(\mathbf{r}, \mathbf{p})$ is replaced by a wavefunction $\psi(\mathbf{r})$. The wavefunction defines probability distributions for both position $\mathbf{r}$ and momentum $\mathbf{p}$ given by $|\psi(\mathbf{r})|^2$ and $|\varphi(\mathbf{p})|^2$ respectively, where $\varphi(\mathbf{p}) = 1/(2\pi\hbar)^{\frac{3}{2}} \int \psi(\mathbf{r}) e^{-i\mathbf{r}\cdot\mathbf{p}/\hbar} d^3r$; $\hbar$ being the reduced Planck's constant. So, in contrast to the infinitely precise classical state $(\mathbf{r}, \mathbf{p})$, the quantum state $\psi(\mathbf{r})$ can be visualized as a density extended across a region of phase space.

However, in addition to smearing out the infinitely precise $(\mathbf{r}, \mathbf{p})$ into a density $\psi(\mathbf{r})$, quantum physics introduces a completely new degree of freedom to the particle unknown to classical physics, known as *spin* χ. So, the total quantum state of the particle is $\psi(\mathbf{r}, \chi)$ (see Fig. 1.1.) As a physical quantity, spin behaves like angular momentum. The operators $\mathbf{S} =$

(S_x, S_y, S_z) that represent spin satisfy the angular momentum operator algebra: $[S_i, S_j] = i\hbar\varepsilon_{ijk}S_k$ where $i, j = 1, 2, 3$ and ε_{ijk} is the Levi-Civita symbol. The eigenvalue of $\mathbf{S}^2$ is $s(s+1)$ where s is called the spin of the particle; it can take values from $s = 0, \frac{1}{2}, 1, \frac{3}{2}, 2, \cdots$. For a fundamental particle, it is a property intrinsic to the particle and is always fixed. For example, electrons have spin 1/2, photons have spin 1 etc.

While it is hard to visualize a clear pictorial representation of quantum spin, it engenders some very consequential properties to the particles that possess it. Here, we list three of the most important implications of quantum spin (also see Fig. 1.2.)

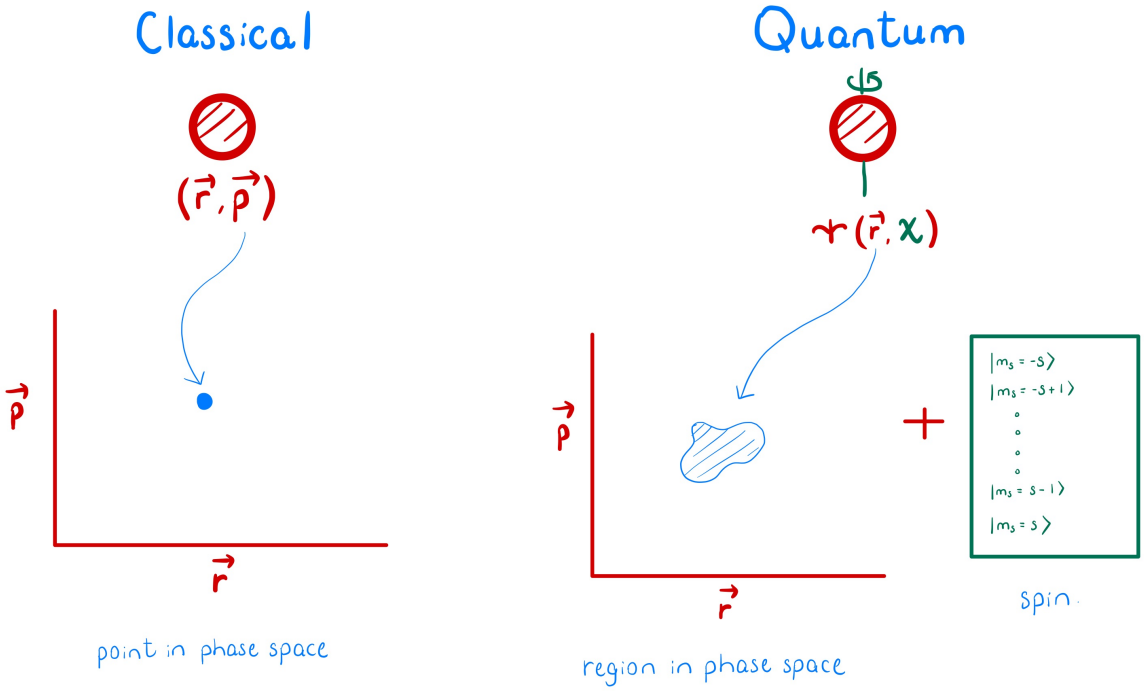

Figure 1.1. What is spin? The classical state of a particle is represented by a point in phase space $(\mathbf{r}, \mathbf{p})$. The quantum state $\psi(\mathbf{r}, \chi)$ in addition to defining probability distributions $|\psi(\mathbf{r})|^2$ and $|\varphi(\mathbf{p})|^2$ over $\mathbf{r}$ and $\mathbf{p}$ respecitvely, introduces a new degree of freedom χ; known as the spin of the particle.

1. **Magnetic moment**

   In classical electrodynamics, a charge moving in a loop possessing an angular momentum $\mathbf{L}$ exhibits a magnetic moment $\boldsymbol{\mu} = \gamma \mathbf{L}$ where γ is known as the gyromagnetic ratio. Quantum particles, in addition to their magnetic moment from orbital motion, also carry an intrinsic magnetic moment due to their spin. For example, the magnetic moment $\boldsymbol{\mu}_S$ imparted to electrons due to their spin is

   $$\boldsymbol{\mu}_S = -g_S \frac{\mu_B}{\hbar} \mathbf{S} \tag{1.1}$$

   where $g_S \approx 2$ is the g-factor, $\mu_B = e\hbar/(2m_e)$ is the Bohr magneton and $\mathbf{S}$ is the electron spin. This magnetic moment is fundamental to explaining the magnetic properties of atoms, molecules and materials.

2. **Quantum statistics**

   In classical physics, identical particles are distinguishable in the sense that one can track the state $(\mathbf{r}_i, \mathbf{p}_i)$ of any individual particle by following its trajectory. However, this is no longer possible in quantum physics, since particle states are spread out in phase space (see Fig. 1.1.) The state of a many-particle system in quantum mechanics is given by a single wavefunction $\psi(\mathbf{r}_1, \chi_1, \mathbf{r}_2, \chi_2, \cdots, \mathbf{r}_i, \chi_i, \cdots)$. Indistinguishability implies that the wavefunction has to be invariant under particle exchanges. Suppose that we have the exchange operator P_{12} for a two-particle system defined as: $P_{12}\psi(\mathbf{r}_1, \chi_1, \mathbf{r}_2, \chi_2) = \psi(\mathbf{r}_2, \chi_2, \mathbf{r}_1, \chi_1)$. Since $P_{12}^2 = I$, the eigenvalues of P_{12} are ± 1. This gives us two classes of states that are invariant with respect to the exchange operation P_{12}: (i) $P_{12}\psi(\mathbf{r}_1, \chi_1, \mathbf{r}_2, \chi_2) = \psi(\mathbf{r}_1, \chi_1, \mathbf{r}_2, \chi_2)$ and (ii) $P_{12}\psi(\mathbf{r}_1, \chi_1, \mathbf{r}_2, \chi_2) = -\psi(\mathbf{r}_1, \chi_1, \mathbf{r}_2, \chi_2)$. Identical particles which admit states of the first kind are called *bosons*, whereas those that admit the second kind are called *fermions*. Collections of bosons and collections of fermions exhibit dramatically distinct physical properties. Bosons experience an "effective attractive influence" towards each other and tend to accumulate together. This principle is invoked to explain superfluidity and superconductivity among many other phenomena. Fermions, on the other

hand, exert an "effective repulsive influence" on each other merely by virtue of being fermions. This is the basis for *Pauli's exclusion principle* which ensures the stability of matter. One of the most remarkable results in quantum physics is the *spin-statistics theorem*. It states that particles with integer spin $s = 0, 1, 2, \cdots$ are bosons, whereas particles with half-integer spin $s = \frac{1}{2}, \frac{3}{2}, \cdots$ are fermions. So, there is an intricate connection between the spin of a particle and its bosonic or fermionic nature.

3. **Quantum fields**

   In quantum field theory, the language of the standard model, particles are described as excitations of the all-pervasive quantum fields. Particle interactions and scattering processes are understood in terms of the interplay of the underlying fields. In this framework, there is a deep link between the spin of a particle and the nature of the field that represents it. The spin of a particle prescribes the kinds of interactions that it can partake in with other particles. Electrons are spin-1/2 particles and are represented by Dirac spinors $\psi_a(\mathbf{r}, t)$; photons are spin-1 particles and are represented by vector fields $A^\mu(\mathbf{r}, t)$; the higgs boson is a spin-0 particle represented by scalar field $\phi(\mathbf{r}, t)$ and so on.

1.2 What is Emergence?

Collections of a large number of individual entities give rise to new structures, characterized by their own unique properties and laws. This phenomenon is known as *emergence* [1, 2, 4]. When a large number of molecules are assembled into a gas, new properties emerge such as pressure, temperature, volume etc. that are meaningful only in the context of the entire collection and are ill-defined for individual molecules; likewise, new laws emerge that characterize the emergent structure such as the ideal gas law $PV = Nk_BT$. Similarly, collections of a large number of people produce new structures such as cities, nations, economies etc. that become real entities in their own right with unique properties and laws governing their behavior. The following three traits are characteristic of these emergent structures:

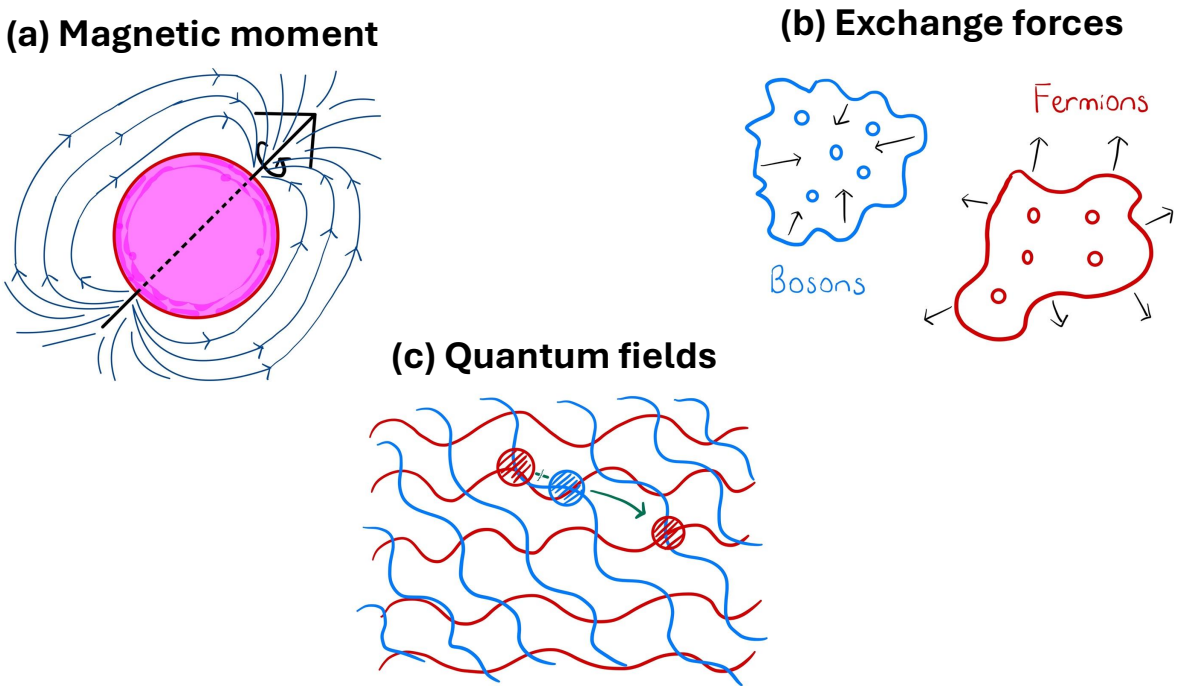

Figure 1.2. Implications of spin. (a) Spin imparts an intrinsic magnetic moment to the particle. (b) Spin determines whether a particle is a boson or a fermion. (c) Spin determines the nature of the quantum field that describes the particle.

1. **Decoupling**

   The behavior of the emergent structure is independent of what each unit is doing individually but depends only on the average behavior of all the units that make up the structure. Some units could be added or removed here or there without affecting the whole. Similarly, a few outliers could be allowed without changing the overall behavior of the collection. In this sense, the whole becomes decoupled from the individual units and can be treated as an entity in its own right. For example, gold will retain its economic value even if a few people think that its worth should not be greater than any other shiny piece of metal.

2. **Robustness**

   The emergent structure is robust against variations in external conditions, as long as the variations are not too drastic. A liquid remains a liquid as its temperature is

gradually increased. Purdue University will retain its status as a high impact university amid funding cuts.

3. **Transitions**

   As external conditions continue to vary, changes continue to accumulate in the emergent structure until the transition point is reached when the whole all of a sudden transforms into a completely new structure. For example, tensions between the public and the ruling elite in France continued to rise in the decades and centuries preceding the *Revolution* until they finally reached the "boiling point" in 1789, resulting in the establishment of a new societal order.

Emergence justifies the need for a variety of sciences and disciplines for a genuine quest towards reality. Although the fundamental entities of chemistry obey the laws of physics, chemistry is not merely applied physics. Instead, assemblies of molecules and compounds and their reactions with each other require the formulation of an entirely new set of laws and principles for their description, which form the subject matter of chemistry. Similarly, at an even greater level of complexity, the laws of biology describe the processes associated with life. But biology is not merely applied chemistry. A study of the laws of biology requires research that is as fundamental as any other [1].

Within physics, prototypic examples of emergence are the structures that emerge in matter, known as *phases of matter*. Typical examples are the solid, liquid, and gas phases of a material. A *phase diagram* maps the phases of a given substance as a function of the external conditions. As external conditions are varied, the material can undergo a *phase transition* as it goes from one phase to another. Fig. 1.3(a) shows the phase diagram of water in terms of pressure and temperature. At a fixed pressure, as the temperature increases along the green dashed curve, water first undergoes a phase transition from ice to liquid water and then undergoes another transition from liquid water to vapor (see Fig. 1.3(b).) In addition to the theory of phase transitions, the principles of emergence are also at the core of other major problems in physics such as the classical-quantum correspondence and the emergence of spacetime [4].

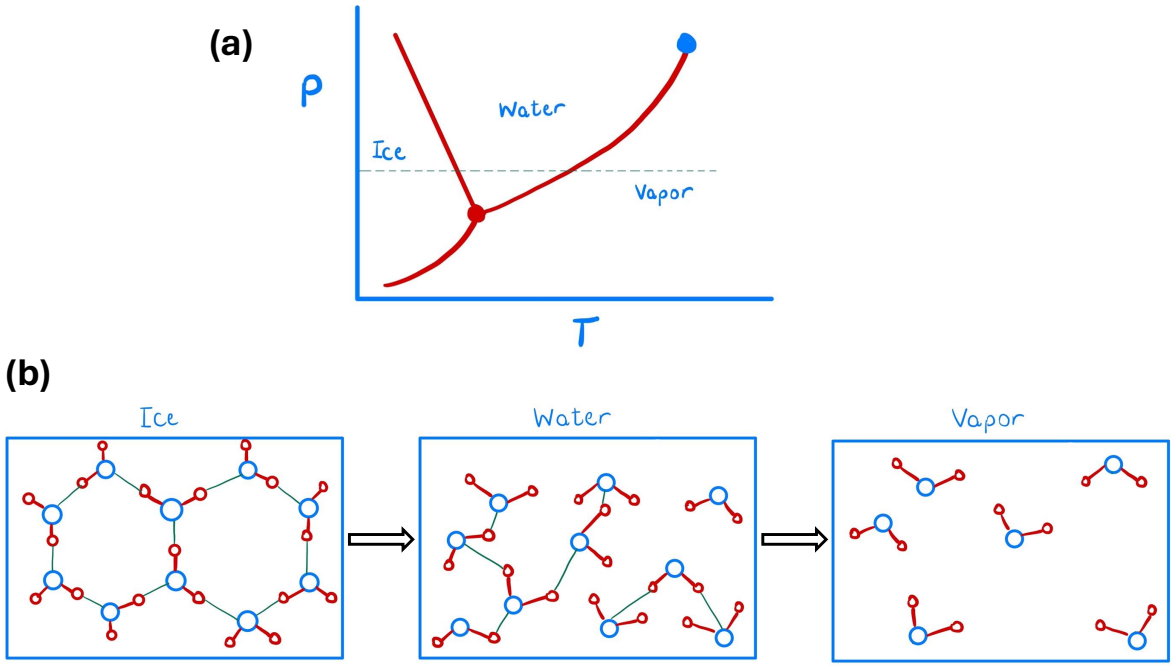

Figure 1.3. Phases of water. (a) Phase diagram of water as a function of pressure P and temperature T. (b) The arrangement and bonding of water molecules across the three phases. The building blocks in all the three phases are H_2O molecules, but the emerging structures are very different.

1.3 What is Chaos?

Henri Poincaré, around the end of the 19th century, had observed that the perturbation series for the gravitational three-body problem for a certain set of initial conditions failed to converge. At the time, this difficulty was seen as a mere mathematical artifact, and it was believed that some kind of renormalization procedure would solve this issue. However, it came as a huge surprise when developments in the 1950s and 60s, culminating in the *KAM (Kolmogorov, Arnold, Moser) theory*, revealed that these difficulties were due, in fact, to a fundamentally new type of behavior in dynamical systems satisfying Newton's laws, later dubbed *chaos*. It was discovered that in most systems starting from the celebrated three-body problem, it was not possible to predict the dynamical behavior over sufficiently long periods of time [5, 6].

One of the chief quests in the history of classical mechanics has been to look for dynamical systems that are explicitly solvable, that is, for which explicit formulas for the flow of the system can be found. A mathematically precise notion of "solvability" of a Hamiltonian system was developed for this purpose, known as *integrability*. A Hamiltonian system with n degrees of freedom is considered integrable if it has n independent constants of motion $\{f_1, f_2, f_3, \cdots, f_n\}$. Setting n independent functions of phase space coordinates equal to constants defines an n-dimensional manifold in a $2n$-dimensional phase space. For integrable systems, the n-dimensional manifold produced by fixing the values of f_k for $k = 1, ..., n$ is an n-dimensional torus $\mathbb{T}^n$. The phase space trajectories of integrable systems are restricted to these tori; they wind up around these tori but cannot escape them. Thus these tori are called *invariant tori*. The invariant tori fit together in concentric layers and foliate the phase space [7].

Fig. 1.4(a) depicts the invariant tori for a $n = 2$ degree-of-freedom integrable system in a 3-dimensional slice of its 4-dimensional phase space. The 3-dimensional slice can be obtained by fixing the energy of the system. A helpful device for visualizing higher-dimensional phase space flows is the *Poincaré map*. To construct the Poincaré map, a surface is chosen transverse to the flow, known as the *Poincaré section*. The points where the trajectory crosses the Poincaré section are recorded (see Fig. 1.4(b).) The 2-dimensional invariant tori in Fig. 1.4(a) become circles on the Poincaré section as shown in Fig. 1.4(c).

For integrable systems, one can perform a canonical transformation to the so-called *action-angle variables* $(\theta, I) = (\theta_1, ..., \theta_n, I_1, ..., I_n)$ for which the Hamiltonian depends only on the action variables $H = h(I)$. In these coordinates, the canonical equations become

$$\frac{dI_k}{dt} = 0, \qquad \frac{d\theta_k}{dt} = \omega_k \tag{1.2}$$

where $\omega_k = \partial h/\partial I_k$ are called the frequencies and $k = 1, ..., n$. The action variables $I = (I_1, ..., I_n)$ are fixed during the flow, so each $I = I^0$ labels an invariant torus. The angle variables $\theta = (\theta_1, ..., \theta_n)$ represent the cyclic directions on the torus. Angle variables evolve uniformly (since the frequencies $\omega = (\omega_1, ..., \omega_n)$ are fixed on a torus) as the trajectories wrap around the torus.

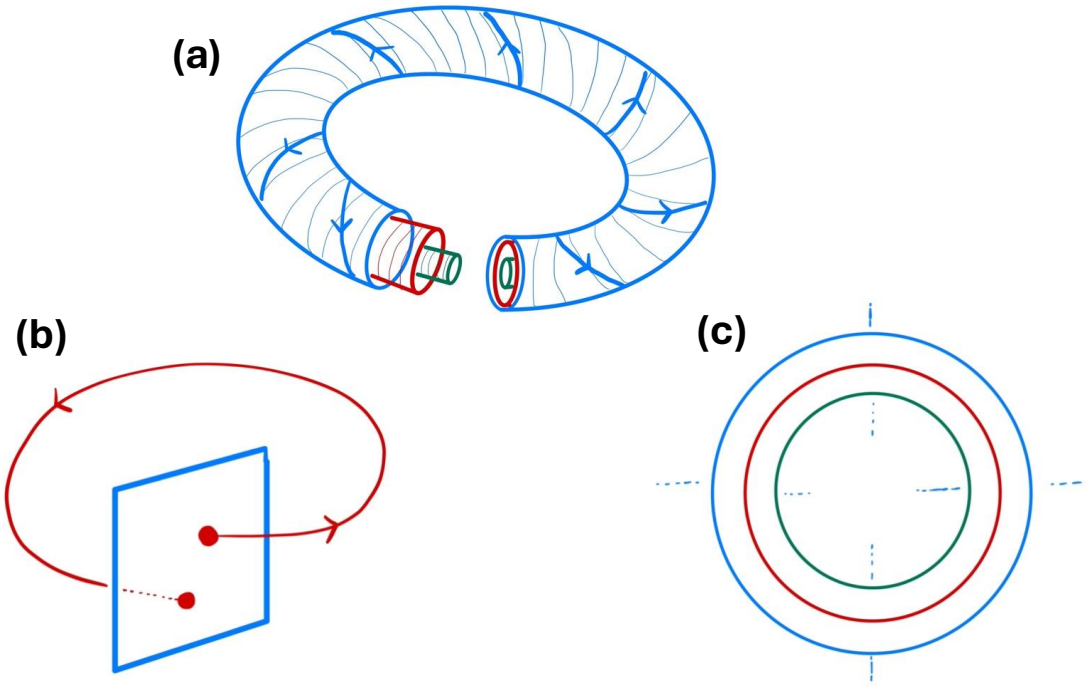

Figure 1.4. Integrable Hamiltonian systems. The phase space of integrable Hamiltonian systems is foliated by invariant tori. A phase space trajectory always stays on the invariant torus that it started on and wraps around it with time. (a) An illustration of 2-dimensional invariant tori for a $n = 2$ degree-of-freedom integrable system. The tori are shown in a 3-dimensional slice of the 4-dimensional phase space. (b) Poincaré map is a convenient device for visualizing higher dimensional flows. A Poincaré section is chosen transverse to the flow. Points are recorded wherever the trajectory passes through the section. (c) Poincaré section for the tori in (a).

Consider an integrable system with $n = 2$ degrees of freedom described by the action-angle coordinates $(\theta_1, \theta_2, I_1, I_2)$. The invariant tori for this system are 2-dimensional, illustrated in Fig. 1.4(a). Clearly, for a uniform flow on $\mathbb{T}^2$, there are only two possibilities: (i) if ω_1/ω_2 is a rational number, the flow eventually returns to its starting point and is periodic; (ii) if ω_1/ω_2 is an irrational number, the flow never returns but continues to fill up the torus more and more densely. The invariant tori for which ω_1/ω_2 is a rational number are called *resonant tori*, whereas, the ones for which ω_1/ω_2 is irrational are known as *nonresonant tori*. The resonant tori are distributed among the nonresonant tori exactly as rational numbers

are distributed among irrational numbers[1]. These definitions can be generalized for the n-dimensional case: the n-dimensional invariant torus $\mathbb{T}^n$ is resonant if $\exists\, k \in \mathbb{Z}^n$ $(k \neq 0)$ such that $k \cdot \omega = 0$ where $\mathbb{Z}$ is the set of integers and $\omega = (\omega_1, ..., \omega_n)$. If the only solution to $k \cdot \omega = 0$ is $k = (k_1, ..., k_n) = (0, ..., 0)$ then the torus is nonresonant [7].

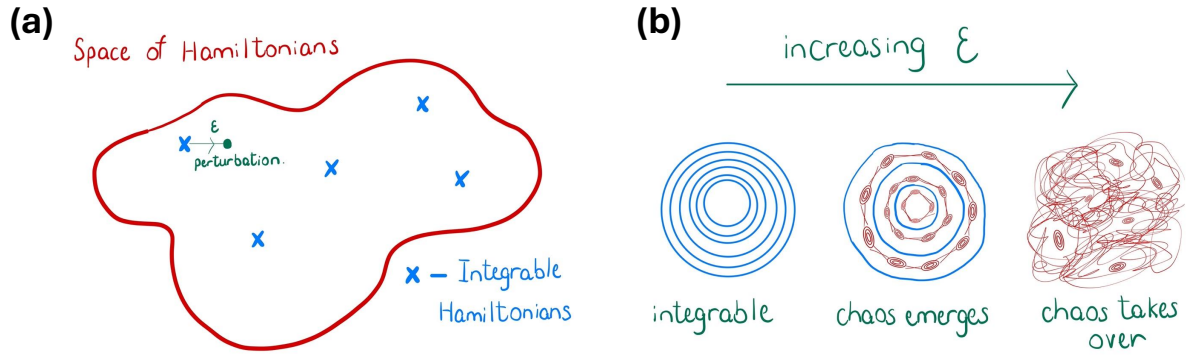

Figure 1.5. KAM theory. (a) Integrable Hamiltonian systems are isolated islands in the space of all Hamiltonians. An arbitrary Hamiltonian can be considered as a perturbation away from the integrable limit. (b) As the perturbation ε is turned on, the resonant tori of the unperturbed integrable Hamiltonian begin to break whereas a large number of the non-resonant ones survive. When ε is sufficiently large, chaos takes over the entire phase space leaving only a few stability islands.

Integrable Hamiltonians are akin to isolated islands in the sea of all Hamiltonians. General Hamiltonian systems can be considered as perturbations away from these islands (see Fig. 1.5(a).) Mathematically, a perturbed Hamiltonian system is written as $H(\theta, I, \varepsilon) = h(I) + \varepsilon f(\theta, I, \varepsilon)$, where $h(I)$ is the unperturbed integrable Hamiltonian and $\varepsilon f(\theta, I, \varepsilon)$ is the perturbation. ε controls the strength of the perturbation. The main message of *KAM theory* is that, as you perturb a system away from the integrable limit, the resonant tori (and some 'close to resonant' too) of the integrable Hamiltonian start to break up chaotically whereas a large subset of nonresonant tori survive and are distorted only slightly (see Fig. 1.5(b).) Several dynamical features begin to develop in the vicinity of these breaking tori that are seen as the hallmarks of *chaos*: (i) *sensitive dependence on initial conditions*

[1]↑This requires that ω_1/ω_2 changes (continuously) as one moves between the invariant tori; such systems are called *nondegenrate*. See [7] for more details.

i.e. trajectories starting close by can end up quite far apart in time; (ii) *dense set of periodic orbits* i.e. arbitrarily close to every point (in the region where chaos is developing), you can find a periodic orbit; (iii) *topological mixing* i.e. any open set (in the associated region) eventually overlaps with any other open set (in the associated region,) as a result of the flow. Perhaps, the most surprising conclusion of KAM theory is that these features are the rule and not the exception; they are found in the vast majority of Hamiltonian systems [7].

The presence of chaos in classical systems raises issues for the classical-quantum correspondence, since it is generally accepted that quantum systems cannot exhibit chaos. The standard argument for the absence of chaos in quantum mechnaics works by evolving two quantum states $|\psi_1(0)\rangle$ and $|\psi_2(0)\rangle$ using the unitary time evolution operator $U(t)$ and tracking their inner product $\langle\psi_1(t)|\psi_2(t)\rangle$. The unitarity of time evolution ensures that the inner product is preserved in time i.e. $\langle\psi_1(t)|\psi_2(t)\rangle = \langle\psi_1(0)|\, U(t)^\dagger U(t)\, |\psi_2(0)\rangle = \langle\psi_1(0)|\psi_2(0)\rangle$. Thus, quantum states do not separate in time and this is taken to imply that there can be no chaos in quantum physics. While the argument sounds plausible, one is left to wonder how such a classically ubiquitous phenomenon can have no quantum counterpart given that the dynamics in both cases are generated by the same Hamiltonian? Another question that is left unaddressed is how can chaos emerge on the scale of our everyday classical reality if the dynamics on the microscopic scale are completely non-chaotic [3, 8]?

1.4 Spin Physics: from Emergence to Chaos

The significance of *emergence* and *chaos* in modern physics naturally motivates a search for fresh avenues of exploration in these themes and a study of their implications for the classical-quantum correspondence. One of the most remarkable developments in recent decades is the emergence of *quantum simulation* as a viable platform to investigate quantum phenomena. In this approach, a given Hamiltonian system is mapped to a versatile quantum architecture that is easier to maneuver and control in a lab than the parent system. The desired interactions are engineered on the quantum architecture, and a variety of physical operations are performed, depending on the objective. While only a far-fetched possibility some decades ago, remarkable technological advances in isolating quantum systems from

their environments and in achieving control over their mutual interactions have enabled the current proliferation of activity in quantum simulation experiments.

Currently, a wide variety of architectures are being employed to carry out quantum simulation experiments: superconducting quantum circuits, trapped ions, Rydberg atom arrays, photonic systems, and many others. There is still a long road ahead though, as the architectures are at present very noisy and do not lend themselves to the desired degree of control. Despite these limitations, however, they have been used to create quantum states that have otherwise not been observed directly in nature (see, for example [9, 10].) Some of these architectures are also being used to pursue the grand ambition of building a *universal quantum computer* – a device that can perform all possible quantum operations on a given Hilbert space or in other words, a device that can simulate any arbitrary Hamiltonian on a given Hilbert space [11, 12].

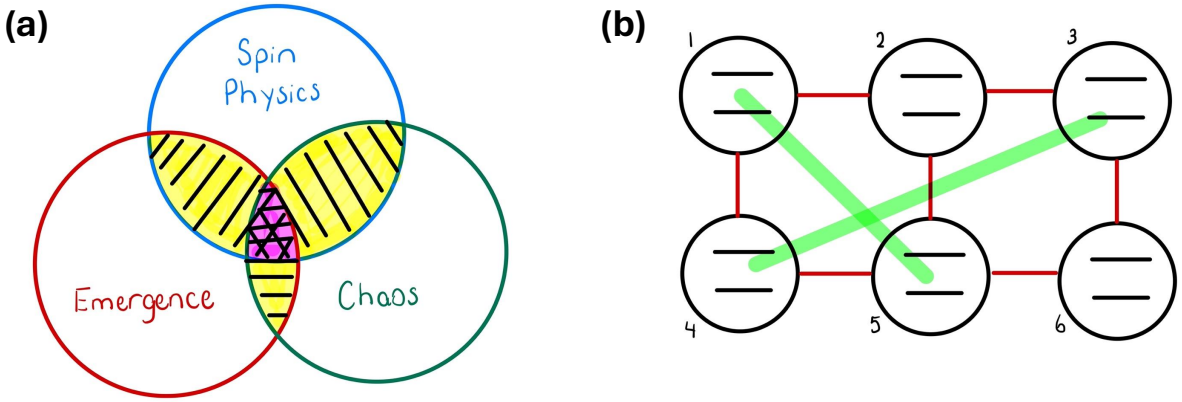

Figure 1.6. Spin physics in the age of quantum simulation. (a) Spin Hamiltonians are perhaps the simplest many-body Hamiltonians providing ideal scenarios to study *emergence* of phases of matter and the quantum dynamical manifestations of *chaos*. (b) Depiction of a 6-qubit quantum architecture in a state with qubits 1 and 5 and qubits 3 and 4 entangled respectively. The development of quantum simulators has introduced new possibilities for the study of spin Hamiltonians offering an unprecedented degree of control.

The fundamental building block of most quantum simulators and quantum computers is a two-level quantum system called a *qubit*. While not a spin system physically (though spins can potentially be used as qubits,) it is mathematically described by the same algebra as spin systems. Therefore, spin systems provide the most natural Hamiltonians to map

onto a qubit architecture. Moreover, the customizability of the architecture ensures that arbitrary spin Hamiltonians can be studied on these devices, some of which might not even be observable directly in nature. These developments have opened up the possibility of investigating, with an unprecendeted degree of control, the *emergence* of phases of matter and quantum dynamical manifestations of *chaos* in spin Hamiltonians (see Fig. 1.6.)

The investigations presented in this dissertation involve three distinct categories of Hamiltonians:

1. **Light-matter interaction models**

   These models were originally created to describe the interaction of electromagnetic fields and atoms. In these models, atoms are typically treated as two-level systems, thus each atom can be directly mapped to a spin-1/2 algebra. The electromagnetic field modes are described in terms of bosonic creation and annihilation operators. Therefore, the range of validity of these models can be extended to any situation where a two-level quantum system interacts with some bosonic environment. Such scenarios could also include, for example, the interaction of electronic spins in a material with the phonon modes i.e. vibrations of the lattice.

   A quite well-known example of a Hamiltonian from this category is the Dicke model. This Hamiltonian describes the interaction of N two-level systems with a common bosonic mode,

   $$H_{\text{Dicke}} = \omega_0 a^\dagger a + \frac{\Omega}{2}\sum_{i=1}^{N}\sigma_z^{(i)} - \frac{\lambda}{\sqrt{N}}(a + a^\dagger)\sum_{i=1}^{N}\sigma_x^{(i)}. \tag{1.3}$$

   Here $\hbar = 1$, ω_0 is the frequency of the bosonic mode, Ω is the energy spacing of the two-level systems, and λ is the coupling strength between the two. When $N \to \infty$, this model famously shows a phase transition to a *superradiant phase* as λ goes beyond a critical value λ_c. The superradiant phase is characterized by a greatly enhanced boson number as a result of the coherent interactions between the two-level systems through the bosonic mode.

A special limit of this model dealing with just a single two-level system interacting with a bosonic mode is known as the *quantum Rabi model*,

$$H_{\text{Rabi}} = \omega_0 a^\dagger a + \frac{\Omega}{2}\sigma_z - \lambda(a + a^\dagger)\sigma_x. \tag{1.4}$$

Surprisingly, despite operating at a finite system size, this model still exhibits a transition to a superradiant phase [13]. This Hamiltonian will be the focus of our study in Chapter 2.

2. **Spins on a lattice**

Consider a collection of atoms distributed on a lattice. Suppose only one outermost electron from each atom contributes in its interactions with neighboring atoms. Moreover, in the low-energy limit, we can further restrict our attention only to the lowest energy orbital of each atom. Now, let us take a close look at the interaction between two neighboring atoms. Suppose the orbitals on the sites of these two atoms are represented by $\psi_a(\mathbf{r})$ and $\psi_b(\mathbf{r})$ respectively. We have already seen in Sec. 1.1 that multi-electron wavefunctions must be antisymmetric under electron exchanges due to the fermionic nature of electrons. With that in mind, consider two possibilities for the collective wavefunction of the two-electron system: (i) $\psi^S_{ab}(\mathbf{r}_1, \chi_1, \mathbf{r}_2, \chi_2) = \frac{1}{\sqrt{2}}(\psi_a(\mathbf{r}_1)\psi_b(\mathbf{r}_2) + \psi_b(\mathbf{r}_1)\psi_a(\mathbf{r}_2))\ \chi^S_{12}$ where $\chi^S_{12} = \frac{1}{\sqrt{2}}(|\uparrow\rangle_1 |\downarrow\rangle_2 - |\downarrow\rangle_1 |\uparrow\rangle_2)$ is the spin-singlet state; (ii) $\psi^T_{ab}(\mathbf{r}_1, \chi_1, \mathbf{r}_2, \chi_2) = \frac{1}{\sqrt{2}}(\psi_a(\mathbf{r}_1)\psi_b(\mathbf{r}_2) - \psi_b(\mathbf{r}_1)\psi_a(\mathbf{r}_2))\ \chi^T_{12}$ where χ^T_{12} is one of the spin-triplet states: $|\uparrow\rangle_1 |\uparrow\rangle_2$, $\frac{1}{\sqrt{2}}(|\uparrow\rangle_1 |\downarrow\rangle_2 + |\downarrow\rangle_1 |\uparrow\rangle_2)$, $|\downarrow\rangle_1 |\downarrow\rangle_2$. In the first case, the spatial part of the wavefunction is symmetric under electron exchange, whereas, in the latter case it is anti-symmetric. However, the total wavefunction is anti-symmetric in both cases. For the spatially symmetric case, we ignore the possible wavefunctions $\psi_a(\mathbf{r}_1)\psi_a(\mathbf{r}_2)$ and $\psi_b(\mathbf{r}_1)\psi_b(\mathbf{r}_2)$ due to the prohibitive Coulombic energy cost inflicted when both electrons are put on the same site. We further assume that $\psi_a(\mathbf{r}_1)\psi_b(\mathbf{r}_2)$ and $\psi_b(\mathbf{r}_1)\psi_a(\mathbf{r}_2)$ are very nearly the eigenstates of the total Hamiltonian H_{12}. It is straightforward to show that $\langle\psi^S_{ab}| H |\psi^S_{ab}\rangle = E + \lambda$ and $\langle\psi^T_{ab}| H |\psi^T_{ab}\rangle = E - \lambda$ where $E = \langle\psi_a, \psi_b| H_{12} |\psi_a, \psi_b\rangle = \langle\psi_b, \psi_a| H_{12} |\psi_b, \psi_a\rangle$ and

$\lambda = \langle\psi_a, \psi_b| H_{12} |\psi_b, \psi_a\rangle = \langle\psi_b, \psi_a| H_{12} |\psi_a, \psi_b\rangle$ is assumed to be real. Thus, the effective low-energy physics of this system can be described by a Hamiltonian with an energy gap of 2λ between the singlet and the triplet states. This effective Hamiltonian is $H_{eff} = -2\lambda\, \mathbf{S}_1 \cdot \mathbf{S}_2$, where $\mathbf{S}_{1,2}$ are the spin operators for the two electrons. In this way, the complicated interactions of electrons in a material can be reduced to effective spin interactions in the low-energy limit. Interactions of this kind are called *exchange interactions*. They tend to either align or anti-align neighboring spins depending on whether they are ferromagnetic ($\lambda > 0$) or anti-ferromagnetic ($\lambda < 0$). Spins interacting in this way on a wide range of lattice geometries produce an enormous variety of *magnetic phases* that are only beginning to be discovered [4]. Some of these phases are so exotic that they might not even seem to possess any magnetic order at first glance, however a closer look reveals a "hidden" structure supported by long-range entanglement that is extremely robust against environmental influences [9, 14, 15]. Spins interacting via exchange interactions will be the subject of our investigations in Chapter 3.

3. **All-to-all interacting systems**

   The last category of Hamiltonians pertains to systems in which all spins interact with all other spins. An example is the *kicked top model* [16] with the following Hamiltonian,

$$H_{\mathrm{KT}}(t) = \frac{p}{\tau} J_y + \frac{\kappa}{2j} J_z^2 \sum_{n=-\infty}^{+\infty} \delta(t - n\tau), \tag{1.5}$$

   where we again take $\hbar = 1$. In this model, $\mathbf{J} = \sum_{i=1}^{N} \mathbf{S}_i$, so the individual spins enter the Hamiltonian only through the global variable $\mathbf{J}$. The Hamiltonian can be re-written in terms of the spin operators $\mathbf{S}_i$ in the following way,

$$H(t) = \frac{p}{\tau} \sum_{i=1}^{N} S_{iy} + \frac{\kappa}{2j} \left(\sum_{i=1}^{N} S_{iz}^2 + \sum_{i \neq j} S_{iz} S_{jz} \right) \sum_{n=-\infty}^{+\infty} \delta(t - n\tau). \tag{1.6}$$

   Under this Hamiltonian, each spin precesses freely around the y-axis by an angle p for the duration τ, when it suddenly experiences a kick, which can be interpreted as

a sudden precession of each spin around the z-axis by an angle proportional to the z-component of the scaled total angular momentum J_z/j of the system. The classical dynamics of this model exhibit a transition to chaos as the kick strength κ is raised. Thus the quantum version of this model presents a tremendous opportunity to study the quantum manifestations of chaos. For example, it has already been observed that the dynamical generation of entanglement between the spins acts as a quantum signature of chaos for this system [17, 18]. This system will be the subject of our study in Chapter 4.

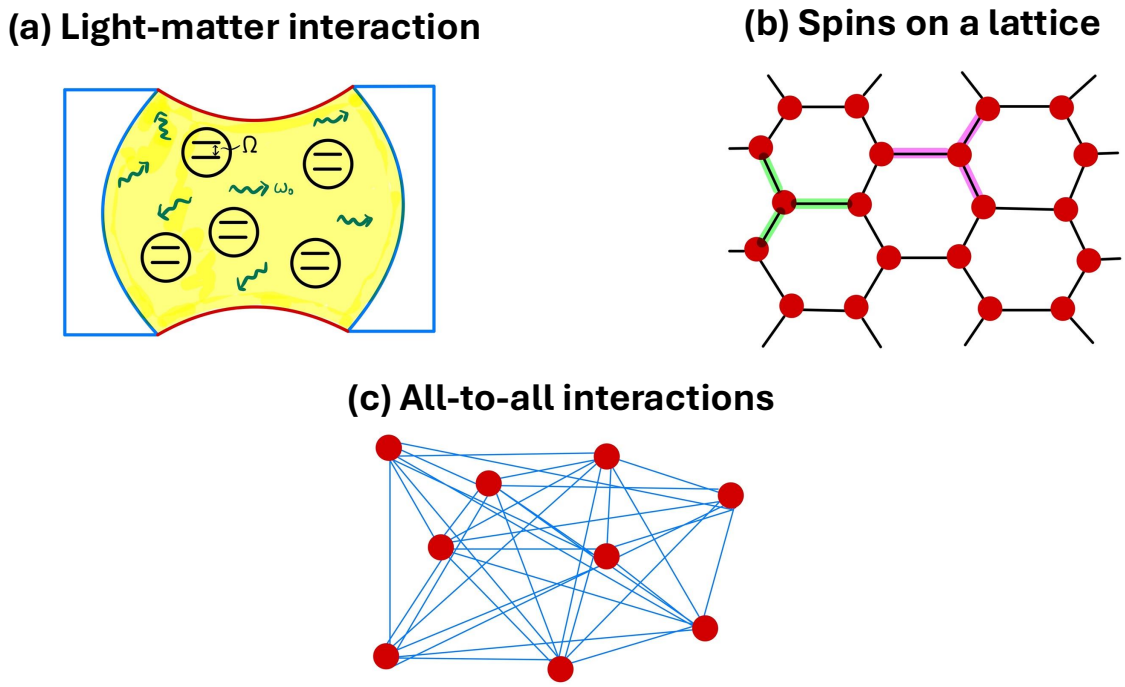

Figure 1.7. Types of Hamiltonians explored in this dissertation. (a) Two-level systems interacting with a bosonic mode e.g. atoms in a cavity, spin-phonon interactions etc. (b) Exchange interactions between spins distributed on a lattice. (c) Every spin interacts with every other spin.

1.5 Dissertation Overview

In this dissertation, our goal is to explore the potential of quantum simulation and quantum computing in revealing a deeper understanding of *emergence* and *chaos* in quantum spin systems (see Fig. 1.6.) The organization of the dissertation is as follows:

- In *Chapter* 2, we present a protocol to compute the critical parameters of a phase transition on a quantum computer. For this purpose, we implement the *quantum restricted Boltzmann machine (QRBM)* algorithm, which uses an artificial neural network architecture to learn the ground state of a quantum Hamiltonian. As an example, we demonstrate the use of this algorithm to locate the critical point for the superradiant phase transition in the *quantum Rabi model*.

- In *Chapter* 3, we investigate the viability of preparing ground states of spin Hamiltonians on multiple lattice geometries using another quantum algorithm, the *quantum approximate optimization algorithm (QAOA)*. The results demonstrate the promise of this approach as a feasible route to understand the diversity of magnetic phases in spin systems once quantum computational advantage becomes available.

- In *Chapter* 4, we explore the interplay of *quantum entanglement* and *classical chaos* in the kicked top model. While a clear relationship between the two has been demonstrated in quantum simulation experiments, we develop a classical analogue of entanglement to understand the inner details of this relationship.

- In *Chapter* 5, we discuss some philosophical implications of the developments in *emergence* and *chaos* for the *classical-quantum correspondence*. Attempt is made to demonstrate the significance of these developments for modern physics and the new opportunities for research that they open up.

Bibliography

[1]P. W. Anderson, "More is different," Science **177**, 393–396 (1972).

[2]R. B. Laughlin, *A different universe: reinventing physics from the bottom down* (Basic Books, New York, 2005).

[3]L. E. Ballentine, "The emergence of classical properties from quantum mechanics: new problems from old," in *Fundamental problems in quantum physics*, edited by M. Ferrero and A. van der Merwe (Springer Netherlands, Dordrecht, 1995), pp. 15–28.

[4]G. Musser, "Emergence: a review of research on condensed matter and quantum gravity and resonances between these fields," Foundational Questions Institute (2021).

[5]J. Lighthill, J. M. T. Thompson, A. K. Sen, A. G. M. Last, D. T. Tritton, and P. Mathias, "The recently recognized failure of predictability in newtonian dynamics [and discussion]," Proceedings of the Royal Society of London. Series A, Mathematical and Physical Sciences **407**, 35–50 (1986).

[6]I. Prigogine, *From being to becoming: time and complexity in the physical sciences* (W. H. Freeman and Company, New York, 1980) Chap. 2.

[7]H. S. Dumas, *The kam story* (WORLD SCIENTIFIC, 2014).

[8]W. H. Zurek and J. P. Paz, "Quantum chaos: a decoherent definition," Physica D: Nonlinear Phenomena **83**, Quantum Complexity in Mesoscopic Systems, 300–308 (1995).

[9]G. Semeghini, H. Levine, A. Keesling, et al., "Probing topological spin liquids on a programmable quantum simulator," Science **374**, 1242–1247 (2021).

[10]K. J. Satzinger, Y.-J. Liu, A. Smith, et al., "Realizing topologically ordered states on a quantum processor," Science **374**, 1237–1241 (2021).

[11]M. A. Nielsen and I. L. Chuang, *Quantum computation and quantum information: 10th anniversary edition* (Cambridge University Press, 2010).

[12]J. Preskill, *Lecture notes*, https://www.preskill.caltech.edu/ph219/index.html#lecture.

[13]M.-J. Hwang, R. Puebla, and M. B. Plenio, "Quantum phase transition and universal dynamics in the rabi model," Phys. Rev. Lett. **115**, 180404 (2015).

[14]L. Savary and L. Balents, "Quantum spin liquids: a review," Rep. Prog. Phys. **80**, 016502 (2016).

[15]R. Samajdar, W. W. Ho, H. Pichler, M. D. Lukin, and S. Sachdev, "Quantum phases of rydberg atoms on a kagome lattice," Proceedings of the National Academy of Sciences **118**, e2015785118 (2021).

[16]F. Haake, M. Kuś, and R. Scharf, "Classical and quantum chaos for a kicked top," Z. Physik B - Condensed Matter **65**, 381–395 (1987).

[17]C. Neill, P. Roushan, M. Fang, et al., "Ergodic dynamics and thermalization in an isolated quantum system," Nature Phys **12**, 1037–1041 (2016).

[18]A. Lerose and S. Pappalardi, "Bridging entanglement dynamics and chaos in semiclassical systems," Phys. Rev. A **102**, 032404 (2020).

2. PROJECT I: PHASE TRANSITION IN THE QUANTUM RABI MODEL

The contents of this chapter are adapted from the following article:

B. Khalid, S. H. Sureshbabu, A. Banerjee and S. Kais, "Finite-size scaling on a digital quantum simulator using quantum restricted Boltzmann machine", Front. Phys. 10:915863 (2022.)

Abstract: *The critical point and the critical exponents for a phase transition can be determined using the Finite-Size Scaling (FSS) analysis. This method assumes that the phase transition occurs only in the infinite size limit. However, there has been a lot of interest recently in quantum phase transitions occuring in finite size systems such as a single two-level system interacting with a single bosonic mode e.g. in the Quantum Rabi Model (QRM). Since, these phase transitions occur at a finite system size, the traditional FSS method is rendered inapplicable for these cases. For cases like this, we propose an alternative FSS method in which the truncation of the system is done in the Hilbert space instead of the physical space. This approach has previously been used to calculate the critical parameters for stability and symmetry breaking of electronic structure configurations of atomic and molecular systems. We calculate the critical point for the quantum phase transition of the QRM using this approach. We also provide a protocol to implement this method on a digital quantum simulator using the Quantum Restricted Boltzmann Machine algorithm. Our work opens up a new direction in the study of quantum phase transitions on quantum devices.*

2.1 Introduction

A phase transition occurs whenever the thermodynamic functions of a system become non-analytic e.g. as a liquid changes into a gas, the density of the system changes discontinuously. If the phase transition occurs at a finite temperature $T \neq 0$, the transition is called a classical phase transition (CPT) as it is dominated by thermal fluctuations. On the other hand, if the transition occurs by tuning some parameter in the system's Hamiltonian as $T \to 0$, it is called a quantum phase transition (QPT) since it is dominated by quantum fluctuations. A CPT appears only when the system is infinite i.e. $N \to \infty$ [1]. On the other hand, a QPT doesn't necessarily require $N \to \infty$. Recently there has been a lot of interest in QPTs occurring in finite size light-matter interaction systems [2–7].

It has been shown that a QPT occurs in the Quantum Rabi Model (QRM) which describes the interaction of a two-level system with one bosonic field mode [2] (see Eq. (2.1) for the Hamiltonian). Namely, when the energy separation of the two levels in the system Ω becomes infinitely large compared to the frequency of the bosonic mode ω_0, the ground state of the Hamiltonian undergoes a phase transition from a normal phase to a superradiant phase as the light-matter coupling exceeds the critical value. Moreover, the ground state of the Jaynes-Cummings model (JCM) which can be obtained from the QRM by performing the rotating-wave approximation has also been shown to exhibit the normal-superradiant phase transition [3]. Later on, a more general anisotropic QRM in which the rotating and counter-rotating terms can have different coupling strengths was also considered [4]. The QRM and JCM are limiting cases of this model. It was shown that the ground state for this more general case also undergoes the normal-superradiant phase transition. The phase transition in QRM has also been demonstrated experimentally using a $^{171}Yb^{+}$ ion in a Paul trap [7]. This experimental demonstration of a phase transition in a single two-level system has incited a lot of interest since this opens up an avenue for studying critical phenomena in controlled, small quantum systems.

In CPTs and some QPTs (which require $N \to \infty$), a finite-size scaling (FSS) analysis can be done to extract the critical point and the critical exponents of the transition [1, 8]. While this procedure is inapplicable to the QPTs discussed above since these phase transitions occur

at a finite system size, the phase transitions in these paradigmatic light-matter interaction models occur only in the limit $\Omega/\omega_0 \to \infty$ and FSS analysis can be done in Ω/ω_0 [2–4] instead. In this chapter, however, we propose a different approach to study such phase transitions. We apply the FSS in Hilbert space method [9–14] to the QPT in Quantum Rabi Model. In this approach, the truncation of the system is done not in the physical space but in the Hilbert space. The set of basis states spanning the infinite dimensional Hilbert space is truncated to a finite set and the scaling ansatz is employed in terms of the size of this set. This approach has previosuly been developed and applied to a single particle in Yukawa potential [10, 12] and the problem of finding electronic structure critical parameters for atomic and molecular systems [9, 11, 13–15].

In recent years, digital and analog quantum simulators have emerged as a promising platform for the simulation of quantum phenomena. Quantum simulators have already been used to study phase transitions using the method of partition function zeros [16] and the Kibble-Zurek mechanism [17, 18]. In this chapter, we present a protocol to implement the finite-size scaling method on a digital quantum simulator. We use the Quantum Restricted Boltzmann Machine (QRBM) algorithm to find the critical point of the Quantum Rabi model.

This chapter is organized as follows. In Sec. 2.2, we explain the theory of Quantum Rabi Model, Finite-Size Scaling and the Quantum Restricted Boltzmann Machine. In Sec. 2.3, we present our results obtained using the exact diagonalization method and QRBM. Finally in Sec. 2.4, we discuss our results and future prospects of studying quantum phase transitions on quantum devices.

2.2 Theory

2.2.1 Quantum Rabi Model

The QRM describes a two-level system interacting with a bosonic field mode. The Hamiltonian is [2],

$$H_{Rabi} = \frac{\Omega}{2}\sigma_z + \omega_0 a^\dagger a - \lambda\sigma_x(a + a^\dagger) \tag{2.1}$$

where we've chosen $\hbar = 1$. Ω is the energy separation between the two levels in the system, ω_0 is the frequency of the bosonic mode and λ is the system-environment coupling strength. The parity operator $\Pi = e^{i\pi(a^\dagger a + |\uparrow\rangle\langle\uparrow|)}$ commutes with H_{Rabi}. So, H_{Rabi} has a Z_2 symmetry.

This model has a critical point at $g = 2\lambda/\sqrt{\omega_0\Omega} = g_c = 1$ in the limit $\Omega/\omega_0 \to \infty$ [2]. For $g < 1$, the system is in the *normal phase* and the ground state is $|\phi^0_{np}(g)\rangle = \mathcal{S}[r_{np}(g)]\,|0\rangle\,|\downarrow\rangle$ where $\mathcal{S}[x] = \exp\left[\frac{x}{2}(a^{\dagger 2} - a^2)\right]$ and $r_{np}(g) = -\frac{1}{4}\ln(1-g^2)$. The rescaled ground state energy and photon number are $e_G(g) = \frac{\omega_0}{\Omega}\langle H_{Rabi}\rangle = -\omega_0/2$ and $n_G(g) = \frac{\omega_0}{\Omega}\left\langle a^\dagger a\right\rangle = 0$ respectively. For $g > 1$, the system is in a *superradiant phase* and the ground state is two-fold degenerate, $|\phi^0_{sp}(g)\rangle = \mathcal{D}[\pm\alpha_g]\mathcal{S}[r_{sp}(g)]\,|0\rangle\,|\downarrow^\pm\rangle$ here $r_{sp}(g) = -\frac{1}{4}\ln(1-g^{-4})$ and $\mathcal{D}[\alpha] = \exp\left[\alpha(a^\dagger - a)\right]$. $|\downarrow^\pm\rangle$ is the negative eigenvalue eigenstate of $\frac{1}{2g^2}\sigma_z \pm \frac{2\lambda\alpha_g}{g^2\Omega}\sigma_x$ where $\alpha_g = \sqrt{\frac{\Omega}{4g^2\omega_0}(g^4-1)}$. The rescaled ground state energy and photon number are $e_G(g) = \frac{\omega_0}{\Omega}\langle H_{Rabi}\rangle = -\omega_0(g^2 + g^{-2})/4$ and $n_G(g) = \frac{\omega_0}{\Omega}\left\langle a^\dagger a\right\rangle = (g^2 - g^{-2})/4$ respectively.

As shown in Fig. 2.1(a) and (b), d^2e_G/dg^2 is discontinuous at $g = g_c = 1$, indicating a continuous phase transition and $n_G = \frac{\omega_0}{\Omega}\left\langle a^\dagger a\right\rangle$ is an order parameter for this phase transition. In the *normal phase*, n_G is zero whereas in the *superradiant phase*, Z_2 symmetry is spontaneously broken and n_G becomes non-zero.

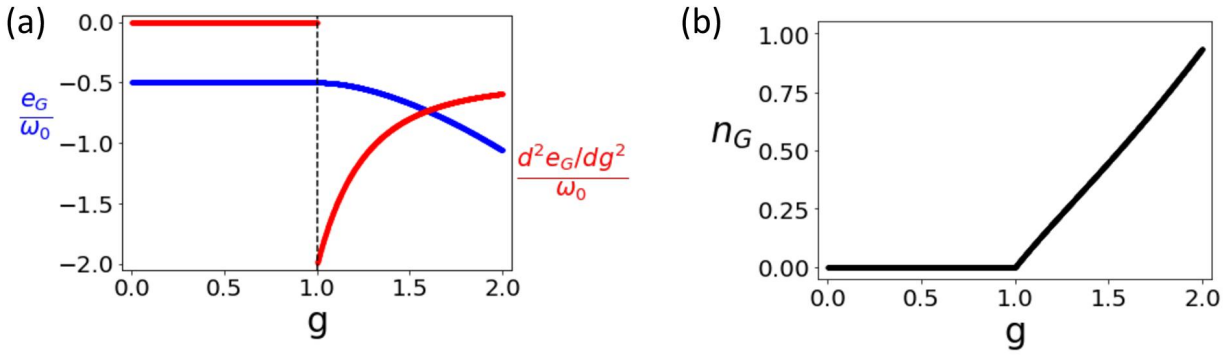

Figure 2.1. Phase Transition in Quantum Rabi Model. (a) The rescaled ground state energy $e_G/\omega_0 = \langle H_{Rabi}\rangle/\Omega$ and $(d^2e_G/dg^2)/\omega_0$ as functions of g. The discontinuity in $(d^2e_G/dg^2)/\omega_0$ at $g = g_c = 1$ indicates a countinuous phase transition. (b) The order parameter $n_G = \frac{\omega_0}{\Omega}\left\langle a^\dagger a\right\rangle$ as a function of g. n_G becomes non-zero when the Z_2 symmetry is spontaneously broken at $g > g_c = 1$.

We can also write effective low-energy Hamiltonians in both the *normal* and the *superradiant phases*. For $g < 1$, H_{Rabi} can be reduced to the following effective Hamiltonian [2],

$$H_{np} = \omega_0 a^\dagger a - \frac{\omega_0 g^2}{4}(a + a^\dagger)^2 - \frac{\Omega}{2}. \tag{2.2}$$

The system's degrees of freedom have been removed by projecting to $|\downarrow\rangle\langle\downarrow|$, since this is a low energy description. Similarly, for $g > 1$ the effective Hamiltonian can be written as [2],

$$H_{sp} = \omega_0 a^\dagger a - \frac{\omega_0}{4g^4}(a + a^\dagger)^2 - \frac{\Omega}{2}(g^2 + g^{-2}), \tag{2.3}$$

where this time around the Hamiltonian has been projected along $|\downarrow^\pm\rangle\langle\downarrow^\pm|$. In Sec. 2.3, we'll use H_{np} and H_{sp} to find the critical point of the model.

2.2.2 Finite-Size Scaling

The FSS method is widely used to determine the critical points and the critical exponents in phase transitions [1]. To demonstrate the method, consider that we have an infinite $2d$ system that undergoes a classical phase transition at a critical temperature $T = T_c$ [8]. Suppose Q is a quantity that becomes singular at $T = T_c$ with some power law behavior

$$Q_\infty(T) \sim |T - T_c|^{-\omega}. \tag{2.4}$$

We can also think of this system as an infinite collection of infinite stripes, where the stripes are infinitely extended along one direction and stacked along the perpendicular direction. Now suppose there are only an N number of stripes. If N is finite, Q should be regular at $T = T_c$ since finite systems cannot have non-analyticities at $T \neq 0$. The singularity at $T = T_c$ should appear only when $N \to \infty$. The finite size scaling hypothesis assumes the existence of a scaling function F_Q such that

$$Q_N(T) \simeq Q_\infty(T) F_Q(N/\xi_\infty(T)), \tag{2.5}$$

where Q_N is the observable Q for a system with N stripes and Q_∞ corresponds to the system in the thermodynamic limit. ξ_∞ is the correlation length for the infinite system. Eq. (2.5) is valid when N is large. The correlation length also diverges as a power law near the critical point,

$$\xi_\infty(T) \sim |T - T_c|^{-\nu}. \tag{2.6}$$

Substituting Eq. (2.4) and (2.6) in Eq. (2.5),

$$Q_N(T) \simeq |T - T_c|^{-\omega} F_Q(N|T - T_c|^{\nu}). \tag{2.7}$$

Since $Q_N(T)$ should be regular at $T = T_c$, the scaling function should cancel the divergence due to $|T - T_c|^{-\omega}$. Therefore, the scaling function should be of the form $F_Q(x) \sim x^{\omega/\nu}$ as $x \to 0$. We should then have,

$$Q_N(T_c) \sim N^{\omega/\nu}. \tag{2.8}$$

If we define a function $\Delta_Q(T; N, N')$ such that

$$\Delta_Q(T; N, N') = \frac{\log(Q_N(T)/Q_{N'}(T))}{\log(N/N')}, \tag{2.9}$$

then the value of this function at $T = T_c$, $\Delta_Q(T_c; N, N') \simeq \omega/\nu$ is independent of N and N'. Therefore, for three different values N, N' and N'', the curves $\Delta_Q(T; N, N')$ and $\Delta_Q(T; N', N'')$ will intersect at the critical point $T = T_c$. This is how we can locate the critical point using the finite size scaling hypothesis.

We can also find the critical exponents ω and ν. Noting from Eq. (2.4) that

$$\frac{\partial Q_\infty(T)}{\partial T} \sim |T - T_c|^{-(\omega+1)}. \tag{2.10}$$

Therefore, we should have $\Delta_{\partial Q/\partial T}(T_c; N, N') \simeq (\omega+1)/\nu$. Define a new function $\Gamma_\omega(T; N, N')$ such that

$$\Gamma_\omega(T; N, N') = \frac{\Delta_Q(T; N, N')}{\Delta_{\partial Q/\partial T}(T; N, N') - \Delta_Q(T; N, N')}. \tag{2.11}$$

The value of this function at the critical point $\Gamma_\omega(T_c; N, N') \simeq \omega$ is independent of N and N' and gives us the critical exponent ω. Then ν can be determined using

$$\nu \simeq \frac{\omega}{\Delta_Q(T_c; N, N')}. \tag{2.12}$$

As we've already stated in the *Introduction*, this method cannot be used for the kinds of phase transitions we are interested in which occur at a finite system size. However, for such cases we can consider an extension of the approach discussed above [9–15]. In this extended approach, instead of truncating the system in the physical space, the system is truncated in the Hilbert space [15]. The FSS ansatz looks exactly the same except that N now represents the size of the set of basis states which spans the truncated Hilbert space [15]. Moreover, the temperature T will be replaced by the parameter g which is being tuned across the critical point. This approach has been shown by Kais and co-workers to work in the case of a particle in Yukawa potential [10, 12] and the calculation of electronic structure critical parameters for atomic and molecular systems [9, 11, 13–15].

2.2.3 Quantum Restricted Boltzmann Machine

Solving quantum many-body problem accurately has been a taxing numerical problem since the size of the wavefunction scales exponentially. The idea of taking advantage of the aspects of Machine Learning (ML) related to dimensionality reduction and feature extraction to capture the most relevant information came from the work by Carleo and Troyer [19], which introduced the idea of representing the many-body wavefunction in terms of an Artificial Neural Network (ANN) to solve for the ground states and time evolution for spin models. A Restricted Boltzmann Machine (RBM) was chosen as the architecture of this ANN. An RBM consists of a visible layer and a hidden layer with each neuron in the visible layer connected to all neurons in the hidden layer but the neurons within a layer are not connected to each other. The quantum state is ψ expanded in the basis $|x\rangle$:

$$|\psi\rangle = \sum \psi(x) \, |x\rangle \tag{2.13}$$

The Neural Network Quantum State (NQS) describes the wavefunction $\psi(x)$ to be written as $\psi(x;\theta)$, where θ represents the parameters of the RBM. $\psi(x;\theta)$ is now written in terms of the probability distribution that is obtained from the RBM as follows:

$$\psi(x;\theta) \propto \sum_{\{h\}} e^{\frac{1}{2}\sum_i a_i\sigma_i^z + \sum_j b_j h_j + \sum_{ij} w_{ij}\sigma_i^z h_j} \tag{2.14}$$

where, σ_i^z is the Pauli z operator at i^{th} site, σ_i^z and h_j take values $\{+1,-1\}$, $\theta = \{a_i, b_j, w_{ij}\}$ are the trainable bias and weight parameters of the RBM. Using stochastic optimization, the energy $E(\theta)$ is minimized.

This work was extended to obtain the ground states of the Bose-Hubbard model [20] and for the application of quantum state tomography [21].

With the rapid developments in the domains of ML and Quantum Computing (QC), the appetite for integrating ideas in both of these areas has been growing considerably. The last decade has seen a surge in the application of classical ML for quantum matter, wherein these methods have been adopted to benchmark, estimate and study the properties of quantum matter [22–25], with recently showing provable classification efficiency in classifying quantum states of matter [26]. The protocols and algorithms related to ML implementable on a quantum system so called Quantum machine Learning [27] is expected to have the potential of changing the course of fundamental scientific research [28] along with industrial pursuit.

In lieu of today's Noisy Intermediate Scale Quantum (NISQ) devices, the ideas which utilize both classical and quantum resources, such that the part of the problem which has an exponential scaling is implemented on the quantum platform while the rest are dealt with classically, are being carefully investigated for various applications. Such algorithms are known as classical-quantum hybrid algorithms. In the work by Xia and Kais [29], a modified RBM with three layers was introduced, the third layer to account for the sign of

the wavefunction, to solve for the ground state energies of molecules. Now, the parametrized wavefunction $\psi(x;\theta)$ is written as a function of $P(x)$ along with a sign function $s(x)$:

$$P(\mathbf{x}) = \frac{\sum_{\{h\}} e^{\sum_i a_i \sigma_i^z + \sum_j b_j h_j + \sum_{ij} w_{ij} \sigma_i^z h_j}}{\sum_{\mathbf{x}'} \sum_{\{h\}} e^{\sum_i a_i \sigma_i^{z'} + \sum_j b_j h_j + \sum_{ij} w_{ij} \sigma_i^{z'} h_j}} \tag{2.15}$$

$$s(\mathbf{x}) = \tanh\left[(c + \sum_i d_i \sigma_i)\right] \tag{2.16}$$

The wavefunction ansatz in terms of the RBM can be expressed as [29]:

$$|\psi\rangle = \sum_x \sqrt{P(x)} s(x) |x\rangle \tag{2.17}$$

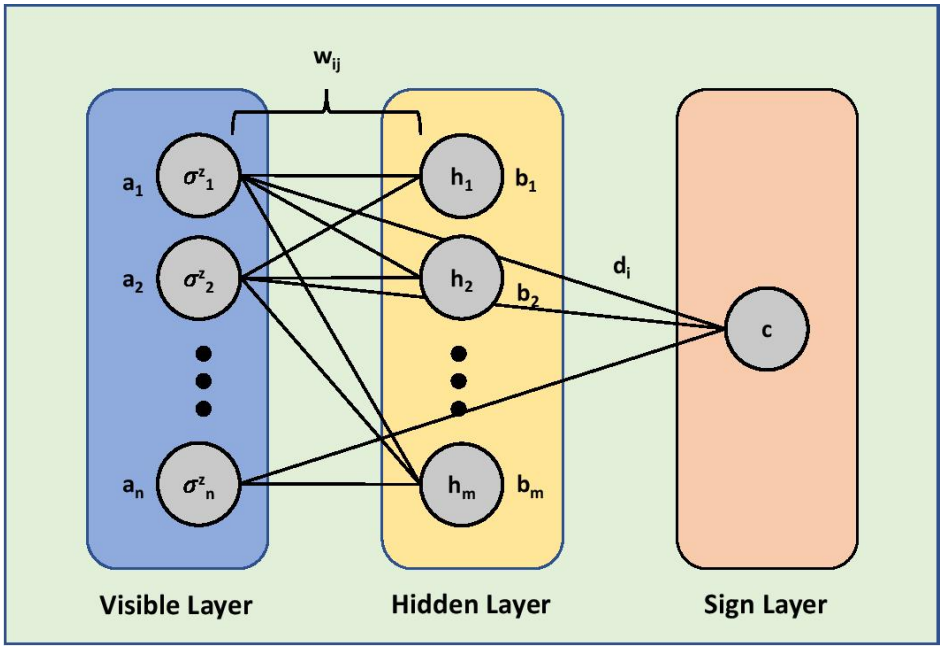

Figure 2.2. Restricted Boltzmann Machine architecture. The first layer is the visible layer with bias parameters denoted by a_i. The second layer is the hidden layer with bias parameters denoted by b_j. The third layer is the sign layer with bias parameters denoted by c. The weights associated with the connections between the visible neurons and the hidden neurons are designated by w_{ij}. The weights associated with the connections between the visible neurons and the neuron of the sign layer are designated by d_i.

A quantum circuit comprising of a single-qubit (R_y) and multi-qubit y-rotation gates ($C1-C2-R_y$) are employed, to sample the Gibbs distribution. The utilization of R_y gates cater to the bias parameter of visible and hidden layers part of the distribution, while $C1-C2-R_y$ gates tend to the weights part of the distribution. In the work by Sureshbabu et al. [30], the implementation of such a circuit on IBM-Q devices were shown, wherein a new ancillary qubit is introduced to store the value corresponding to every $C1-C2-R_y$ gate (Fig. 2.3). The term n denotes the number of visible qubits and m denotes the number of hidden units. In this formalism, the number of ancillary qubits required are $n \times m$. Starting all the qubits from a $|0\rangle$, the R_y and $C1-C2-R_y$ rotations are performed, and a measurement is performed on all the qubits. If all the ancillary qubits are in $|1\rangle$, then the sampling is deemed successful and the states corresponding to the first $m+n$ qubits provide the distribution $P(x)$. The joint probability distribution defined over the parameters of the circuit $\theta = \{a, b, w\}$ and a set of $y = \{\sigma^z, h\}$ is given by:

$$P(y,\theta) = \frac{e^{\sum_i a_i \sigma_i^z + \sum_j b_j h_j + \sum_{ij} w_{ij} \sigma_i^z h_j}}{\sum_{\{y\}} e^{\sum_i a_i \sigma_i^{z'} + \sum_j b_j h_j + \sum_{ij} w_{ij} \sigma_i^{z'} h_j}} \tag{2.18}$$

The probability of successful sampling can be improved by rewriting the distribution $P(y,\theta)$ as $Q(y,\theta)$ and setting $k = max(1, \frac{|w_{ij}|}{2})$ [29, 31]:

$$Q(y,\theta) = \frac{e^{\frac{1}{k}(\sum_i a_i \sigma_i^z + \sum_j b_j h_j + \sum_{ij} w_{ij} \sigma_i^z h_j)}}{\sum_{\{y\}} e^{\frac{1}{k}(\sum_i a_i \sigma_i^{z'} + \sum_j b_j h_j + \sum_{ij} w_{ij} \sigma_i^{z'} h_j)}} \tag{2.19}$$

Firstly, the QRBM is implemented classically, i.e, the quantum circuit is simulated on a classical computer. This execution caters to the ideal results that can be obtained through the QRBM algorithm. Then, the quantum circuit is implemented on the Digital Quantum Simulator, the *qasm* simulation backend. This simulator is part of the high-performance simulators from IBM-Q. The circuit is realized using IBM's Quantum Information Software Toolkit titled Qiskit [32]. Though no noise model was utilized, as a result of finite sampling, statistical fluctuations in the values of probabilities in observing the circuit in the measurement basis, are present in the obtained results.

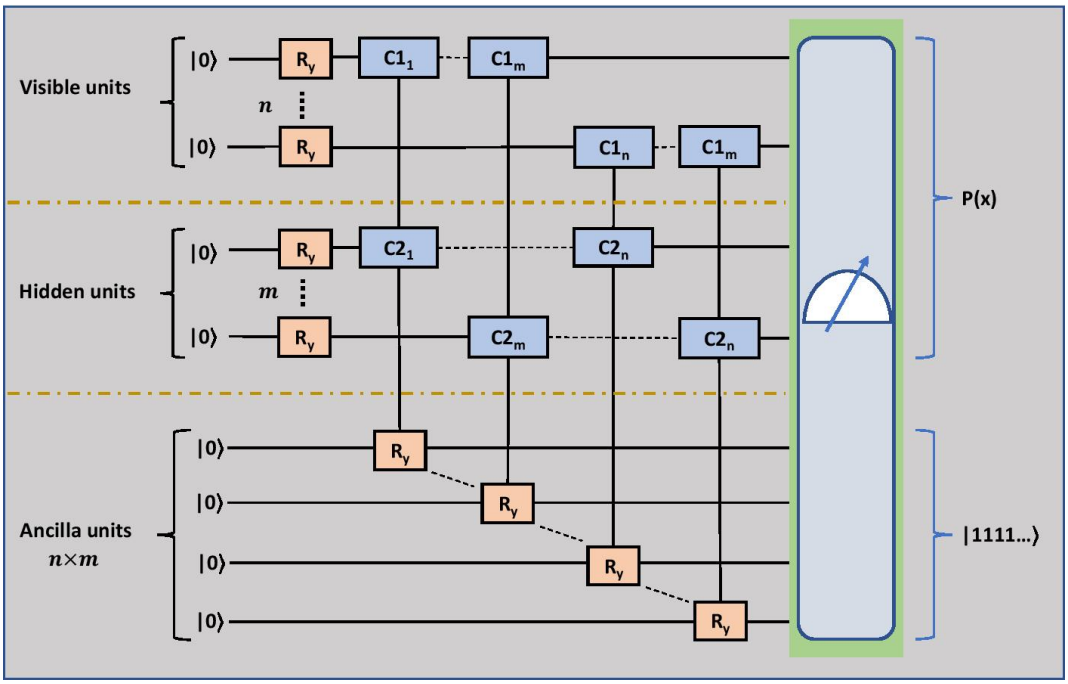

Figure 2.3. The quantum circuit to sample the Gibbs distribution. n is the number of qubits belonging to the visible layer and m is the number of qubits belonging to the hidden layer. There are $m \times n$ ancillary qubits.

Having obtained the distribution $Q(y, \theta)$, the probabilities are raised to the power of k, to get $P(y, \theta)$. Following this, the sign function is computed classically, thereby calculating $|\psi\rangle$. Then, the expectation value for the Hamiltonian H $[\langle\Psi| H |\Psi\rangle]$ is computed to get the energy, which is minimized using gradient descent to obtain the ground state eigenenergy of H.

The resource requirements demanded by this algorithm are quadratic. The number of qubits required are $(m+n)$ to encode the visible and hidden nodes, and $(m \times n)$ to account for the ancillary qubits. Hence, the number of qubits scales as $O(mn)$. The number of R_y gates required are $(m+n)$ and the number of $C1-C2-R_y$ gates required are $(m \times n)$. In addition, each $C1-C2-R_y$ gate requires $6n$ X-gates to account for all the states spanned by the control qubits. Therefore, the number of gates required also scales as $O(mn)$. Obtaining the ground states or minimum eigenvalues of a given matrix using exact diagonalization has a complexity of $\approx j^3$, with j being the dimension of the column space for the given matrix [33].

2.3 Results

2.3.1 Exact Diagonalization

In this section, we demonstrate the calculation of the critical point of the Quantum Rabi model using the Finite-Size Scaling method. As discussed before, the phase transition in QRM occurs only in the limit $\Omega/\omega_0 \to \infty$. This limit is not straightforward to implement in H_{Rabi} given in Eq. (2.1). Instead, we have considered the effective low-energy Hamiltonians H_{np} and H_{sp} given in Eq. (2.2) and (2.3) respectively. In H_{np} and H_{sp}, Ω is involved only in a constant term which can be removed from the Hamiltonians and the limit $\Omega/\omega_0 \to \infty$ can then be easily imposed.

In H_{np} and H_{sp}, the degrees of freedom of the two-level system have been traced out and the only degrees of freedom we have are those of the bosonic mode. Let's first consider the *normal phase* Hamiltonian H_{np}. The Hilbert space for this Hamiltonian is spanned by the familiar harmonic oscillator number states $\{|0\rangle, |1\rangle, |2\rangle, \ldots\}$. We can truncate the full Hilbert space to an N-dimensional Hilbert space spanned by $\{|0\rangle, |1\rangle, \ldots, |N-1\rangle\}$ to apply the finite-size scaling analysis. In this restricted Hilbert space, the matrix form of $H_{np}^{(N)}$ can be found by using $a|m\rangle = \sqrt{m}\,|m-1\rangle$ and $a^\dagger|m\rangle = \sqrt{m+1}\,|m+1\rangle$. Once we have the matrix form, we can then use the exact diagonalization method to find the ground state of $H_{np}^{(N)}$ with energy $E_{np}^{(N)}$.

Consider the scaling law for the ground state energy in the vicinity of the critical point $g = g_c$,

$$E(g) \sim |g - g_c|^\alpha. \tag{2.20}$$

Here E is the ground state energy. We slightly modify the formula in Eq. (2.9) to take into account the difference in the signs of the exponents in Eq. (2.4) and (2.20). The new formula with $Q = E$ is,

$$\Delta_{H_{np}}(g; N, N') = \frac{\log\left(E_{np}^{(N)}(g)/E_{np}^{(N')}(g)\right)}{\log(N'/N)}, \tag{2.21}$$

We plot the curves $\Delta_{H_{np}}(g; N, N+2)$ for $N = 8, 10, \ldots, 30$ in Fig. 2.4(a). We then plot the intersection points $g_{np}^{(N)}$ of the curves $\Delta_{H_{np}}(g; N-4, N-2)$ and $\Delta_{H_{np}}(g; N-2, N)$ as a function of N as shown in Fig. 2.4(b). To find the limit of $g_{np}^{(N)}$ as $N \to \infty$, we used the

Bulirsch-Stoer algorithm (see supplementary information S-I). The limit was calculated to be $g_{np}^{(N)} \to 0.999996$. So $g_c^{(np)} = 0.999996$.

In a similar way, we then consider H_{sp}. The curves $\Delta_{H_{sp}}(g; N, N+2)$ are plotted in Fig. 2.4(c) for $N = 8, 10, \ldots, 30$ and the intersection points $g_{sp}^{(N)}$ are plotted in Fig. 2.4(d) as a function of N. In this case, the extrapolation to $N \to \infty$ gives the critical value $g_c^{(sp)} = 0.999987$. Both the calculated values of $g_c^{(np)}$ and $g_c^{(sp)}$ are very close to the exact value $g_c = 1$.

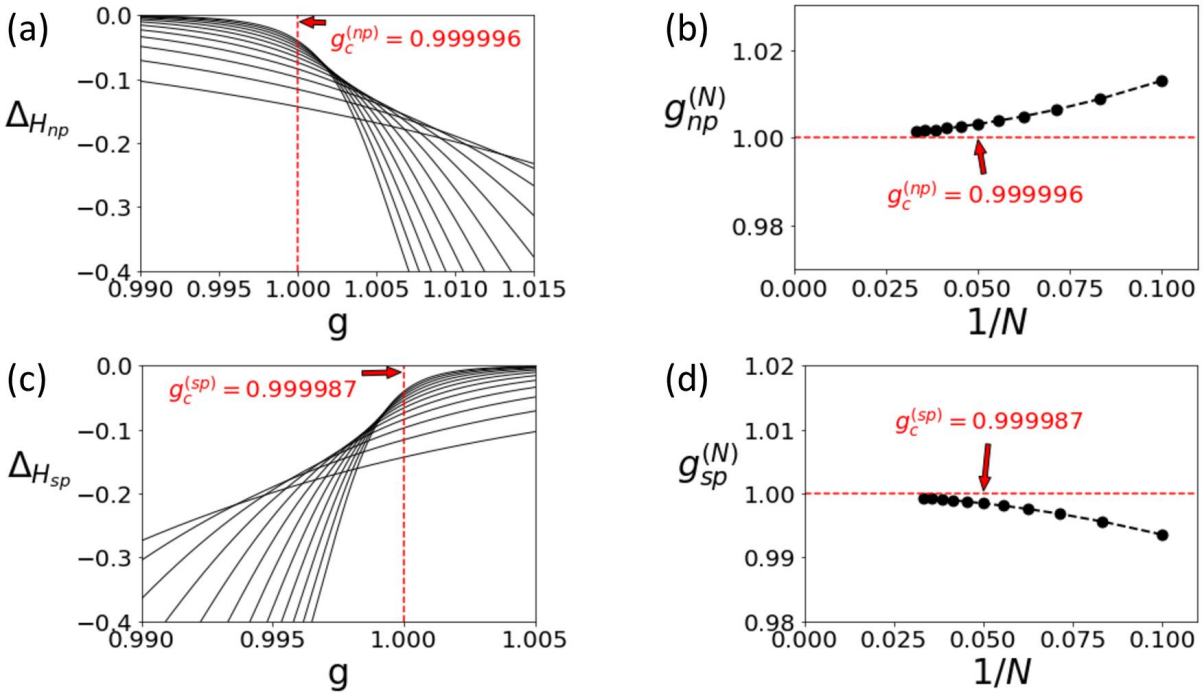

Figure 2.4. Finite-Size Scaling for Quantum Rabi model. We used $N = 8, 10, \ldots, 32$. (a) Graphs of $\Delta_{H_{np}}(g; 8, 10)$, $\Delta_{H_{np}}(g; 10, 12), \ldots, \Delta_{H_{np}}(g; 30, 32)$ as a function of g. (b) Intersection points $g_{np}^{(N)}$ where $\Delta_{H_{np}}(g_{np}^{(N)}; N-4, N-2) = \Delta_{H_{np}}(g_{np}^{(N)}; N-2, N)$, as a function of $1/N$. As $N \to \infty$, $g_{np}^{(N)} \to 0.999996$. So, $g_c^{(np)} = 0.999996$. (c) Graphs of $\Delta_{H_{sp}}(g; 8, 10)$, $\Delta_{H_{sp}}(g; 10, 12), \ldots, \Delta_{H_{sp}}(g; 30, 32)$ as a function of g. (d) Intersection points $g_{sp}^{(N)}$ where $\Delta_{H_{sp}}(g_{sp}^{(N)}; N-4, N-2) = \Delta_{H_{sp}}(g_{sp}^{(N)}; N-2, N)$, as a function of $1/N$. As $N \to \infty$, $g_{sp}^{(N)} \to 0.999987$. So, $g_c^{(sp)} = 0.999987$.

2.3.2 Quantum Restricted Boltzmann Machine

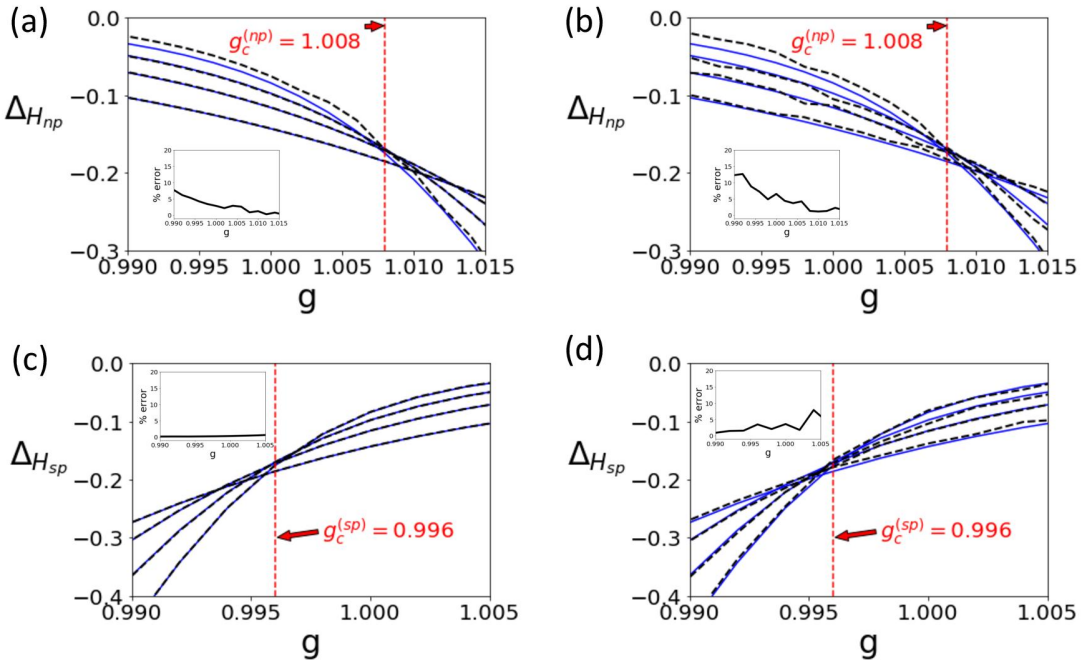

Figure 2.5. QRBM Implementation of FSS for QRM. The light blue line represents results obtained from exact diagonalization and dashed black line represents QRBM results. (a) Classical implementation of QRBM corresponding to normal phase, graphs of $\Delta_{H_{np}}(g; 8, 10)$, $\Delta_{H_{np}}(g; 10, 12), \ldots,$ $\Delta_{H_{np}}(g; 14, 16)$ as a function of g. (b) QRBM implemented on *qasm* simulator corresponding to normal phase, graphs of $\Delta_{H_{np}}(g; 8, 10)$, $\Delta_{H_{np}}(g; 10, 12), \ldots,$ $\Delta_{H_{np}}(g; 14, 16)$ as a function of g. The $g_c^{(np)}$ in both the cases is calculated to be 1.008. (c) Classical implementation of QRBM corresponding to superradiant phase, graphs of $\Delta_{H_{sp}}(g; 8, 10)$, $\Delta_{H_{sp}}(g; 10, 12), \ldots,$ $\Delta_{H_{sp}}(g; 14, 16)$ as a function of g. (b) QRBM implemented on *qasm* simulator corresponding to superradiant phase, graphs of $\Delta_{H_{sp}}(g; 8, 10)$, $\Delta_{H_{sp}}(g; 10, 12), \ldots,$ $\Delta_{H_{sp}}(g; 14, 16)$ as a function of g. The $g_c^{(sp)}$ in both the cases is calculated to be 0.996. The inset plots display the mean percentage error between the exact diagonalization results and QRBM results.

Now we illustrate the implementation of the FSS method using the QRBM algorithm. The results are shown in Fig. 2.5. Fig. 2.5(a) and Fig. 2.5(c) show the results for H_{np} and H_{sp} using the classical implementation of the algorithm respectively. Whereas, Fig. 2.5(b) and Fig. 2.5(d) correspond to the results for H_{np} and H_{sp} when the algorithm is implemented

using the *qasm* simulator from IBM-Q respectively. The QRBM algorithm is run for $N = 8, 10, 12, 14, 16$.

For the case of N=8, the number of qubits associated with the visible nodes equal 3, the number of qubits associated with the hidden nodes equal 3, and 9 ancillary qubits were used. The quantum circuit consists of 6 R_y gates associated with the bias parameters, 9 $C1 - C2 - R_y$ gates associated with the weights. Since, each $C1 - C2 - R_y$ gate requires 6 X-gates, a total of 54 X-gates were used. For the case of N=10,..,16, the number of qubits associated with the visible nodes equal 4, the number of qubits associated with the hidden nodes equal 4, and 16 ancillary qubits were used. The quantum circuit consists of 8 R_y gates associated with the bias parameters, 16 $C1 - C2 - R_y$ gates associated with the weights. Since, each $C1 - C2 - R_y$ gate requires 6 X-gates, a total of 96 X-gates were used.

Starting from random initialization, all parameters are updated via gradient descent. A learning rate of 0.01 was chosen and the algorithm is run for around 30,000 iterations. In order to assist with the convergence to the minimum eigenenergies, warm starting is employed. The method of warm starting is essentially initializing the parameters of the current point with the parameters of a previously converged point of calculation, which helps in avoiding the convergence to a local minima.

The black curves plotted in the insets in Fig. 2.5 represent the deviation of the QRBM results (black dashed curves) from the exact diagonalization results (blue solid curves). They were calculated using the average of the quantity $\left|\Delta^{(ED)}(g) - \Delta^{(QRBM)}(g)/\Delta^{(ED)}(g)\right| \times 100$ over all the four curves. An enlarged version of the error plots can be found in supplementary information S-II. For each case the overall error close to $g = 1.000$ is not more than $\sim 5\%$ which implies convergence to the right result. Moreover, for the case of H_{sp}, we notice that the error is very small for the classical implementation i.e. $\sim< 1\%$ throughout the range of the graph. An astoundingly low error for this particular case shows that the QRBM method is particularly effective in finding the correct ground state for the case of H_{sp}. Overall this result also underscores the fact that QRBM can be more effective for certain forms of the Hamiltonian over others, such as in this case it was quite effective for H_{sp} even with a relatively small number of qubits used in the hidden layer.

The critical point using H_{np} was found to be $g_c^{(np)} = 1.008$ for both the classical and *qasm* implementations. Similarly, the critical point for the case of H_{sp} was found to be $g_c^{(sp)} = 0.996$ for both the classical and *qasm* implementations. Here we notice that although, the convergence for the data obtained from both the classical and *qasm* implementations turns out to be the same for both H_{np} and H_{sp}, such a perfect match appears to be somewhat coincidental. In see supplementary information S-I, we have explained the Bulirsch-Stoer algorithm which sets the criteria used to deduce these convergence results. The convergence plots have been added to the *Supporting Information* section.

2.4 Discussion and Outlook

In this chapter we have used the Finite-Size Scaling in Hilbert Space approach to calculate the critical point of the Quantum Rabi Model. We used the low-energy effective Hamiltonians for both the normal and superradiant phases respectively to show that the critical point is $g_c \approx 1$. The original FSS approach in which the truncation is done in the physical space has been widely used to calculate critical points and critical exponents since its inception. However that approach was not applicable to Quantum Phase Transitions which occur at a finite system size. With the rise in interest in QPTs occurring in these finite size systems, our approach provides a natural extension of the original FSS method to study such phase transitions. To our knowledge, this is the first time this approach has been used to study a QPT in a light-matter interaction system.

We have also provided a recipe for the implementation of this method on a universal quantum computer using the Quantum Restricted Boltzmann Machine algorithm. It was shown that results obtained from the classical gate simulation match those obtained from the IBM-Q's *qasm* simulator. Such an implementation scales quadratically while the exact diagonalization scales cubically in the best case and exponentially in the worst case. Looking forward, we are interested in applying this approach to other QPTs such as the QPT in anisotropic QRM. We would also like to use our method to calculate the critical exponents in addition to the critical points in these phase transitions. It would also be interesting

to see if this approach can be used to predict any new phase transition for some other non-integrable model.

Another very promising research direction is to implement the FSS method for phase transitions in classically intractable many-body models such as exotic electronic and magnetic systems. These include general quantum materials, for example where Coulomb potential leads to a gapped spectrum in energy, including in direct band-gap semiconductors in the thermodynamic limit. Conventionally speaking, it might be necessary to resort to the original finite-size scaling in the physical space approach for these systems since they exhibit criticality only in the limit $N \to \infty$. However, the ground state of an appropriately truncated Hamiltonian could be deduced using the QRBM algorithm as shown in the chapter towards efficient implementation on a digital quantum simulator. A simile can also be drawn between a many-body bulk gap separating a continuum of excited states from the ground state manifold to the gapped Rabi model discussed in this chapter. Such an approach can be useful in emergent topological systems, such as in Weyl semimetals, 1-D Kitaev spin chains, quantum spin liquids, and others, on which there is a tremendous explosion of interest [34–39]. Topological phase transitions are devoid of any conventional order parameter and a quantum solution deriving from the approach outlines in this chapter can help us bypass resource and scaling limitations of DMRG and exact diagonalization approaches to calculate the critical point and the critical exponents.

Bibliography

[1]N. Goldenfeld, *Lectures on phase transitions and the renormalization group*, Frontiers in Physics (Addison-Wesley Publishing Company, 1992).

[2]M.-J. Hwang, R. Puebla, and M. B. Plenio, "Quantum phase transition and universal dynamics in the rabi model," Phys. Rev. Lett. **115**, 180404 (2015).

[3]M.-J. Hwang and M. B. Plenio, "Quantum phase transition in the finite jaynes-cummings lattice systems," Phys. Rev. Lett. **117**, 123602 (2016).

[4]M. Liu, S. Chesi, Z.-J. Ying, X. Chen, H.-G. Luo, and H.-Q. Lin, "Universal scaling and critical exponents of the anisotropic quantum rabi model," Phys. Rev. Lett. **119**, 220601 (2017).

[5]M.-J. Hwang, P. Rabl, and M. B. Plenio, "Dissipative phase transition in the open quantum rabi model," Phys. Rev. A **97**, 013825 (2018).

[6]Y.-F. Xie, X.-Y. Chen, X.-F. Dong, and Q.-H. Chen, "First-order and continuous quantum phase transitions in the anisotropic quantum rabi-stark model," Phys. Rev. A **101**, 053803 (2020).

[7]M.-L. Cai, Z.-D. Liu, W.-D. Zhao, et al., "Observation of a quantum phase transition in the quantum Rabi model with a single trapped ion," Nat Commun **12**, 1126 (2021).

[8]B. Derrida and L. D. Seze, "Application of the phenomenological renormalization to percolation and lattice animals in dimension 2," in *Finite-size scaling*, Vol. 2, edited by J. L. CARDY, Current Physics–Sources and Comments (Elsevier, 1988), pp. 275–283.

[9]J. P. Neirotti, P. Serra, and S. Kais, "Electronic structure critical parameters from finite-size scaling," Phys. Rev. Lett. **79**, 3142–3145 (1997).

[10]P. Serra, J. P. Neirotti, and S. Kais, "Finite-size scaling approach for the schrödinger equation," Phys. Rev. A **57**, R1481–R1484 (1998).

[11]P. Serra, J. P. Neirotti, and S. Kais, "Electronic structure critical parameters for the lithium isoelectronic series," Phys. Rev. Lett. **80**, 5293–5296 (1998).

[12]P. Serra, J. P. Neirotti, and S. Kais, "Finite size scaling in quantum mechanics," J. Phys. Chem. A **102**, 9518–9522 (1998).

[13]S. Kais and P. Serra, "Quantum critical phenomena and stability of atomic and molecular ions," International Reviews in Physical Chemistry **19**, 97–121 (2000).

[14]Q. Shi and S. Kais, "Finite size scaling for critical parameters of simple diatomic molecules," Molecular Physics **98**, 1485–1493 (2000).

[15]S. Kais and P. Serra, "Finite size scaling for atomic and molecular systems," Advances in Chemical Physics, Volume 125, 1–100 (2003).

[16]A. Francis, D. Zhu, C. H. Alderete, S. Johri, X. Xiao, J. K. Freericks, C. Monroe, N. M. Linke, and A. F. Kemper, "Many-body thermodynamics on quantum computers via partition function zeros," Science Advances **7**, eabf2447 (2021).

[17]A. Keesling, A. Omran, H. Levine, et al., "Quantum kibble–zurek mechanism and critical dynamics on a programmable rydberg simulator," Nature **568**, 207–211 (2019).

[18]M. Dupont and J. E. Moore, "Quantum criticality using a superconducting quantum processor," arXiv:2109.10909 (2021).

[19]G. Carleo and M. Troyer, "Solving the quantum many-body problem with artificial neural networks," Science **355**, 602–606 (2017).

[20]H. Saito, "Solving the bose–hubbard model with machine learning," Journal of the Physical Society of Japan **86**, 093001 (2017).

[21]G. Torlai, G. Mazzola, J. Carrasquilla, M. Troyer, R. Melko, and G. Carleo, "Neural-network quantum state tomography," Nature Physics **14**, 447–450 (2018).

[22]J. Carrasquilla and R. G. Melko, "Machine learning phases of matter," Nature Physics **13**, 431–434 (2017).

[23]D.-L. Deng, X. Li, and S. D. Sarma, "Machine learning topological states," Physical Review B **96**, 195145 (2017).

[24]K. T. Butler, D. W. Davies, H. Cartwright, O. Isayev, and A. Walsh, "Machine learning for molecular and materials science," Nature **559**, 547–555 (2018).

[25]G. Carleo, I. Cirac, K. Cranmer, L. Daudet, M. Schuld, N. Tishby, L. Vogt-Maranto, and L. Zdeborová, "Machine learning and the physical sciences," Reviews of Modern Physics **91**, 045002 (2019).

[26]H.-Y. Huang, R. Kueng, G. Torlai, V. V. Albert, and J. Preskill, "Provably efficient machine learning for quantum many-body problems," arXiv preprint arXiv:2106.12627 (2021).

[27]J. Biamonte, P. Wittek, N. Pancotti, P. Rebentrost, N. Wiebe, and S. Lloyd, "Quantum machine learning," Nature **549**, 195–202 (2017).

[28]M. Sajjan, J. Li, R. Selvarajan, S. H. Sureshbabu, S. S. Kale, R. Gupta, and S. Kais, "Quantum computing enhanced machine learning for physico-chemical applications," arXiv preprint arXiv:2111.00851 (2021).

[29]R. Xia and S. Kais, "Quantum machine learning for electronic structure calculations," Nature communications **9**, 1–6 (2018).

[30]S. H. Sureshbabu, M. Sajjan, S. Oh, and S. Kais, "Implementation of quantum machine learning for electronic structure calculations of periodic systems on quantum computing devices," Journal of Chemical Information and Modeling (2021).

[31]M. Sajjan, S. H. Sureshbabu, and S. Kais, "Quantum machine-learning for eigenstate filtration in two-dimensional materials," Journal of the American Chemical Society **143**, PMID: 34705449, 18426–18445 (2021).

[32]G. Aleksandrowicz, T. Alexander, P. Barkoutsos, L. Bello, Y. Ben-Haim, D. Bucher, F. Cabrera-Hernández, J. Carballo-Franquis, A. Chen, C. Chen, et al., "Qiskit: an open-source framework for quantum computing," Accessed on: Mar **16** (2019).

[33]C. R. Harris, K. J. Millman, S. J. van der Walt, R. Gommers, P. Virtanen, D. Cournapeau, E. Wieser, J. Taylor, S. Berg, N. J. Smith, et al., "Array programming with numpy," Nature **585**, 357–362 (2020).

[34]K. J. Satzinger, Y.-J. Liu, A. Smith, C. Knapp, et al., "Realizing topologically ordered states on a quantum processor," Science **374**, 1237–1241 (2021).

[35]A. Kitaev, "Anyons in an exactly solved model and beyond," Annals of Physics **321**, January Special Issue, 2–111 (2006).

[36]Y.-J. Liu, K. Shtengel, A. Smith, and F. Pollmann, "Methods for simulating string-net states and anyons on a digital quantum computer," arXiv:2110.02020 (2021).

[37]X. Xiao, J. K. Freericks, and A. F. Kemper, "Determining quantum phase diagrams of topological Kitaev-inspired models on NISQ quantum hardware," Quantum **5**, 553 (2021).

[38]X.-G. Wen, "Colloquium: zoo of quantum-topological phases of matter," Rev. Mod. Phys. **89**, 041004 (2017).

[39]M. Z. Hasan and C. L. Kane, "Colloquium: topological insulators," Rev. Mod. Phys. **82**, 3045–3067 (2010).

[40]R. Bulirsch and J. Stoer, "Numerical treatment of ordinary differential equations by extrapolation methods," Numer. Math. **8**, 1–13 (1966).

[41]M. Henkel and G. Schutz, "Finite-lattice extrapolation algorithms," **21**, 2617–2633 (1988).

Supplementary Information

S-I Bulirsch-Stoer Algorithm

For $h_N = 1/N$ where $N = 0, 1, 2, \ldots$, the Bulirsch-Stoer algorithm can be used to find the limit of a function $T(h_N)$ as $N \to \infty$ [40, 41]. For demonstration, consider that we only have $T(h_N)$ for $N = 0, 1, 2, 3$, then the following rows are computed successively,

$$
\begin{array}{lcccccc}
n=0 & T_0^{(0)} & & T_0^{(1)} & & T_0^{(2)} & & T_0^{(3)} \\
n=1 & & T_1^{(0)} & & T_1^{(1)} & & T_1^{(2)} & \\
n=2 & & & T_2^{(0)} & & T_2^{(1)} & & \\
n=3 & & & & T_3^{(0)} & & &
\end{array}
$$

using the following rules

$$T_{-1}^{(N)} = 0 \tag{2.22}$$

$$T_0^{(N)} = T(h_N) \tag{2.23}$$

$$T_{m\geq 1}^{(N)} = T_{m-1}^{(N+1)} + (T_{m-1}^{(N+1)} - T_{m-1}^{(N)}) \left[\left(\frac{h_N}{h_{N+m}} \right)^{\omega} \left(1 - \frac{T_{m-1}^{(N+1)} - T_{m-1}^{(N)}}{T_{m-1}^{(N+1)} - T_{m-2}^{(N+1)}} \right) - 1 \right]^{-1} \tag{2.24}$$

where ω is a free parameter determined by minimizing $\varepsilon_m^{(i)} = \left| T_m^{(i+1)} - T_m^{(i)} \right|$. The final answer is $T_3^{(0)}$.

S-II Error Plots

Fig. 2.6 displays the enlarged error plots included in the insets of Fig. 2.5. Fig. 2.7 shows the convergence plots for the data in Fig. 2.5.

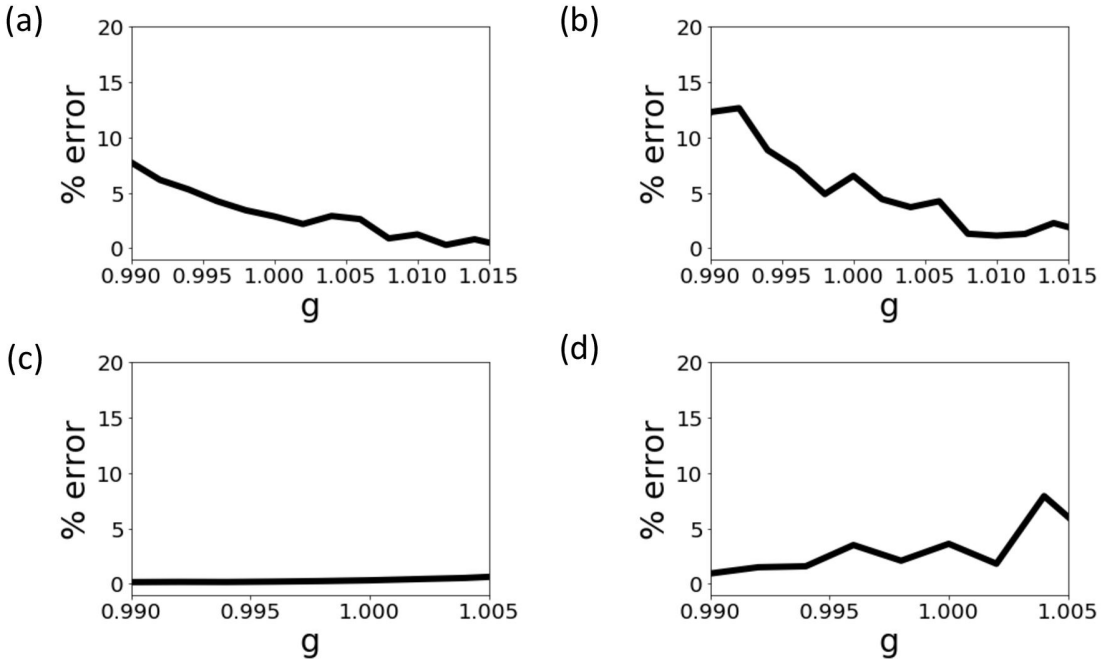

Figure 2.6. Error plots from the insets of Fig 2.5.

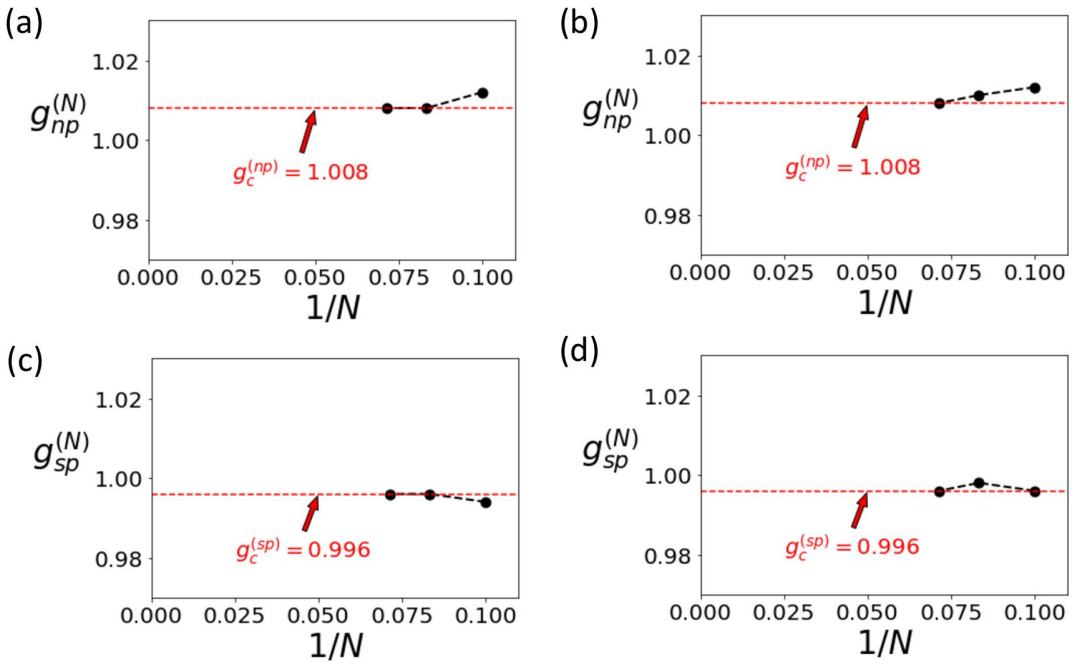

Figure 2.7. Convergence diagrams for results in Fig 2.5. (a), (b), (c), (d) correspond to convergence results for data in Fig. 2.5(a), (b), (c), (d) respectively. The same procedure was used as the one shown in Fig. 2.4(b) and (d).

3. PROJECT II: GROUND STATES OF FRUSTRATED ISING HAMILTONIANS

The contents of this chapter are adapted from the following article:

P. C. Lotshaw, H. Xu, B. Khalid, G, Buchs, T. S. Humble and A. Banerjee, "Simulations of frustrated Ising Hamiltonians using quantum approximate optimization", Phil. Trans. R. Soc. A.38120210414 (2023.)

Abstract: *Novel magnetic materials are important for future technological advances. Theoretical and numerical calculations of ground state properties are essential in understanding these materials, however, computational complexity limits conventional methods for studying these states. Here we investigate an alternative approach to preparing materials ground states using the quantum approximate optimization algorithm (QAOA) on near-term quantum computers. We study classical Ising spin models on unit cells of square, Shastry-Sutherland, and triangular lattices, with varying field amplitudes and couplings in the material Hamiltonian. We find relationships between the theoretical QAOA success probability and the structure of the ground state, indicating that only a modest number of measurements ($\lesssim 100$) are needed to find the ground state of our nine-spin Hamiltonians, even for parameters leading to frustrated magnetism. We further demonstrate the approach in calculations on a trapped-ion quantum computer and succeed in recovering each ground state of the Shastry-Sutherland unit cell with probabilities close to ideal theoretical values. The results demonstrate the viability of QAOA for materials ground state preparation in the frustrated Ising limit, giving important first steps towards larger sizes and more complex Hamiltonians where quantum computational advantage may prove essential in developing a systematic understanding of novel materials.*

3.1 Introduction

Quantum magnetism has been a major focus in condensed matter research, driven by the potential for new disruptive applications ranging from quantum computing to quantum sensing [1]. Quantum material properties are intrinsically related to the structure of the ground states. However, exact ground states are notoriously challenging to calculate classically, requiring the field to resort to using semi-classical limits [2–5] or fully quantum approaches with restricted applicability [6–12]. New, fully quantum computational tools are required to understand current problems including frustrated two-dimensional quantum magnets currently explored by bulk neutron scattering and thin film susceptibility [13, 14]. Digital and analog quantum simulators have emerged as a new tool for the simulation of quantum many-body phenomena towards efficient modeling of exotic quantum phases of matter beyond classical tractability [15, 16]. They are naturally suited for magnetic Hamiltonians since spins can be directly mapped to qubits. Non-trivial phases in magnetic systems, such as frustrated phases [17] , spin glasses [18], and topologically ordered phases [19, 20] have been realized on multiple qubit platforms using a variety of techniques.

In this paper, we investigate an alternative approach to preparing materials ground states using the quantum approximate optimization algorithm (QAOA) [21] on near-term quantum computers. We apply QAOA to lattices of interest in materials science, considering the classical Ising limit (equivalently, $S = \infty$) where standard QAOA is directly applicable. This serves as a stepping stone towards truly quantum problems such as the XY and Heisenberg models in the fully frustrated limit, which will require further algorithmic research and modifications to the approach presented here. Our results validate that QAOA achieves sufficient accuracy for the simpler classical limit and provides insights into algorithmic behavior for material lattice problems.

We consider lattice instances with varying degrees of frustration. The smallest building block of a frustrated magnetic Hamiltonian is an anti-ferromagnetic triangular motif of three spins where all the bonds cannot be satisfied simultaneously. In these materials, exchange interactions compete such that it is impossible to satisfy them all simultaneously, see Fig. 3.1.

If all spin configurations are equally favorable, frustration can lead to non-ordered states such as spin liquids [5], spin glasses [22], or plaquette states [8], each with distinct signatures.

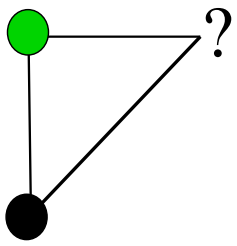

Figure 3.1. Example of frustration on an anti-ferromagnetic triangular motif. Two spins in opposite orientations (black and green) minimize the energy along one bond, however, there is no configuration for the final spin that minimizes energy along both remaining bonds.

We solve three different types of Hamiltonians for unit cells pictured in Fig. 3.2. The first is a square unit cell Hamiltonian, which exhibits only simple ferromagnetic and anti-ferromagnetic phases in the infinite size (thermodynamic) limit. The second is the celebrated Shastry-Sutherland lattice. Interestingly, this problem already lends itself to materials applications and experimental data analysis. Among other examples, it is conjectured to describe the class of rare-earth tetraborides (ErB_4, TmB_4 and NdB_4) and allows a direct comparison with several existing results both theoretical [23–27] and experimental [28–33]. The third case is the more complex Ising triangular lattice which represents a maximally frustrated problem with an infinite number of possible ground states in the infinite size limit [34, 35]. We compute theoretical probabilities to prepare the ground state for each of these 9-spin Hamiltonians under varying choices of the external field and coupling parameters and compare these theoretical results against computations on a trapped ion quantum computer.

We choose $N = 9$ spins as this is the logical minimum number of spins required to construct a unit cell of the Shastry Sutherland lattice and also it is a feasible size for the Quantinuum quantum computer (with 12 qubits available at the time this work was completed). We focus on $p = 1$ layers of the QAOA algorithm; for larger N instances more layers p of QAOA will be needed to maintain a significant success probability [36–38]. Implementations on quantum computers will also have to overcome predicted limitations due to noise [39–42] including an exponential scaling in the number of measurements with circuit

size, depth, and other factors [43]. Noise in modern quantum computers has negative consequences for all quantum algorithms, not only QAOA. Ongoing testing and development of these devices is necessary to assess realistic performance scaling in the presence of noise and to determine whether QAOA, or other quantum algorithms, will ultimately succeed in providing a useful computational advantage over conventional approaches.

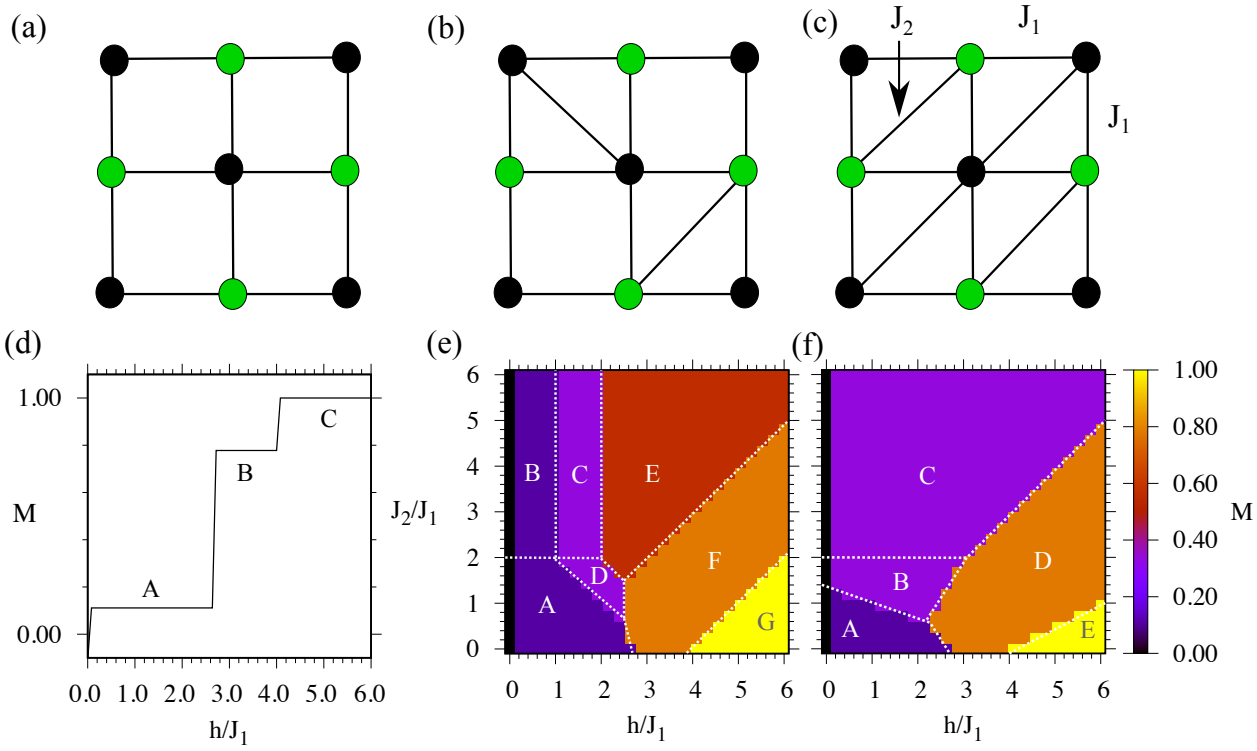

Figure 3.2. Unit cells of (a) square, (b) Shastry-Sutherland, and (c) triangular geometries. Colors indicate two spin values $s_i = \pm 1$ in examples of ground states with $h/J_1, J_2/J_1, \ll 1$. (d-f) phase diagrams for each of the unit cells (a-c) respectively, with labels "A", "B",... denoting regions with distinct ground states for each lattice. Magnetization $M = 0$ at $h = 0$ is due to degeneracy in the ground states, where spin-flip-related pairs of states are present in absence of the field ($h = 0$).

3.2 Ising Hamiltonian and Model Unit Cell Lattices

A single unpaired spin on the outermost orbital of a magnetic ion constitutes a $s = 1/2$ state which is implemented straightforwardly on a qubit. In a magnetic material, several such spins in a lattice interact via pairwise superexchange interactions J_α. The nature and

strength of these interactions, J_α, depend on several factors. These include the distance between the magnetic ions (typically J_α scales as the inverse cube of the distance between the ions), the shape of the orbitals, the symmetry of the lattice, and the local crystal fields. Magnetic frustration can arise in the lattice, for example, if spins arranged on a triangular motif in the lattice experience equal Ising anti-ferromagnetic interactions. Such a magnetic frustration can arise via a combination of straight edge bonds J_1 which are either horizontal or vertical, and the diagonal bonds J_2. This is given by the Hamiltonian

$$\mathcal{H}(\boldsymbol{s}) = J_1 \sum_{(i,j)\in \mathrm{NN}} s_i s_j + J_2 \sum_{(i,j)\in \mathrm{NNN}} s_i s_j + h \sum_{i=1}^{N} s_i, \tag{3.1}$$

where the first sum is over the nearest neighbors (NN), the second sum is over the diagonal next-nearest neighbors (NNN), and $\boldsymbol{s} = (s_1, ..., s_N)$ lists the spin orientations $s_i \in \{1, -1\}$ of the N spins. We study anti-ferromagnetic couplings with positive J_1, J_2. The term h represents a longitudinal magnetic field (parallel to the spin axis), which for the real material represents either a mean crystal field or an external magnetic field. The unit cell motif of the Hamiltonian is shown in Fig. 3.2. Materials described by this model are being actively researched in condensed matter physics. The Ising Shastry-Sutherland model is a special case of a model, inspired by the geometry of real materials, where some but not all of the diagonal bonds are present (Fig. 3.2(b)). The triangular lattice is shown in Fig. 3.2(c). In all cases we consider open boundary conditions. Analytical ground state properties of Ising models on Shastry-Sutherland and triangular lattices have been derived analytically [44, 45].

Multiple methods have been proposed to solve for ground states of Ising Hamiltonians and related optimization problems, notably Integer Programming method [46], Simulated Annealing [47] and its variants, Large Neighborhood Search [48] and Quantum or Quantum-inspired physical annealing devices. Among them, the Integer Programming method solves exactly but suffers from exponential scaling of computational time. Simulated Annealing and Large Neighborhood Search are both herustics methods that promise faster runtime but there is no guarantee of the solution qualities. Quantum annealers, digital annealers and coherent Ising machines are hardwares dedicated to solving Ising models [49, 50]. Depending

on the connectivity of these various (qu)bits, every backend could be good at a different task - parallel tempering machines could be good in finding the classical phases [26], while others could reveal intricate dynamical behaviour in a transverse field Ising universality [51]. For frustrated lattice problems, QAOA allows us to sample different ground states with certain probabilities due to quantum randomness, whereas classical and deterministic algorithms may generate a ground state efficiently, but fail to explore the states which might arise because of a coherent superposition between all the spins. Additionally, future extensions beyond the Ising limit also becomes an exciting possibility.

3.2.1 Ground state magnetization phase diagrams

We consider the nine-spin unit cells with geometries in Fig. 3.2(a-c) which represent the number of spins required to simply construct an unit cell of the Shastry-Sutherland lattice. In materials represented by Bravais lattices, these unit cells repeat periodically to realize the very large lattices in a real material. We computed ground states for each unit cell by evaluating (3.1) for each possible spin configuration to identify the lowest energy states, for varying choices of h and J_2, with $J_1 = 1$ taken as the unit of energy. We plot the magnetization

$$M = \frac{1}{N}\sum_{i=1}^{N} s_i, \tag{3.2}$$

of these ground states in the phase diagrams of Fig. 3.2(d-f). We further separate each diagram into regions A,B,... with distinct sets of ground states but sometimes equivalent magnetizations. For example, "A" and "B" in Fig. 3.2(e) have different ground states but identical magnetizations. The individual ground states are shown in the Supplemental Information (Figs. S4-S6) [52].

Starting with the non-frustrated square lattice with J_1 - only interactions with simple ferromagnetic or antiferromagnetic ground states, the degree of frustration is tuned progressively by a) addition of J_2 bonds and b) bringing $J_2 \to J_1$. The triangular lattice with uniform coupling parameters represents the maximally frustrated limit with highly degenerate solutions. The Shastry-Sutherland model represents a scenario with the minimum number of J_2

bonds required to realize a fully frustrated lattice. The solution of these states represent a problem of polynomial time complexity in two-dimensions and without a magnetic field.

The ground state for a given h shows a number of magnetization plateaus, where each plateau has a different proportion of spins pointing up. Unsurprisingly, at large h, the ground state for each lattice is ferromagnetic, in regions C, G, and E in Fig. 3.2(d-f) respectively. The situation becomes more interesting at small h in regions "A", the ground state is anti-ferromagnetic with magnetization $M = 1/9$, as five spins are aligned with the field while four are anti-aligned. For fields $8/3 \leq h \leq 4$ and small J_2, there is a ground state with $M = 7/9$ in which a single spin in the center of the unit cell is anti-aligned with the field. Besides frustration, these states are also determined by the finite size of the unit cells, where the central spin is distinguished as the only spin with four interactions in the square lattice. As J_2 and h are varied, frustration leads to a variety of different ground states for the Shastry-Sutherland and triangular lattices, with varying magnetizations in Fig. 3.2(e-f), with ground states in Supplemental Information [52]. These are true ground states of the 9-spin Hamiltonians, with boundary spins playing a big role. In the infinite size limit we expect the ground states to be progressively less dependent on the boundary, and more on the symmetry of the Hamiltonian, which we discuss in the next section.

3.2.2 Finite size effects

The finite sizes of our lattice unit cells, as well as the unusual $M = 7/9$ ground state noted in the previous section, raise questions of how the ground states for our unit cells match with ground states that would be obtained in the large size limit, and the minimum number of spins that are needed to achieve quantitative behavior consistent with large sizes. To address these questions, we computed the magnetization of triangular and Shastry-Sutherland lattices of $N = n \times n$ spins to analyze the size-dependent behavior. Due to the exponential complexity of the problem, we used *neal* [53], a software implementation of simulated annealing to approximate the ground state configurations with $h, J_2 \in [0, 6]$ and $J_1 = 1$. Each combination of h and J_2 was run 50 times and the solution with minimum Ising energy was picked. Examples with $3 \leq n \leq 30$ are shown in Fig. 3.3. We assessed convergence of

the global phase diagrams to the large size limit by computing the root mean square error (RMSE) between the target lattice's and 30×30 lattice's magnetization across points in the phase diagram. We fitted the RMSE to both a power-law as well as an exponential form (see Supplemental Information, Fig. S1 [52]), and we find that the power-law scaling with n exponent γ and prefactor a fits the RMSE better. The equation takes the form:

$$\mathrm{RMSE}(M_{n\times n}, M_{30\times 30}) = \sqrt{\frac{\sum_g (M_{n\times n,g} - M_{30\times 30,g})^2}{\mathcal{N}}} \approx a n^{\gamma}. \tag{3.3}$$

where $\mathcal{N} = 900$ is the number of points g we evaluated in each phase diagram (30 evaluations for $h \in [0, 6]$ and 30 evaluations for $J_2 \in [0, 6]$ with a step size of 0.2 in each variable). The computed RMSEs and fitted power-law curves are shown in Fig. 3.4. Empirically, the RMSE diminishes following a power law scaling with the exponent $\gamma = -1.27(4)$ for the triangular, and $\gamma = -1.34(4)$ for the Shastry-Sutherland lattice. We note that the size of the *boundary* scales as $O(n)$ while the size of the *bulk* scales as $O(n^2)$. If the RMSE had arisen strictly from the boundary effects, it would diminish following the proportion of $boundary/bulk \sim O(1/n)$. However, $\gamma < -1$ signifies a faster drop off of RMSE as compared to $1/n$, which could be because of enhanced correlations between the various spins subject to the Hamiltonian.

A more rigorous analysis of finite-size scaling [54, 55] around each critical point could yield a careful analysis of the required lattice size for target fidelity for every phase transition, our result based on an overall RMSE demonstrates that a 15×15 spin grid is already obtaining results close to the much larger 30×30 grid. Based on this trend, we expect that finite size effects in M will diminish quickly with the size of the lattice, indicating that lattices of only a few hundred spins may diminish the errors sufficiently to achieve a realistic "bulk", and therefore meaningful results for comparison with experiments which probe bulk properties, such as diffraction and heat-capacity. This suggests that quantum processors with hundreds of qubits, achievable within the noisy intermediate-scale quantum era [56], may be capable of meaningful applications for materials science applications.

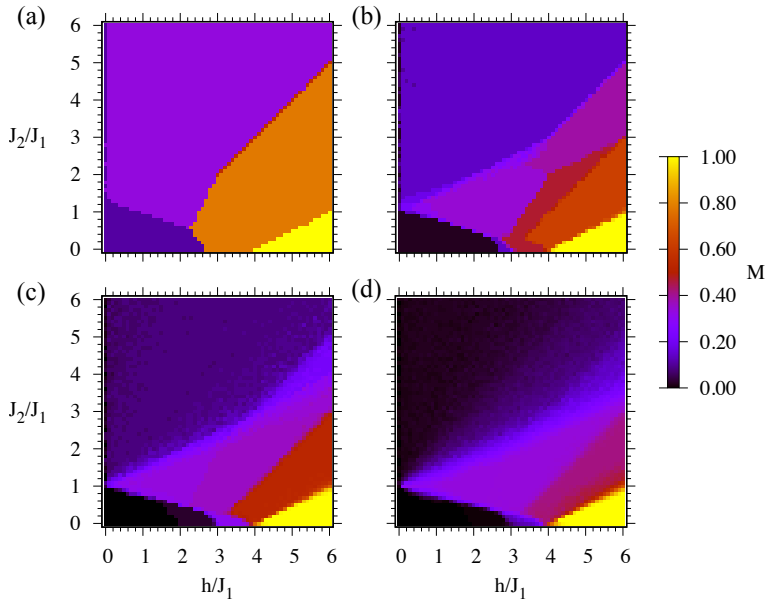

Figure 3.3. Ground state magnetization of $n \times n$ triangular spin arrays with a number of spins per dimension (a) $n = 3$, (b) $n = 7$, (c) $n = 12$, and (d) $n = 30$, computed as described in Sec. 3.2.2.

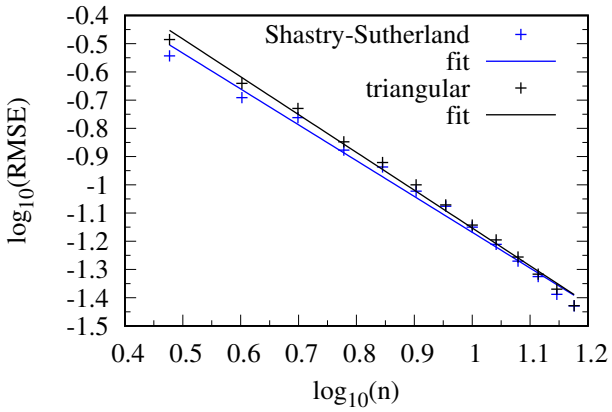

Figure 3.4. Root mean square errors (3.3) of total magnetization between $n \times n$ lattices relative to a 30×30 lattice, plotted on a log-log scale. Solid lines show fits to the power-law scaling relation (3.3); the slopes indicate the best-fit exponents $\gamma = -1.34(4)$ and $\gamma = -1.27(4)$, with fit $R^2 = 0.994$ and 0.990 for the triangular and Shastry-Sutherland lattices, respectively. Best-fit intercepts are $\gamma \log_{10}(a) = 0.19$ and $\gamma \log_{10}(a) = 0.10$ for the triangular and Shastry-Sutherland lattices respectively. The fit and the errors in the exponent are based on standard Levenberg-Marquardt routines and assume Poisson statistics at each point.

3.3 Quantum Approximate Optimization Algorithm

Quantum computers offer a route to overcoming issues associated with identifying ground states through conventional methods. One approach to address these problems uses the quantum approximate optimization algorithm, which was originally designed to find approximate solutions to difficult combinatorial optimization problems [21] that are often expressed in terms of Ising Hamiltonians [57]. Empirical performance of QAOA has been characterized for a variety of combinatorial problems [36, 58–61] and this has also led to generalizations [62–67] that have been applied to preparing chemical ground states [68] as well as ground state preparation for one-dimensional [38, 69] and two-dimensional [70] quantum spin models in theory and experiment [71].

To formulate our Ising problems in a structure that is suitable for QAOA, we first express the Ising Hamiltonian (3.1) in terms of a quantum Hamiltonian operator

$$H = J_1 \sum_{(i,j)\in \mathrm{NN}} Z_i Z_j + J_2 \sum_{(i,j)\in \mathrm{NNN}} Z_i Z_j + h \sum_{i=1}^{N} Z_i. \tag{3.4}$$

Here the N spins $s_i \in \{+1, -1\}$ in (3.1) are encoded into the eigenvalues of the Pauli Z operators, with $Z_i|z_i\rangle = s_i|z_i\rangle$, where $z_i \in \{0, 1\}$ and $s_i = 1 - 2z_i$. The set of all spin values is then encoded into a computational basis state $|\boldsymbol{z}\rangle = \bigotimes_{i=1}^{N} |z_i\rangle$. Each $|\boldsymbol{z}\rangle$ is an energy eigenstate of H with the energy eigenvalue of the corresponding classical spin problem,

$$H|\boldsymbol{z}\rangle = \mathcal{H}(\boldsymbol{z})|\boldsymbol{z}\rangle, \tag{3.5}$$

where $\mathcal{H}(\boldsymbol{z})$ comes from (3.1) taking $s_i = 1 - 2z_i$ for each component $|z_i\rangle$ in the total basis state $|\boldsymbol{z}\rangle$. This gives an encoding of the Ising spin problem (3.1) that is useful for QAOA, where we will sample eigenstates $|\boldsymbol{z}\rangle$ to try to identify the ground state of the Ising problem.

To find solutions, QAOA uses a quantum state prepared with p layers of unitary evolution, where each layer alternates between Hamiltonian evolution under the Ising Hamiltonian H and under a "mixing" Hamiltonian $B = \sum_i X_i$

$$|\psi_p(\boldsymbol{\gamma}, \boldsymbol{\beta})\rangle = \left(\prod_{l=1}^{p} e^{-i\beta_l B} e^{-i\gamma_l H} \right) |\psi_0\rangle \tag{3.6}$$

where the initial state $|\psi_0\rangle = 2^{-N/2} \sum_{\boldsymbol{z}} |\boldsymbol{z}\rangle$ is the ground state of $-B$ represented in the computational basis. The parameters $\boldsymbol{\gamma} = (\gamma_1, ..., \gamma_p)$ and $\boldsymbol{\beta} = (\beta_1, ..., \beta_p)$ are typically chosen to minimize the expectation value of the energy $\langle H \rangle$, though other objectives have also been studied [68, 72, 73]. The minimization is typically accomplished using a quantum-classical hybrid feedback loop, shown schematically in Fig. 3.5. For a given set of parameters $\boldsymbol{\gamma}$ and $\boldsymbol{\beta}$, a set of states $|\psi_p(\boldsymbol{\gamma}, \boldsymbol{\beta})\rangle$ is prepared and measured by a quantum computer. The measurement results are sent to a conventional (classical) computer to compute the classical objective function. If the objective function is not converged relative to previous evaluations, then the conventional computer uses an optimization routine to select new parameters $\boldsymbol{\gamma}', \boldsymbol{\beta}'$. The process is repeated until convergence to a minimal objective with optimized parameters $\boldsymbol{\gamma}^*, \boldsymbol{\beta}^*$. The final result is taken as the measurement result $|\boldsymbol{z}^*\rangle$ that gives the lowest energy $\mathcal{H}(\boldsymbol{z}^*)$. In the best case, $\boldsymbol{z}^* = \boldsymbol{z}_{\text{ground}}$ is a ground state, while more generally $\boldsymbol{z}^*$ may be a low-energy state that is an approximate solution to the problem.

An analytic proof has demonstrated that QAOA can prepare an exact ground state $|\boldsymbol{z}_{\text{ground}}\rangle$ of Ising Hamiltonians as $p \to \infty$ [21, 57]. Apart from the formal proof of convergence at large p, there has been significant interest in applying QAOA at small p, where approximations exceeding conventional lower bounds have been observed in simulations [36, 74] and predicted for large problems in certain contexts [75]. Realizing such advantages on devices with hundreds of qubits or more is an important topic of ongoing research as quantum computing technologies continue to develop.

For the materials problems we consider, we are interested in preparing the ground states of the Ising Hamiltonian. We compute exact ground states for our unit cells in Fig. 3.2 by evaluating all eigenvalues of the Hamiltonian using Eqs. (3.1) and (3.4) to identify the lowest energy state. For some phases the number of ground states is $N_{\text{ground}} > 1$ due to

degeneracies, while for other phases there is a single ground state $N_{\text{ground}} = 1$, as pictured in Supplemental Information [52]. To assess QAOA performance, we compute the average ground state probability

$$\overline{P}_{\text{ground}} = \frac{1}{N_{\text{ground}}} \sum_{\boldsymbol{z}_{\text{ground}}} P(\boldsymbol{z}_{\text{ground}}), \tag{3.7}$$

where the sum contains a single term in the case of a non-degenerate ground state or multiple terms in the degenerate case. Analytically, the probabilities are given by the Born rule $P(\boldsymbol{z}) = |\langle \boldsymbol{z}|\psi_p(\boldsymbol{\gamma}, \boldsymbol{\beta})\rangle|^2$, while for experiments on a quantum computer they are given by the frequencies of measurement results, $P(\boldsymbol{z}) = N(\boldsymbol{z})/N_{\text{tot}}$, where $N(\boldsymbol{z})$ is the number of times $|\boldsymbol{z}\rangle$ was measured and N_{tot} is the total number of measurements. If QAOA identifies a ground state then $|z^*\rangle = |z_{\text{ground}}\rangle$ and $\overline{P}_{\text{ground}} > 0$, while if QAOA only finds sub-optimal solutions then $\overline{P}_{\text{ground}} = 0$.

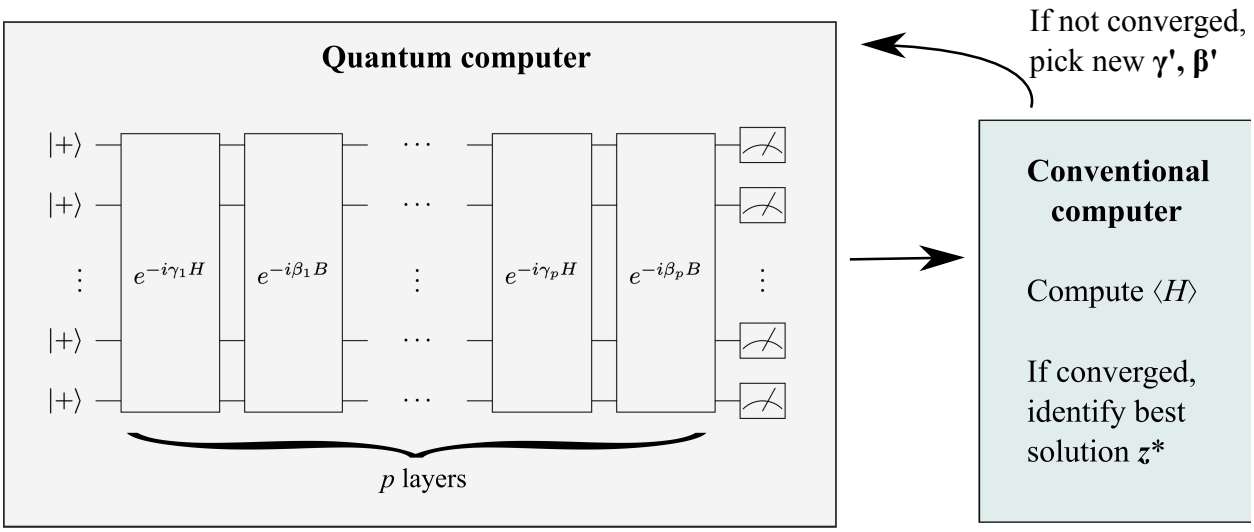

Figure 3.5. Quantum-classical optimization loop for QAOA. For a given set of parameters $\boldsymbol{\gamma}, \boldsymbol{\beta}$, a quantum computer generates and measures states $|\psi_p(\boldsymbol{\gamma}, \boldsymbol{\beta})\rangle$. The measurements are sent to a conventional computer to compute $\langle H\rangle$ and check its convergence. If $\langle H\rangle$ is not converged, then an optimization routine selects new $\boldsymbol{\gamma}'$ and $\boldsymbol{\beta}'$ for the quantum computer. If $\langle H\rangle$ is converged, then the algorithm terminates and the final solution is the measured result $\boldsymbol{z}^*$ that minimizes the energy.

Ground state preparation is a goal specific to the materials problem context we are interested in here. This is, importantly, a departure from the standard goal of QAOA in the context of approximate combinatorial optimization, where the goal is to find approximate solutions that are not necessarily the ground states. While QAOA is not expected to efficiently find exact ground states for generic NP-hard optimization problems, it may still prove useful for finding ground states of specific structured problems such as materials problems on a lattice similar to those we explore here [38, 69–71].

3.3.1 Numerical simulations of ideal QAOA

We use numerical calculations to assess the theoretical performance of QAOA for ground state preparation. These demonstrate the ideal performance of QAOA in exact pure state calculations that use matrix multiplication to evaluate (3.6). This gives an ideal baseline for later comparison against results from a noisy quantum computer, where errors lead to mixed states with degraded performance. We use $p = 1$ QAOA layers throughout this section and our results.

To identify QAOA states for our Ising problems we must determine optimized QAOA parameters γ_1^* and β_1^*. We choose regions to evaluate parameters in determining γ_1^* and β_1^* as follows. QAOA is periodic when $\beta_1 \to \beta_1 \pm \pi$ [58], hence we consider $-\pi/2 \leq \beta_1 \leq \pi/2$, which gives all unique β_1 up to symmetries. The periodicity of the γ_1 parameter is more complicated, as it depends on the Hamiltonian in $\exp(-i\gamma_1 H)$ in (3.6). Here we focus on γ_1 intervals near the origin and dependent on the magnitude of the Hamiltonian terms, which has been highly successful in previous work [76]. The basic idea is that the QAOA unitary $\exp(-i\gamma_1 H)$ changes at varying speeds with respect to γ_1, depending on the Hamiltonian coefficients J_1, h, and J_2. When the Hamiltonian coefficients increase, then γ_1 should decrease to obtain a similar unitary. The rate at which the unitary changes with respect to γ_1 is related to the average magnitude of the Hamiltonian coefficients

$$\iota = \frac{Nh + J_1 E_{\mathrm{NN}} + J_2 E_{\mathrm{NNN}}}{N + E_{\mathrm{NN}} + E_{\mathrm{NNN}}}, \tag{3.8}$$

where E_{NN} is the number of nearest-neighbor interactions and E_{NNN} is the number of next-nearest-neighbor interactions. Previous work on generic Ising Hamiltonians with $h = 0$ has shown that high quality solutions are obtained at small γ_1 with an empirical scaling of optimized parameters similar to $\gamma_1^* \sim 1/\iota$. The scaling $1/\iota$ compensates for the varying rates of evolution that are present for varying choices of the Hamiltonian, and also limits the interval of γ_1 values that are explored, simplifying the optimization [76]. Based on these ideas we choose γ_1 in the interval $-0.55 \times \pi/\iota \leq \gamma_1 \leq 0.55 \times \pi/\iota$.

We show an example of how the energy expectation value and average ground state probability depend on the choice of parameters in Fig. 3.6 for an example with the Shastry-Sutherland unit cell with Hamiltonian coefficients $J_1 = 1, J_2 = 3.7$, and $h = 1.4$ (similar patterns are observed in sample calculations using other choices of Hamiltonian coefficients and also for the triangular unit cell). There are two regions in Fig. 3.6(a) with optimized $\langle H \rangle$ in yellow. The ground state probabilities in Fig. 3.6(b) are also relatively large near the γ_1^* and β_1^* that optimize $\langle H \rangle$.

We have found in searches over much larger γ_1 intervals that the local optima for $\overline{P}_{\mathrm{ground}}$ and $\langle H \rangle$ do not always approximately align as in Fig. 3.6, which can lead to poor $\overline{P}_{\mathrm{ground}}$ at optimized $\langle H \rangle$ in these larger intervals. However, this does not appear to be a prevalent issue for the smaller ι-dependent γ_1 intervals in cases we have looked at. The results are somewhat sensitive to the specific choice of γ_1 interval, however, our choice of $-0.55 \times \pi/\iota \leq \gamma_1 \leq 0.55 \times \pi/\iota$ gives satisfactory results across the varying lattices.

To identify optimized parameters, we perform a grid search over γ_1 and β_1 for each Hamiltonian considered. We evaluate the QAOA states in (3.6) on 201 evenly spaced intervals with $-\pi/2 \leq \beta_1 \leq \pi/2$ and over 300 evenly spaced intervals with $-0.55 \times \pi/\iota \leq \gamma_1 \leq 0.55 \times \pi/\iota$ for a total of $201 \times 300 = 60,300$ grid evaluations for each Hamiltonian. This approach gives optimal parameters in our intervals up to coarse graining in the grid search. We select parameters γ_1^* and β_1^* that optimize $\langle H \rangle$.

The optimized parameters γ_1^* and β_1^* do not necessarily give the optimal ground state probabilities that are possible from QAOA. The reason is that the average energy optimization accounts for energies and probabilities of all states, which together may yield low energies at parameter choices that are not optimal for the ground states alone [36]. To assess

performance, we further compare our parameter choices against parameters $\gamma_1^{*\prime}$ and $\beta_1^{*\prime}$ that directly optimize $\overline{P}_{\text{ground}}$. The direct optimization of $\overline{P}_{\text{ground}}$ is used here for benchmarking purposes and is not a realistic approach for large problems where the ground states are unknown. For our small problems, the comparison gives an idea of how the ground state probabilities from a standard optimization of $\langle H \rangle$ compare against the best ground state probabilities that could be obtained by QAOA in our setup.

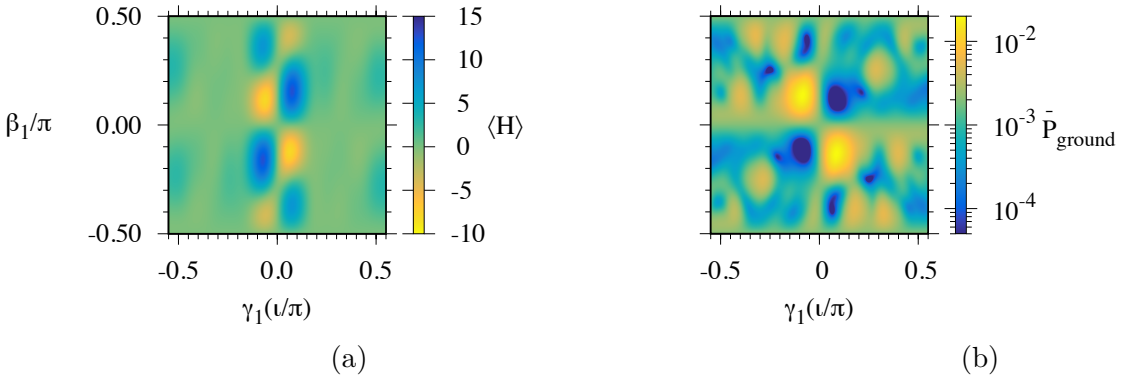

Figure 3.6. Numerical simulations of the (a) average energy $\langle H \rangle$ and (b) average ground state probability $\overline{P}_{\text{ground}}$ with varying choices of QAOA parameters γ_1 and β_1, for the Shastry-Sutherland unit cell with $J_1 = 1, J_2 = 3.7$, and $h = 1.4$ (Sec. 3.3.1). Each plot has the same range of β_1 and γ_1; the color scales are reversed in (a) and (b) so that small $\langle H \rangle$ and large $\overline{P}_{\text{ground}}$ are each represented by bright colors.

3.3.2 Quantum computations of QAOA

We next investigate the performance of QAOA using the Quantinuum H1-2 quantum computer. H1-2 contains trapped-ion qubits and uses lasers to implement gates on these qubits. Typical error rates are reported as 3.5×10^{-3} for two-qubit gates and 1×10^{-4} for single-qubit rotation gates [77]. In addition to the device H1-2, we also us the H1-1E device "emulator" to simulate noisy device behavior. This gives results that approximately correspond to expected device behavior while avoiding the financial expense and wait times that are associated with running the device. The emulator models a variety of device-specific noise processes for the H1-class computers, including depolarizing noise, leakage errors, crosstalk, dephasing in transport, and qubit idling errors [78].

We test QAOA on the H1-2 using the QCOR software stack [79]. The QCOR stack translates the series of unitary operators expressing QAOA into quantum circuits for H1-2; see Supplemental Information [52], Appendix B, for details. The QCOR program used for submitting jobs to the device as well as our calculations are available online, cf. "Data Accessibility".

Furthermore, modern quantum computers are known to be affected by state preparation and measurement (SPAM) errors as well as gate infidelities from a variety of physical sources. We assessed SPAM errors expected in our quantum computations using the device emulator, with details in Supplemental Information Appendix C [52]. The probability to observe no error in circuits we tested was approximately 96%, with errors distributed approximately uniformly across qubits. We account for these errors using an independent bit-flip model and associated SPAM matrix $\tilde{P}$, which transforms an ideal set of measurement results to the expected noisy set of results. The inverse matrix $\tilde{P}^{-1}$ can then be applied to our noisy measurements from the quantum computer to approximately correct for SPAM errors. A technical issue arises in that the mitigated measurement probabilities can sometimes be negative, due to the approximate nature of the mitigation scheme. This leads to a second mitigation scheme that additionally sets all negative probabilities to zero and renormalizes so the total probability is one. We use each of these approaches to attempt to correct the small SPAM errors we expect from the quantum computer, as described in detail in Supplemental Information [52].

3.4 Results

In this section we consider the results from QAOA applied to the materials lattices of Fig. 3.2. We take $J_1 = 1$ as the unit of energy and analyze the success of QAOA in preparing ground states at variable h and J_2, first in numerical simulations (Sec. 3.3.1) and then in quantum computations on a trapped-ion quantum computer (Sec. 3.3.2).

3.4.1 Ground state measurement probabilities

We first consider theoretical probabilities to measure the ground state with QAOA and how these vary for different parameter choices in the Hamiltonian. We begin with the simple square lattice in Fig. 3.2(a,d), which does not exhibit frustration as there are no triangles in the interaction graph. The probability to measure the ground state for varying h is shown in Fig. 3.7. Fig. 3.7(a) shows the probabilities obtained from optimizing the standard objective $\langle H \rangle$ while Fig. 3.7(b) shows the best-case results based on optimizing $\overline{P}_{\text{ground}}$, as described in Sec. 3.3.1. The probabilities in each case are similar, demonstrating that optimizing $\langle H \rangle$ is nearly as successful in increasing the ground state probability as a direct optimization.

The average ground state probability shows distinct behaviors for each of the three ground states at varying h, visually separated by dotted lines. In the anti-ferromagnetic ground state at small h, the probability $\overline{P}_{\text{ground}}$ approximately oscillates between $h = 0$ and $h = 2$, with small probabilities observed near integer values of h and larger probabilities near $h = 1/2$ and $h = 3/2$. The $M = 7/9$ ground state with $8/3 < h < 4$ has a near-constant probability of ≈ 0.06. At $h = 4$ the ground state becomes ferromagnetic and $\overline{P}_{\text{ground}}$ increases significantly, with monotonic increases at larger h.

We rationalize the varying success probabilities in the figure as attributable to structures of the ground states at varying h and the interplay with the structure of the QAOA state in (3.6). We show in Supplemental Information [52] Appendix D that QAOA can exactly prepare the ferromagnetic ground state when $h \gg J_1$ for arbitrary lattice sizes, based on the fact that $\exp(-i\gamma H) \approx \exp\left(-i\gamma h \sum_{i=1}^{N} Z_i\right)$ in this limit. This is consistent with the behavior in the figure, where $\overline{P}_{\text{ground}}$ increases monotonically with h for the ferromagnetic ground state at $h \geq 4$. We further show in Supplemental Information [52] Appendix E how the anti-ferromagnetic ground state probability is maximized at $h = 0.5$, and we devise large γ_1 parameters that can further improve these results (We did not include larger γ_1 parameters in our numerical searches as this can lead to poor $\overline{P}_{\text{ground}}$ at parameters that optimize $\langle H \rangle$ for the frustrated lattices, as remarked in Sec. 3.3.1). However, the mechanism for anti-ferromagnetic ground state preparation here depends on the specific choice of the 3×3 lattice, and it is not clear how QAOA will behave for other lattice sizes. For the

M=7/9 phase the QAOA state is more complicated, as it is a superposition of many basis states that depends on the optimized parameters, and we do not have an analytic account for this behavior. The optimized parameters that create each QAOA state in the square-lattice phase diagram are shown in Supplemental Information Appendix F [52].

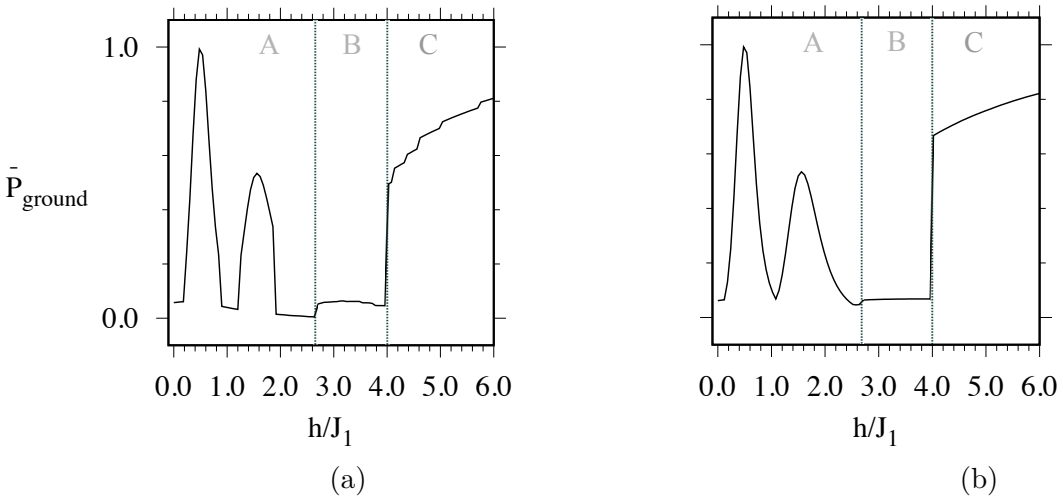

Figure 3.7. The square unit cell ground state probabilities when (a) optimizing $\langle H \rangle$ and (b) optimizing $\overline{P}_{\text{ground}}$ as described in Sec. 3.3.1. The $\overline{P}_{\text{ground}}$ ranges are identical in each figure. Phases A, B, C refer the anti-ferromagnetic, M=7/9, and ferromagnetic phases of Fig. 3.2 respectively, with vertical dotted lines showing the phase boundaries.

Ground state probabilities $\overline{P}_{\text{ground}}$ for the Shastry-Sutherland and triangular lattices are pictured in Figs. 3.8 and 3.9, respectively. Ground state probabilities from optimizing $\langle H \rangle$ are presented in panels (a) while panels (b) show the best case probabilities from a direct optimization of $\overline{P}_{\text{ground}}$ as described in Sec. 3.3.1. These probabilities show patterned behavior, with distinct probabilities $\overline{P}_{\text{ground}}$ observed throughout most of each individual region A,B,..., with significant differences in $\overline{P}_{\text{ground}}$ between different regions. At small J_2, there are oscillations in the probability for preparing the anti-ferromagnetic ground states at small h, and large success probabilities for the ferromagnetic ground state at large h, as foreshadowed by results from the square lattice. On the other hand, as the J_2 coupling increases, the triangular and Shastry-Sutherland lattices experience increased frustration, with competing interactions within the triangular motifs in Fig. 3.2. The average ground state probability decreases significantly as J_2 increases and frustration becomes dominant.

This is especially evident when $J_2 \gtrsim h$, for example in the top left of each of Figs. 3.8(b) and 3.9(b). The $\overline{P}_{\text{ground}}$ are mostly uniform across h and J_2 within each region, qualitatively similar to the nearly-uniform probability for the $M = 7/9$ state at varying h for the square lattice in Fig. 3.7. Ground state probabilities are typically $\gtrsim 0.01$, indicating that only $\lesssim 100$ measurements are expected to identify a ground state. We now turn to computations on a trapped-ion quantum computer, to benchmark and assess performance of QAOA on a real quantum computing device.

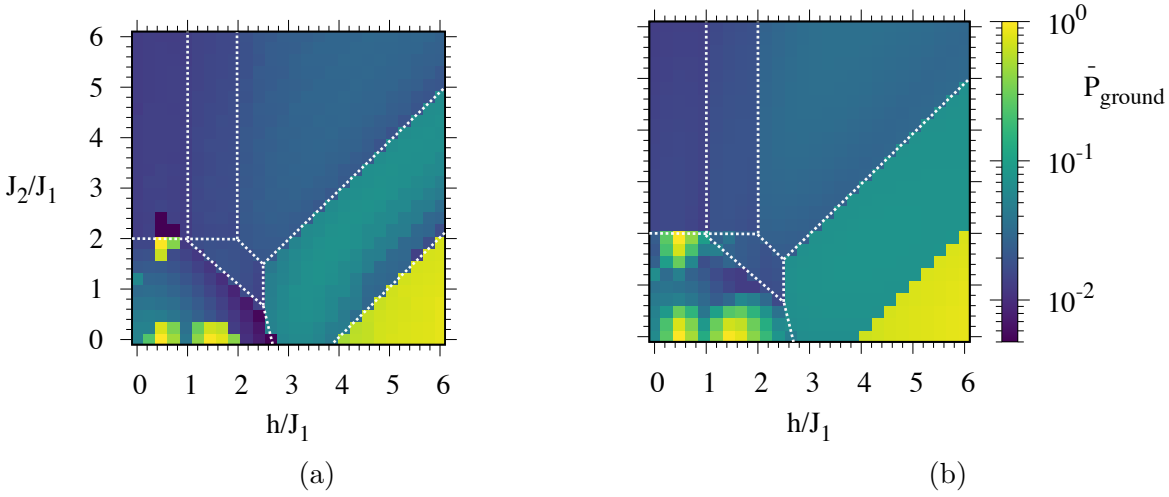

Figure 3.8. Shastry-Sutherland unit cell ground state probabilities when (a) optimizing $\langle H \rangle$ and (b) optimizing $\overline{P}_{\text{ground}}$ as described in Sec. 3.3.1. The ranges for J_2/J_1 and $\overline{P}_{\text{ground}}$ are identical in each figure.

3.4.2 QAOA quantum computations

Here we assess QAOA performance in preparing ground states on a trapped-ion quantum computer. Ultimately, our aim is to validate the idea that a current quantum computing technology is capable of preparing each ground state of a frustrated Ising Hamiltonian using QAOA. An important first step is to assess whether optimized parameters from our theoretical calculations are also optimized for the device, or whether further optimization is needed to determine device-specific optimized parameters.

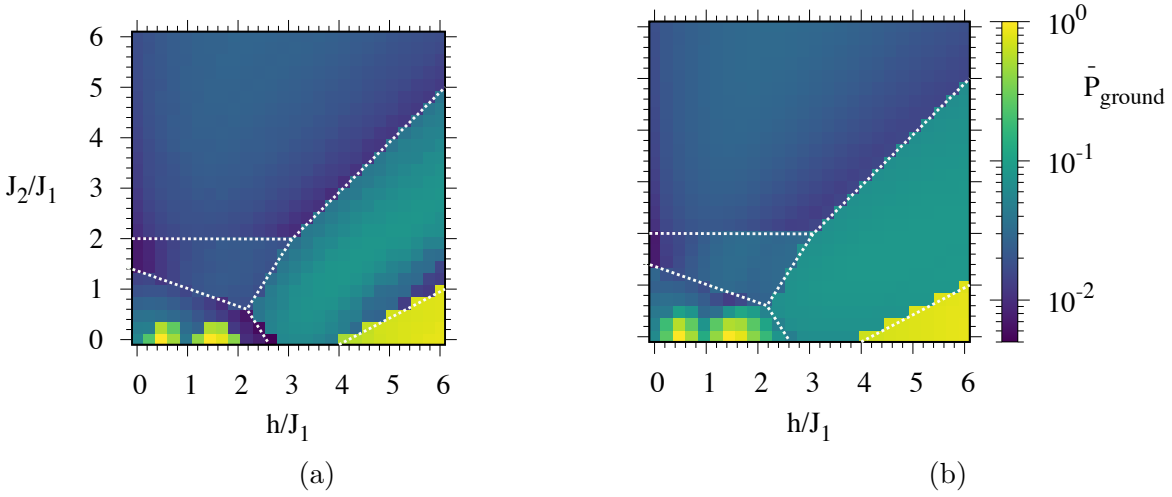

Figure 3.9. Triangular unit cell ground state probabilities when (a) optimizing $\langle H \rangle$ and (b) optimizing $\overline{P}_{\text{ground}}$ as described in Sec. 3.3.1. The ranges for J_2/J_1 and $\overline{P}_{\text{ground}}$ are identical in each figure.

Quantum computational performance with varying parameters

QAOA depends on the choice of parameters, as discussed in connection with Fig. 3.6. To test whether our theoretical parameters also yield good performance in the device, we consider QAOA circuits evaluating a point in region E of the Shastry-Sutherland phase diagram Fig. 3.2(e), with Hamiltonian coefficients and QAOA parameters shown in Table 3.1. The parameters correspond to a local minimum in $\langle H \rangle$, similar to the minima observed in Fig. 3.6. We use the H1-1E device emulator to evaluate circuits at the optimized γ_1 and β_1 and circuits where either γ_1 or β_1 has been displaced from its optimal value, as shown in Fig. 3.10. Black crosses in the figure indicate how $\langle H \rangle$ increases in pure state simulations as either of these parameters are varied individually. Error bars denote the analytic standard error of the mean (S.E.M.) for $N_{\text{shots}} = 1000$ measurement shots, with S.E.M.$= \sqrt{(\langle H^2 \rangle - \langle H \rangle^2)/N_{\text{shots}}}$ calculated numerically from the pure states. If the quantum computations did not have any noise, then from the central limit theorem we would expect about two-thirds of the $\langle H \rangle$ from the quantum computer to be within these error bars.

The theoretical $\langle H \rangle$ can be compared against the device emulator, with data point labels in the figure beginning with "H1-1E". There are three sets of data points for the emulator; the

first is direct output labeled "H1-1E", the second includes SPAM error mitigation (Sec. 3.3.2) in "H1-1E, E.M.", the third includes a variation of the SPAM mitigation that additionally forces the mitigated probabilities to be $P \geq 0$ in "H1-1E, E.M., P≥0". These emulated $\langle H \rangle$ are larger than the theoretical values and we attribute this to noise in the device emulator, which introduces errors that cause the energy to deviate from its ideal minimum value. Despite these errors, the shape of the landscape is similar to our theoretical calculations, with best performance observed near the theoretical parameters that minimize $\langle H \rangle$, and energies that tend to increase away from these parameters.

Table 3.1. The parameters used for quantum computations with the Shastry-Sutherland lattice. Here J_2/J_1 and h/J_1 are the Hamiltonian coefficients used in the calculations, γ and β are the QAOA parameters, and N_{shots} is the number of measurement shots taken on the quantum computer.

region	degeneracy	M	J_2/J_1	h/J_1	β_1/π	γ_1/π	N_{shots}
A	1	1/9	0.240	1.440	0.750	-0.507	400
B	4	1/9	3.840	0.480	0.112	-0.048	1000
C	4	3/9	3.840	1.680	0.121	-0.043	1000
D	2	3/9	1.680	1.920	0.131	-0.056	400
E	4	5/9	2.000	2.480	0.143	-0.050	1000
F	1	7/9	1.680	3.600	0.182	-0.046	400
G	1	1.0	0.240	5.520	0.244	-0.041	400

We further validate that the H1-2 trapped-ion device itself is consistent with the emulator in the data points that begin with "H1-2". These actually yield better energies than the emulator, and are within one standard error of the mean from our theoretical results. The results from the device and emulator indicate that the energy landscape as a function of the QAOA parameters γ_1 and β_1 is consistent between our theoretical calculations, the quantum device, and emulator. We therefore proceed with our theoretically optimized parameters to evaluate success in ground state preparation using the quantum computer.

Quantum calculations of ground states

We now perform calculations on the Honeywell H1-2 quantum computer to analyze success probability in ground state preparation. We consider points in each region of the Shastry-

Sutherland lattice, using parameters listed in Table 3.1 that correspond to local minima in $\langle H \rangle$, similar to the minima used to evaluate theoretical performance in Sec. 3.4.1). We post-process the measurement results using the SPAM mitigation model with probabilities $P(\boldsymbol{z}) \geq 0$ (see Sec. 3.3.2), to give a minor correction to the observed results that is designed to counteract this known source of error.

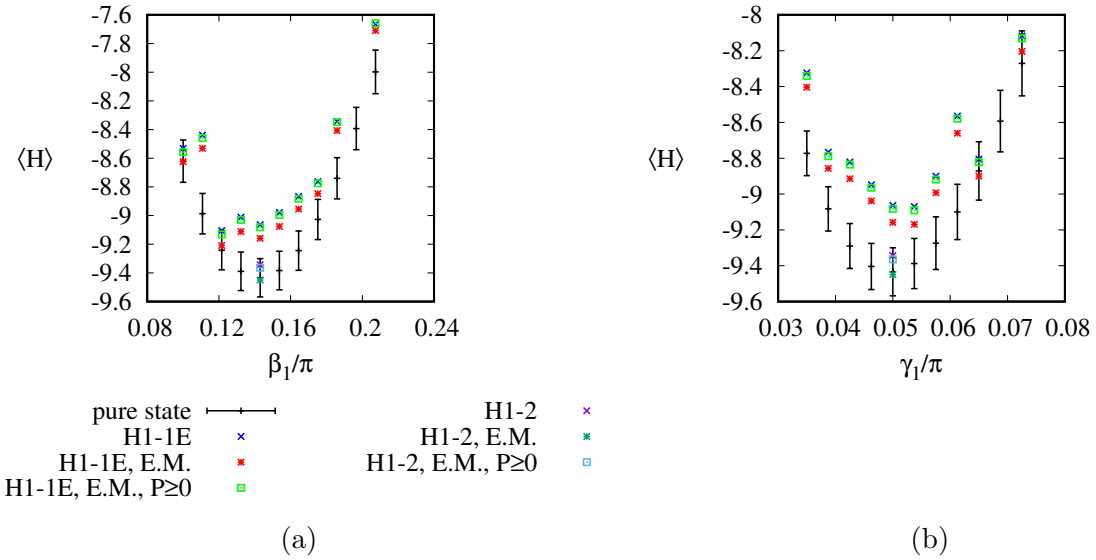

Figure 3.10. Angle sensitivity analysis for $h = 2.48$ and $J_2 = 2.0$, with separate variations in (a) β_1 and (b) γ_1 about the ideal values from Table 3.1. Black crosses show results from pure state calculations, with error bars denoting the standard error of the mean at 1000 shots (see text). Data points showing results from the Honeywell emulator are denoted with "E" in H1-1E and results from the trapped-ion quantum computer are labeled H1-2. Data points labeled 'H1-1E' and 'H1-2' are raw data, labels "E.M." (error-mitigation) are with basic mitigation, and "E.M. P≥0" are readout error mitigation that forces each probability $P(\boldsymbol{z})$ to be ≥ 0, as described in Sec. 3.3.2.

Figure 3.11 shows the ground state probabilities from quantum computations in comparison with ideal expectations from pure states. The ground states are separated by regions A,B,... with markers a,b,... corresponding to the individual ground states pictured in electronic supplementary material Fig. S16. The quantum computations succeed in observing each individual ground state in each region of the Shastry-Sutherland lattice, as seen by the positive probabilities in each state "a", "b",...

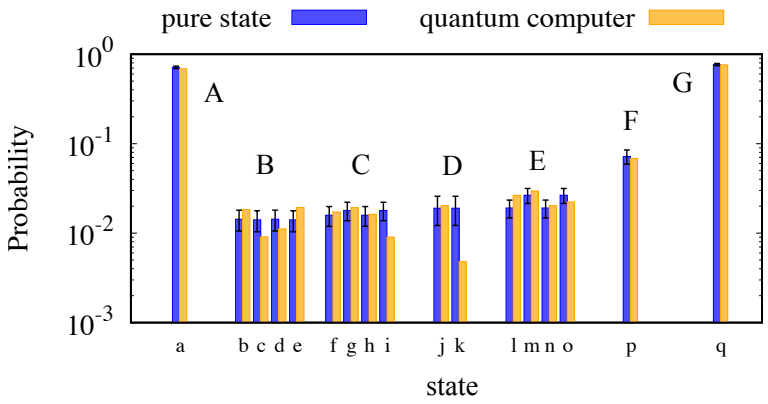

Figure 3.11. Probabilities to observe each ground state from pure state simulations compared with observed frequencies estimated by quantum computations with the H1-2 device for each different phase (A-G) of the Shastry-Sutherland unit cell. Alphabetical labels "a", "b", etc., identify the different ground states in electronic supplementary material Fig. S16.

For a closer comparison of probabilities, we plot error bars denoting the theoretical standard error of the mean S.E.M.=$\sqrt{P(\boldsymbol{z})(1-P(\boldsymbol{z}))/N_{\text{shots}}}$. The S.E.M. defines a range in which we expect about two-thirds of estimated $P_{\text{est}}(\boldsymbol{z}) = N(\boldsymbol{z})/N_{\text{shots}}$ are expected to be found, where $N(\boldsymbol{z})$ is the number of measurement results of a given ground state and N_{shots} is the total number of measurements in Table 3.1. The probabilities from the quantum computation are largely consistent with the pure state results, with the majority of results within one S.E.M. from the ideal $P(\boldsymbol{z})$, as expected in finite sampling to estimate the ground state probability. There are only two large deviations for states "k" and "i", which may be related to noise in the device. The quantum computations succeed in preparing ground states with probabilities comparable to pure-state expectations.

3.5 Conclusion

We analyzed QAOA as an approach for preparing materials ground states on three types of Ising Hamiltonians with longitudinal magnetic fields, focusing on nine-spin unit cells as a starting size that is amenable to simulations and calculations on a trapped-ion quantum computer.

We applied QAOA to the nine-spin Ising unit cell problems to assess its success in ground state preparation. We found that the theoretical success probability depends significantly on the structure of the ground state, while it is mostly insensitive to the precise Hamiltonian parameters, which can vary within regions consistent with a fixed ground state. Each Hamiltonian yields a ferromagnetic ground state in the presence of large magnetic fields, and QAOA achieved large success probabilities for these relatively simple states. The probabilities for other types of ground states were more variable, and tended to decrease as next-nearest-neighbor couplings became stronger with associated frustration in the lattice. For all of these nine-spin states, we typically find success probabilities indicating that $\lesssim$ 100 measurements are expected to be necessary from an ideal quantum computer for these problem instances.

To assess QAOA performance under realistic conditions we implemented the algorithm on a trapped-ion quantum computer. These quantum computations succeeded in observing each of the 17 ground states of the Shastry-Sutherland unit cell. The quantum computations yielded ground state probabilities that were consistent with theoretical expectations based on pure states, indicating that noise was not a significant issue at the sizes and depths tested. This suggests that calculations with current technology can likely be extended to greater QAOA depth parameters p, and to larger sizes as greater numbers of qubits become available. At greater depths and sizes we expect higher performance and more realistic results in comparison with the large size limit, respectively.

While the ground states and associated phase diagrams for our nine-spin unit cells were found to have significant finite size effects relative to the large-size limit, the errors from finite size effects on the classically-calculated magnetization phase diagrams on $n \times n$ lattices up to $n = 30$ was found to be suppressed rapidly with n, with small errors at $n = 15$ indicating that only hundreds of spins may be necessary to reproduce large scale behavior. This provides a baseline of hundreds of qubits for quantum computational experiments that seek to explain materials science problems, which may be accessible to near-term quantum computers in coming years.

Assessing scaling of the ground state probability with size N will be an essential aspect of extending this approach to larger sizes N. This includes numerical simulations to quantify

how the ground state probabilities depend on the number of spins N and number of QAOA layers p; previous works have shown $p \propto N$ maintains a large ground state probability ($\gtrsim 0.7$) for simple models in different contexts [37, 38], but future work is needed to test scaling in the current model. Benchmarking on quantum computers is also essential to understand how real noise processes effect scalability.

Thus from our results we envision QAOA can be successfully applied to somewhat larger lattice problems as quantum computing technologies develop and larger number of qubits become available. These could be used for optimization of Ising lattice problems as we have here, with increasing sizes that potentially describe real bulk properties of materials in the $N \to \infty$ limit. Additionally, the QAOA algorithm is general, with the application of a magnetic field, and hence could be explored for lattice problems which are NP-Hard [80]. But a more promising future direction leveraging the full benefit of this approach is to extend and modify QAOA to prepare ground states of quantum Hamiltonians such as the XY and Heisenberg models, which can lead to a variety of quantum phenomena not captured in the Ising model, such as quantum spin glasses [81], spin nematicity [82], Berzinski-Kosterlitz-Thouless states [83, 84] and long-range entangled states such as Dirac string excitations [85], the likes of which exist in 2D frustrated quantum spin liquids and spin ice. Many of these topics are fiercely researched and are of considerable interest and importance for future quantum technologies and devices. Conventional numerical methods for understanding these states are hindered by the exponential size of the Hilbert space, making it difficult to generate a theoretical understanding of experimental observations. QAOA or related generalizations [38, 62, 68–71] offer a potential route to overcome conventional computing bottlenecks. Some successes along these lines have been observed in certain contexts, however, advances in methodology and quantum computing technologies are needed to extend these methods to complicated and larger-scale problems where quantum computational approaches may have a significant impact in understanding and developing materials for technological applications.

Bibliography

[1]S. Blundell, *Magnetism in condensed matter* (Oxford University Press, Oct. 2001).

[2]A. M. Samarakoon, A. Banerjee, S.-S. Zhang, Y. Kamiya, S. E. Nagler, D. A. Tennant, S.-H. Lee, and C. D. Batista, "Comprehensive study of the dynamics of a classical kitaev spin liquid," Phys. Rev. B **96**, 134408 (2017).

[3]S. M. Winter, Y. Li, H. O. Jeschke, and R. Valentí, "Challenges in design of kitaev materials: magnetic interactions from competing energy scales," Phys. Rev. B **93**, 214431 (2016).

[4]M. Vojta, "Frustration and quantum criticality," Reports on Progress in Physics **81**, 064501 (2018).

[5]C. Broholm, R. J. Cava, S. A. Kivelson, D. G. Nocera, M. R. Norman, and T. Senthil, "Quantum spin liquids," Science **367**, eaay0668 (2020).

[6]Q. Zhu, Z. Chen, S. Zhang, Q. Li, Y. Jiang, P. Wu, and K. Zhang, "Improving soft magnetic properties in finemet-like alloys with ga addition," Journal of Magnetism and Magnetic Materials **487**, 165297 (2019).

[7]A. Szasz, J. Motruk, M. P. Zaletel, and J. E. Moore, "Chiral spin liquid phase of the triangular lattice hubbard model: a density matrix renormalization group study," Phys. Rev. X **10**, 021042 (2020).

[8]C. Wessler, B. Roessli, K. W. Krämer, et al., "Observation of plaquette fluctuations in the spin-1/2 honeycomb lattice," npj Quantum Mater **5** (2020).

[9]E. Stoudenmire and S. R. White, "Studying two-dimensional systems with the density matrix renormalization group," Annual Review of Condensed Matter Physics **3**, 111–128 (2012).

[10]S. Wessel, B. Normand, F. Mila, and A. Honecker, "Efficient Quantum Monte Carlo simulations of highly frustrated magnets: the frustrated spin-1/2 ladder," SciPost Phys. **3**, 005 (2017).

[11]Y. Kamiya, Y. Kato, J. Nasu, and Y. Motome, "Magnetic three states of matter: a quantum monte carlo study of spin liquids," Phys. Rev. B **92**, 100403 (2015).

[12]M. Troyer and U.-J. Wiese, "Computational complexity and fundamental limitations to fermionic quantum monte carlo simulations," Phys. Rev. Lett. **94**, 170201 (2005).

[13]A. M. Samarakoon, P. Laurell, C. Balz, A. Banerjee, P. Lampen-Kelley, D. Mandrus, S. E. Nagler, S. Okamoto, and D. A. Tennant, "Extraction of interaction parameters for $\alpha-RuCl_3$ from neutron data using machine learning," Phys. Rev. Res. **4**, L022061 (2022).

[14]Z. Zhu, P. A. Maksimov, S. R. White, and A. L. Chernyshev, "Disorder-induced mimicry of a spin liquid in $YbMgGaO_4$," Phys. Rev. Lett. **119**, 157201 (2017).

[15]E. Altman, K. R. Brown, G. Carleo, L. D. Carr, et al., "Quantum simulators: architectures and opportunities," PRX Quantum **2**, 017003 (2021).

[16]I. M. Georgescu, S. Ashhab, and F. Nori, "Quantum simulation," Rev. Mod. Phys. **86**, 153–185 (2014).

[17]A. D. King, C. Nisoli, E. D. Dahl, G. Poulin-Lamarre, and A. Lopez-Bezanilla, "Qubit spin ice," Science **373**, 576–580 (2021).

[18]R. Harris, Y. Sato, A. J. Berkley, M. Reis, et al., "Phase transitions in a programmable quantum spin glass simulator," Science **361**, 162–165 (2018).

[19]D. Bluvstein, H. Levine, G. Semeghini, et al., "A quantum processor based on coherent transport of entangled atom arrays," Nature **604**, 451–456 (2022).

[20]K. J. Satzinger, Y.-J. Liu, A. Smith, C. Knapp, et al., "Realizing topologically ordered states on a quantum processor," Science **374**, 1237–1241 (2021).

[21]E. Farhi, J. Goldstone, and S. Gutmann, "A quantum approximate optimization algorithm," arXiv **1411.4028** (2014).

[22]A. Ortiz-Ambriz, C. Nisoli, C. Reichhardt, C. J. O. Reichhardt, and P. Tierno, "Colloquium: ice rule and emergent frustration in particle ice and beyond," Rev. Mod. Phys. **91**, 041003 (2019).

[23]Y. I. Dublenych, "Ground states of the ising model on the shastry-sutherland lattice and the origin of the fractional magnetization plateaus in rare-earth-metal tetraborides," Phys. Rev. Lett. **109**, 167202 (2012).

[24]W. C. Huang, L. Huo, G. Tian, H. R. Qian, X. S. Gao, M. H. Qin, and J.-M. Liu, "Multi-step magnetization of the Ising model on a Shastry-Sutherland lattice: a Monte Carlo simulation," Journal of Physics: Condensed Matter **24**, 10.1088/0953-8984/24/38/386003 (2012).

[25]P. Kairys, A. D. King, I. Ozfidan, K. Boothby, J. Raymond, A. Banerjee, and T. S. Humble, "Simulating the shastry-sutherland ising model using quantum annealing," PRX Quantum **1**, 020320 (2020).

[26]A. Jha, E. Stoyanoff, G. Khundzakishvili, P. Kairys, H. Ushijima-Mwesigwa, and A. Banerjee, "Digital annealing route to complex magnetic phase discovery," in (2021).

[27]P. Farkašovský, H. Čenčariková, and S. Mat'aš, "Numerical study of magnetization processes in rare-earth tetraborides," Phys. Rev. B **82**, 054409 (2010).

[28]J. Trinh, S. Mitra, C. Panagopoulos, T. Kong, P. C. Canfield, and A. P. Ramirez, "Degeneracy of the 1/8 plateau and antiferromagnetic phases in the shastry-sutherland magnet TmB_4," Phys. Rev. Lett. **121**, 167203 (2018).

[29]K. Siemensmeyer, E. Wulf, H.-J. Mikeska, K. Flachbart, S. Gabáni, S. Mat'aš, P. Priputen, A. Efdokimova, and N. Shitsevalova, "Fractional magnetization plateaus and magnetic order in the shastry-sutherland magnet TmB_4," Phys. Rev. Lett. **101**, 177201 (2008).

[30]L. Ye, T. Suzuki, and J. G. Checkelsky, "Electronic transport on the shastry-sutherland lattice in ising-type rare-earth tetraborides," Phys. Rev. B **95**, 174405 (2017).

[31]A. S. Panfilov, G. E. Grechnev, I. P. Zhuravleva, A. V. Fedorchenko, and V. B. Muratov, "Specific features of the magnetic properties of rb4 (r = ce, sm and yb) tetraborides. effects of pressure," Low Temperature Physics **41**, 193–198 (2015).

[32]J. Y. Kim, N. H. Sung, B. Y. Kang, M. S. Kim, B. K. Cho, and J.-S. Rhyee, "Magnetic anisotropy and magnon gap state of smb4 single crystal," Journal of Applied Physics **107**, 09E111 (2010).

[33]S. Yoshii, K. Ohoyama, K. Kurosawa, H. Nojiri, M. Matsuda, P. Frings, F. Duc, B. Vignolle, G. L. J. A. Rikken, L.-P. Regnault, S. Michimura, and F. Iga, "Neutron diffraction study on the multiple magnetization plateaus in TbB_4 under pulsed high magnetic field," Phys. Rev. Lett. **103**, 077203 (2009).

[34]Y. Shokef, A. Souslov, and T. C. Lubensky, "Order by disorder in the antiferromagnetic ising model on an elastic triangular lattice," Proceedings of the National Academy of Sciences **108**, 11804–11809 (2011).

[35]Y. I. Dublenych, "Ground states of the Ising model on an anisotropic triangular lattice: stripes and zigzags," Journal of Physics: Condensed Matter **25**, 406003 (2013).

[36]P. C. Lotshaw, T. S. Humble, R. Herrman, J. Ostrowski, and G. Siopsis, "Empirical performance bounds for quantum approximate optimization," Quantum Inf Process **20**, 10.1007/s11128-021-03342-3 (2021).

[37]V. Akshay, H. Philathong, E. Campos, D. Rabinovich, I. Zacharov, X.-M. Zhang, and J. D. Biamonte, "Circuit depth scaling for quantum approximate optimization," Phys. Rev. A **106**, 042438 (2022).

[38]W. W. Ho and T. H. Hsieh, "Efficient variational simulation of non-trivial quantum states," SciPost Phys. **6**, 029 (2019).

[39]S. Wang, E. Fontana, M. Merezo, K. Sharma, A. Sone, L. Cincio, and P. J. Coles, "Noise-induced barren plateaus in variational quantum algorithms," Nat Commun **12**, 6961 (2021).

[40]J. Weidenfeller, L. C. Valor, J. Gacon, C. Tornow, L. Bello, S. Woerner, and D. J. Egger, "Scaling of the quantum approximate optimization algorithm on superconducting qubit based hardware," Quantum **6**, 870 (2022).

[41]G. González-García, R. Trivedi, and J. I. Cirac, "Error propagation in nisq devices for solving classical optimization problems," PRX Quantum **3**, 040326 (2022).

[42]D. S. França and R. García-Patrón, "Limitations of optimization algorithms on noisy quantum devices," Nat. Phys. **17**, 1221–1227 (2021).

[43]P. C. Lotshaw, T. Nguyen, A. Santana, M. McCaskey, R. Herrman, J. Ostrowski, G. Siopsis, and T. S. Humble, "Scaling quantum approximate optimization on near-term hardware," Sci Rep **12**, 12388 (2022).

[44]B. Sriram Shastry and B. Sutherland, "Exact ground state of a quantum mechanical antiferromagnet," Physica B+C **108**, 1069–1070 (1981).

[45]U. Brandt and J. Stolze, "Ground states of the triangular Ising model with two-and three-spin interactions," Z. Physik B - Condensed Matter **64**, 481–490 (1986).

[46]A. Billionnet and S. Elloumi, "Using a mixed integer quadratic programming solver for the unconstrained quadratic 0-1 problem," Math. Program. **109**, 55–68 (2007).

[47]S. Kirkpatrick, C. D. Gelatt, and M. P. Vecchi, "Optimization by simulated annealing," Science **220**, 671–680 (1983).

[48]A. Selby, "Efficient subgraph-based sampling of Ising-type models with frustration," arXiv **1409.3934** (2014).

[49]A. D. King, J. Carrasquilla, J. Raymond, I. Ozfidan, et al., "Observation of topological phenomena in a programmable lattice of 1,800 qubits," Nature **560**, 456–460 (2018).

[50]G. Semeghini, H. Levine, A. Keesling, S. Ebadi, et al., "Probing topological spin liquids on a programmable quantum simulator," Science **374**, 1242–1247 (2021).

[51]Y. Bando, Y. Susa, H. Oshiyama, N. Shibata, et al., "Probing the universality of topological defect formation in a quantum annealer: kibble-zurek mechanism and beyond," Phys. Rev. Res. **2**, 033369 (2020).

[52]https://doi.org/10.6084/m9.figshare.c.6260131.

[53]*D-wave systems*, https://github.com/dwavesystems/dwave-neal.

[54]N. Goldenfeld, *Lectures on phase transitions and the renormalization group*, Frontiers in Physics (Addison-Wesley Publishing Company, 1992).

[55]B. Khalid, S. H. Sureshbabu, A. Banerjee, and S. Kais, "Finite-size scaling on a digital quantum simulator using quantum restricted boltzmann machine," Frontiers in Physics **Volume 10 - 2022**, 10.3389/fphy.2022.915863 (2022).

[56]J. Preskill, "Quantum Computing in the NISQ era and beyond," Quantum **2**, 79 (2018).

[57]A. Lucas, "Ising formulations of many np problems," Frontiers in Physics **Volume 2 - 2014**, 10.3389/fphy.2014.00005 (2014).

[58]L. Zhou, S.-T. Wang, S. Choi, H. Pichler, and M. D. Lukin, "Quantum approximate optimization algorithm: performance, mechanism, and implementation on near-term devices," Phys. Rev. X **10**, 021067 (2020).

[59]J. Cook, S. Eidenbenz, and A. Bartschi, " The Quantum Alternating Operator Ansatz on Maximum k-Vertex Cover," in 2020 ieee international conference on quantum computing and engineering (qce) (Oct. 2020), pp. 83–92.

[60]P. Vikstål, M. Grönkvist, M. Svensson, M. Andersson, G. Johansson, and G. Ferrini, "Applying the quantum approximate optimization algorithm to the tail-assignment problem," Phys. Rev. Appl. **14**, 034009 (2020).

[61]S. Harwood, C. Gambella, D. Trenev, A. Simonetto, D. Bernal Neira, and D. Greenberg, "Formulating and solving routing problems on quantum computers," IEEE Transactions on Quantum Engineering **2**, 1–17 (2021).

[62]S. Hadfield, Z. Wang, B. O'Gorman, E. G. Rieffel, D. Venturelli, and R. Biswas, "From the quantum approximate optimization algorithm to a quantum alternating operator ansatz," Algorithms **12**, 10.3390/a12020034 (2019).

[63]T. L. Patti, J. Kossaifi, A. Anandkumar, and S. F. Yelin, "Variational quantum optimization with multibasis encodings," Phys. Rev. Res. **4**, 033142 (2022).

[64]R. Herrman, P. C. Lotshaw, J. Ostrowski, T. S. Humble, and G. Siopsis, "Multi-angle quantum approximate optimization algorithm," Sci Rep **12**, 6781 (2022).

[65]E. Farhi, J. Goldstone, S. Gutmann, and H. Neven, "Quantum algorithms for fixed qubit architectures," arXiv **1703.06199** (2017).

[66]R. Tate, M. Farhadi, C. Herold, G. Mohler, and S. Gupta, "Bridging classical and quantum with sdp initialized warm-starts for qaoa," ACM Transactions on Quantum Computing **4**, 10.1145/3549554 (2023).

[67]L. Zhu, H. L. Tang, G. S. Barron, F. A. Calderon-Vargas, N. J. Mayhall, E. Barnes, and S. E. Economou, "Adaptive quantum approximate optimization algorithm for solving combinatorial problems on a quantum computer," Phys. Rev. Res. **4**, 033029 (2022).

[68]V. Kremenetski, T. Hogg, S. Hadfield, S. J. Cotton, and N. M. Tubman, "Quantum alternating operator ansatz (QAOA) phase diagrams and applications for quantum chemistry," arXiv **2108.13056v2** (2021).

[69]G. Matos, S. Johri, and Z. Papić, "Quantifying the efficiency of state preparation via quantum variational eigensolvers," PRX Quantum **2**, 010309 (2021).

[70]Z.-H. Sun, Y.-Y. Wang, J. Cui, and H. Fan, "Improving the performance of quantum approximate optimization for preparing non-trivial quantum states without translational symmetry," New J. Phys. **25**, 013015 (2023).

[71]G. Pagano, A. Bapat, P. Becker, K. S. Collins, et al., "Quantum approximate optimization of the long-range ising model with a trapped-ion quantum simulator," Proceedings of the National Academy of Sciences **117**, 25396–25401 (2020).

[72]P. K. Barkoutsos, G. Nannicini, A. Robert, I. Tavernelli, and S. Woerner, "Improving Variational Quantum Optimization using CVaR," Quantum **4**, 256 (2020).

[73]L. Li, M. Fan, M. Coram, P. Riley, and S. Leichenauer, "Quantum optimization with a novel gibbs objective function and ansatz architecture search," Phys. Rev. Res. **2**, 023074 (2020).

[74]G. E. Crooks, "Performance of the quantum approximate optimization algorithm on the maximum cut problem," arXiv **1811.08419** (2018).

[75]J. Basso, E. Farhi, K. Marwaha, B. Villalonga, and L. Zhou, "The Quantum Approximate Optimization Algorithm at High Depth for MaxCut on Large-Girth Regular Graphs and the Sherrington-Kirkpatrick Model," in 17th conference on the theory of quantum computation, communication and cryptography (tqc 2022), Vol. 232, edited by F. Le Gall and T. Morimae, Leibniz International Proceedings in Informatics (LIPIcs) (2022), 7:1–7:21.

[76]R. Shaydulin, P. C. Lotshaw, J. Larson, J. Ostrowski, and T. S. Humble, "Parameter transfer for quantum approximate optimization of weighted maxcut," ACM Transactions on Quantum Computing **4**, 10.1145/3584706 (2023).

[77]*Quantinuum system model H1 product data sheet*, Mar. 2022.

[78]*Quantinuum system model H1 emulator data sheet*, Mar. 2022.

[79]T. M. Mintz, A. J. McCaskey, E. F. Dumitrescu, S. V. Moore, S. Powers, and P. Lougovski, "Qcor: a language extension specification for the heterogeneous quantum-classical model of computation," J. Emerg. Technol. Comput. Syst. **16**, 10.1145/3380964 (2020).

[80]F Barahona, "On the computational complexity of Ising spin glass models," J. Phys. A: Math. Gen. **15**, 3241 (1982).

[81]H. Rieger and A. P. Young, "Quantum spin glasses," in Complex behaviour of glassy systems, Vol. 492, edited by M. Rubí and C. Pérez-Vicente, Lecture Notes in Physics (1997).

[82]P. Reiss, D. Graf, A. A. Haghighirad, T. Vojta, and A. I. Coldea, "Signatures of a quantum griffiths phase close to an electronic nematic quantum phase transition," Phys. Rev. Lett. **127**, 246402 (2021).

[83]Ze Hu, Z. Ma, Y.-D. Liao, H. Li, et al., "Evidence of the Berezinskii-Kosterlitz-Thouless phase transition in a frustrated magnet," Nat Commun **11**, 5631 (2020).

[84]J. M. Kosterlitz and D. J. Thouless, "Ordering, metastability and phase transitions in two-dimensional systems," J. Phys. C: Solid State Phys. **6**, 1181 (1973).

[85]L. D. C. Jaubert and P. C. W. Holdsworth, "Signature of magnetic monopole and Dirac string dynamics in spin ice," Nature Phys **5**, 258–261 (2009).

4. PROJECT III: A CLASSICAL ANALOGUE OF ENTANGLEMENT

The contents of this chapter are adapted from the following article:

B. Khalid and S. Kais, "A classical analogue of entanglement for a kicked top", arXiv preprint: 2411.08857v2 (2025.)

Abstract: *It is widely believed that quantum mechanics cannot exhibit chaos, since unitarity of time evolution ensures that distances between quantum states are preserved. However, Ballentine has suggested that a parallel argument can be constructed in classical mechanics that would seem to deny the existence of classical chaos too [1]. The argument works by describing classical states as probability distributions in phase space and showing that the inner product between distributions on phase space is preserved under Liouvillian dynamics. This leads Ballentine to conclude that the more faithful classical analogy of a quantum state is not a single phase space trajectory but is instead a phase space distribution, and chaos in such states must be identified by some statistical signatures instead of exponential separation of nearby states. The search for these signatures is the primary goal in quantum chaos research [2–4]. However, this perspective also naturally motivates the search for classical analogues of these signatures, to reveal the inner machinery of chaos in quantum systems. One widely recognized signature of chaos in quantum systems is the dynamical generation of entanglement. Chaos in the classical system is correlated with a greater entanglement production in the corresponding quantum system [5–25]. One of the most well-studied examples of this is the kicked top model [26]. In this chapter, we construct a classical analogue of bipartite entanglement in terms of the mutual information between phase space distributions of subsystems and find completely analogous signatures of chaos as those found in entanglement for the kicked top Hamiltonian.*

4.1 Introduction

Quantum chaos is the study of the quantum mechanical properties characteristic of systems that exhibit chaos classically [2–4]. Traditionally, the primary focus in the field has been on the determination of universal features in the spectral statistics and the eigenstates of chaotic Hamiltonians. However, in recent years, developments in quantum information science and phenomenal advances in quantum simulation technologies have enabled novel theoretical and experimental avenues for exploring the dynamical manifestations of chaos in quantum systems. Information-theoretic measures such as entanglement entropy, quantum Fisher information, OTOCs (out-of-time-order correlators), etc. have been suggested as new probes for tracking quantum chaos. Consequently, a fresh understanding of quantum chaos has emerged that has revealed its fundamental significance in quantum dynamical processes, crucial to understanding decoherence, many-body systems and black hole physics, such as entanglement generation [5–25], information scrambling [27–31] and quantum thermalization [32–36].

The issue of quantum entanglement has been the subject of much debate since Einstein, Podolsky and Rosen pointed out the "bizarre" consequences it can lead to [37]. Schrödinger declared it as "the characteristic trait of quantum mechanics, the one that enforces its entire departure from classical lines of thought [38]." In its essence, entanglement expresses the *nonlocal* and *nonseparable* nature of quantum states in a form that is completely alien to classical physics [39]. In quantum information science, it has been identified as a central resource in quantum communication protocols, quantum cryptography and quantum information processing and storage [40, 41].

Remarkably, the dynamical generation of entanglement (within the system or with an environment) is intimately tied to the chaoticity properties of the underlying classical phase space. It has been observed that wave packets centered on regions of phase space that are classically chaotic yield a greater entanglement entropy production than classically regular regions. For chaotic initial conditions, the entanglement entropy grows linearly at a rate given by the sum of the positive Lyuapunov exponents, the classical Kolmogorov-Sinai entropy rate; whereas for the regular case, the entropy grows only logarithmically with time [5–25].

A system for which the chaos-entanglement relationship has been extensively studied is the kicked top model [10, 16, 21–26]. In this system, the evolution of the angular momentum $\mathbf{J}$ ("the top") is governed by two kinds of process: (i) precession of $\mathbf{J}$ around a fixed axis at a constant rate and (ii) a periodic sequence of kicks that bring about an instantaneous change in $\mathbf{J}$. The Hamiltonian for this system commutes with $\mathbf{J}^2$, so the quantum evolution is confined within a subspace characterized by an eigenvalue $j(j+1)$ of $\mathbf{J}^2$. Moreover, the model is chaotic in the classical limit $j \to \infty$. This model was introduced by Haake et al. to analyze how chaos arises as a system becomes more and more classical [26].

A particularly interesting realization of this model is in terms of a collection of spins-1/2, where $\mathbf{J}$ denotes the collective angular momentum of the spins. This approach has been used to study bipartite entanglement in the model as a function of time and initial state [21–25]. In a common scenario, the system is initialized in a spin-coherent state i.e. a minimum uncertainty angular momentum state, and the growth of entanglement entropy of a single spin-1/2 is tracked. The growth of entropy has been found to carry strong signatures of chaos in the underlying classical dynamics: (i) for an initial state centered in a classically chaotic region of phase space, the entanglement entropy grows linearly at a rate given by the Lyuapunov exponent before reaching the saturation point, whereas, for the classically regular case, the entropy grows only logarithmically; (ii) for initial conditions centered in classically chaotic regions of phase space, the equilibrium entropy (also known as average entropy) is larger compared to those centered in classically regular regions [21–25].

With recent advances in a variety of quantum simulation platforms, there has also been a lot of interest in experimental investigations of this correlation. A quantum simulation of the kicked top was achieved by Chaudhury et al. using the $F = 3$ hyperfine ground state of ^{133}Cs [23]. In their experiment, the total angular momentum in the Hamiltonian was taken to be the sum of the electron and nuclear spins of a single ^{133}Cs atom. Consequently, the theoretically predicted correspondence between entanglement, as quantified by the linear entropy of the electron spin, and classical chaos was corroborated. Later, similar conclusions were obtained by Neill et al. in their quantum simulation experiment of the same Hamiltonian using a three-qubit ring of planar transmons [24]. Commenting on their findings, they added,

"it is interesting to note that chaos and entanglement are each exclusive to their respective classical and quantum domains, and any connection is surprising."

The connection is surprising because a purely quantum property (entanglement) is being related with a purely classical one (chaos), each one understood to have no counterpart on the other side. The standard argument for the absence of chaos in quantum mechanics proceeds like this. Suppose $|\psi_1(0)\rangle$ and $|\psi_2(0)\rangle$ represent two initially close quantum states i.e. $\langle\psi_1(0)|\psi_2(0)\rangle = 1 - \epsilon$ (ϵ being a small number.) Under unitary evolution of $|\psi_1(0)\rangle$ and $|\psi_2(0)\rangle$, we should have $\langle\psi_1(t)|\psi_2(t)\rangle = 1 - \epsilon$ for all times t. So, the states do not separate in time and this is taken to imply that there can be no chaos in quantum mechanics [1]. However, Ballentine has argued that a parallel argument can be constructed in classical mechanics too if classical states are taken to be represented by probability distributions in phase space. For two phase space distributions $\rho_1(q, p, t)$ and $\rho_2(q, p, t)$, the construction $\{\rho_1(t)|\rho_2(t)\} = \int\int \rho_1(q, p, t)\rho_2(q, p, t)\, dqdp$ is a well-defined inner product on phase space and is invariant under the Liouvillian dynamics of ρ_1 and ρ_2. But no one can deny the existence of chaos in classical mechanics. Ballentine then concludes that the confusion about quantum chaos is merely a reflection of the confusion about the notion of "state" in classical and quantum mechanics. The more adequate classical analogue of a quantum state is not a single trajectory but a phase space distribution, and chaos in such states must be identified by some statistical signatures [1].

One such signature is the growth of entanglement in quantum systems as discussed above. This naturally raises the question of what would be a good classical analogue of entanglement in the statistical interpretation of classical physics. Constructing such an analogue is desirable for two related reasons: (i) a comparison between conceptually similar identifiers of chaos across the classical-quantum divide can enable a fresh understanding of the classical-quantum correspondence, especially in light of the issues raised by chaos; (ii) since quantum chaos is still far from understood, an analysis of a classical analogue of a quantum signature of chaos can reveal the inner machinery of quantum chaos, that would otherwise be hidden from view.

To construct this analogue, it would be convenient to consider the meaning of entanglement in the Wigner function formalism of quantum mechanics as it provides a visualization

of quantum states in phase space. In this formulation, the state of a quantum system is represented by a real-valued function in phase space $W(q,p)$, called the Wigner function. This function in many ways acts like the classical phase space density $\rho(q,p)$. However, an important difference is that $W(q,p)$ is not really a distribution as it can take negative values unlike $\rho(q,p)$ [42, 43].

In the Wigner function formalism, two systems are entangled iff their collective Wigner function is nonseparable i.e. if $W(q_1,q_2,p_1,p_2)$ is the Wigner function of the total system and $W_1(q_1,p_1) = \int\int W(q_1,q_2,p_1,p_2)\, dq_2dp_2$ and $W_2(q_2,p_2) = \int\int W(q_1,q_2,p_1,p_2)\, dq_1dp_1$ are the Wigner functions of systems 1 and 2 respectively, then $W(q_1,q_2,p_1,p_2) \neq W_1(q_1,p_1) \times W_2(q_2,p_2)$. This motivates the construction of a classical analogue in terms of the separability of phase space density ρ. The classical state is separable iff $\rho(q_1,q_2,p_1,p_2) = \rho_1(q_1,p_1)\times\rho_2(q_2,p_2)$ and is nonseparable otherwise, where $\rho_1(q_1,p_1) = \int \rho(q_1,q_2,p_1,p_2)dq_2dp_2$ and $\rho_2(q_2,p_2) = \int \rho(q_1,q_2,p_1,p_2)\, dq_1dp_1$. To quantify the degree of nonseparability, we will use mutual information which for two random variables X_1 and X_2 is defined as $I_{12} = \int\int \rho(X_1,X_2)\log\Big[\rho(X_1,X_2)/\big(\rho_1(X_1)\rho_2(X_2)\big)\Big]dX_1dX_2$. $I_{12} \geq 0$ and $I_{12} = 0$ iff $\rho(X_1,X_2) = \rho_1(X_1)\rho_2(X_2)$. For other measures of classical nonseparability, see references [7, 13, 18, 19].

In this chapter, we have analyzed the growth of mutual information in the classical kicked top. We bipartition the total angular momentum $\mathbf{J}$ into two parts $\mathbf{J}_1$ and $\mathbf{J}_2$ and compute the mutual information between the variables on the two sides of the partition. We find striking resemblances between the growth of mutual information and the bipartite entanglement. Mutual information, like entanglement, carries clear signatures of chaos in the underlying dynamics. Under chaotic dynamics, it grows linearly at a rate proportional to the Lyuapunov exponent. Whereas, for regular dynamics, the growth starts to slow down well before equilibrium is attained. Similarly, initial states centered in chaotic regions of phase space end up with a higher mutual information at equilibrium compared to regular regions, in complete analogy with bipartite entanglement.

The organization of the chapter is as follows. In Sec. 4.2, we introduce the kicked top Hamiltonian and describe its classical dynamics. In Sec. 4.3, we recall the correspondence between entanglement and classical dynamics. Then, in Sec. 4.4, we present our calculations

for classical mutual information. Finally, in Sec. 4.5, we provide a summary of the results and an outlook for the future.

4.2 Classical Dynamics

Consider the angular momentum operator $\hbar\mathbf{J} = \hbar(J_x, J_y, J_z)$ satisfying the commutation relations $[J_i, J_j] = i\varepsilon_{ijk}J_k$. The Hamiltonian for the kicked top is then expressed in terms of $\mathbf{J}$ as [26],

$$H(t) = \frac{\hbar p}{\tau}J_y + \frac{\hbar\kappa}{2j}J_z^2 \sum_{n=-\infty}^{+\infty} \delta(t - n\tau). \tag{4.1}$$

The first term describes the precession of the rotor around the y-axis at a rate p/τ. The second term represents a periodic sequence of kicks separated by a period τ. Intuitively, this term can be thought of as a sudden precession around the z-axis by an angle proportional to J_z/j, where j is the total angular momentum quantum number. Once we initialize our system in the subspace characterized by the eigenvalue $j(j+1)$ of the operator $\mathbf{J}^2$, we stay within the same subspace for all times since $[\mathbf{J}^2, H(t)] = 0$. κ is a dimensionless constant which controls the strength of the kick. For this chapter, we are going to choose $p = \pi/2$ i.e. the top precesses around the y-axis by an angle $\pi/2$ between successive kicks.

Working in the Heisenberg picture, we are interested in tracking the evolution of $\mathbf{J}$ in time. The evolution of the operator J_i in n time steps can be represented as $J_i^{(n)} = (U^\dagger)^n\, J_i\, U^n$, where U is the unitary evolution corresponding to the interval τ between successive kicks [26],

$$U = e^{-i(\kappa/2j)J_z^2} e^{-i(\pi/2)J_y}. \tag{4.2}$$

The evolution of $\mathbf{J}$ can be represented in terms of the following non-linear operator recursion relations which determine how $\mathbf{J} = \mathbf{J}^{(i)}$ is updated to $\mathbf{J}' = \mathbf{J}^{(i+1)}$ after each time step [26],

$$\begin{aligned} J_x' &= \frac{1}{2}(J_z + iJ_y)\, \mathrm{e}^{-i\frac{\kappa}{j}(J_x - \frac{1}{2})} + \text{h.c.} \\ J_y' &= \frac{1}{2i}(J_z + iJ_y)\, \mathrm{e}^{-i\frac{\kappa}{j}(J_x - \frac{1}{2})} + \text{h.c.} \\ J_z' &= -J_x. \end{aligned} \tag{4.3}$$

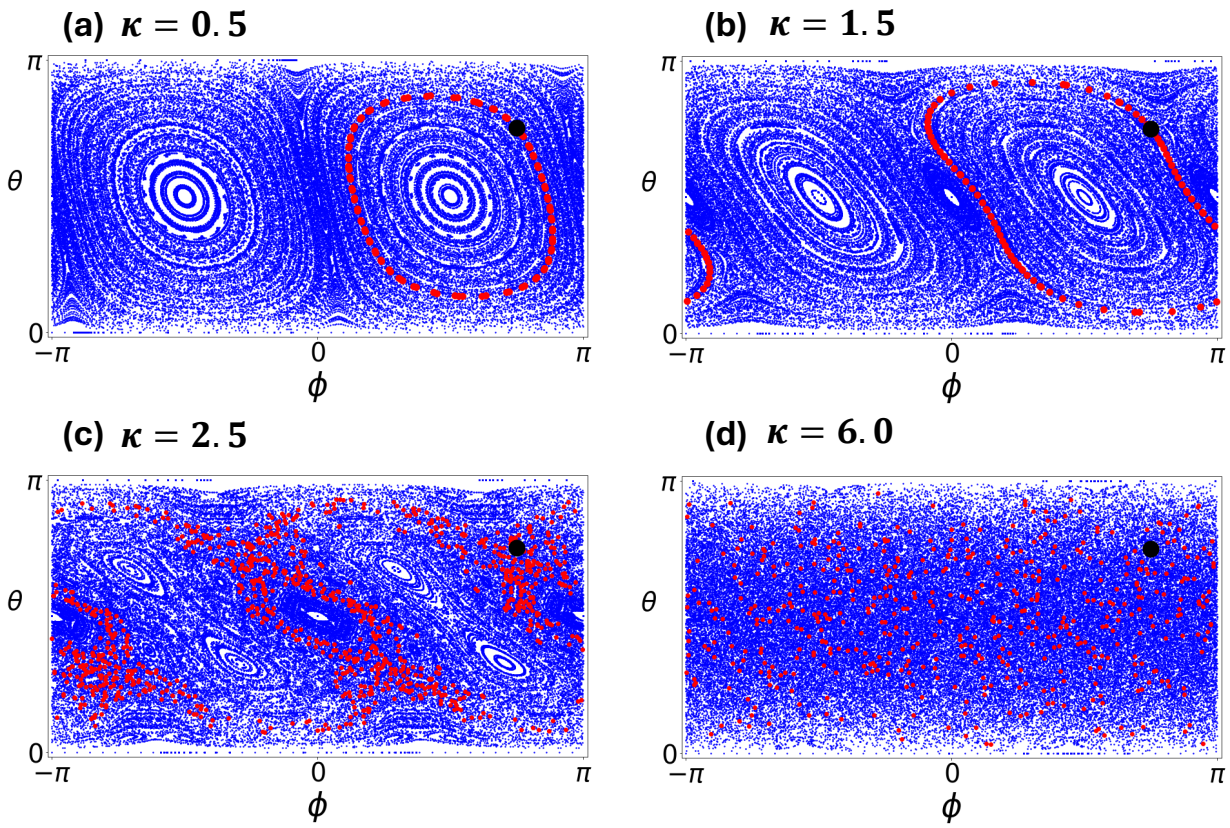

Figure 4.1. Classical phase portraits for the kicked top. The trajectories of rescaled angular momenta $\mathbf{X} = \mathbf{J}/j$ in the classical limit $j \to \infty$, represented in terms of the polar and the azimuthal angles on a unit sphere. As κ is tuned from low to high, an order-to-chaos transition occurs in the phase space. Red markers represent the trajectories corresponding to the initial condition $\theta_0 = 3\pi/4, \phi_0 = 3\pi/4$ (black marker.)

Defining the rescaled angular momentum as $\mathbf{X} = \mathbf{J}/j$ and taking the classical limit $j \to \infty$, we can track the evolution of the now real-valued $\mathbf{X} = (X, Y, Z)$ on the surface of a unit sphere using the following recursion relations obtained from (4.3),

$$\begin{aligned} X' &= \mathrm{Re}\{(Z + iY)\, e^{-i\kappa X}\} \\ Y' &= \mathrm{Im}\{(Z + iY)\, e^{-i\kappa X}\} \\ Z' &= -X. \end{aligned} \tag{4.4}$$

In Fig. 4.1, we have plotted some examples of the phase portraits in spherical coordinates (i.e. $X = \sin\theta\cos\phi$, $Y = \sin\theta\sin\phi$ and $Z = \cos\theta$) that are produced by the recursion relations (4.4) for different values of the kick strength κ. As we increase the kick strength κ, chaos emerges in the phase space and islands of regularity begin to shrink. Eventually, for a large enough value of κ, chaos completely takes over.

4.3 Quantum Entanglement

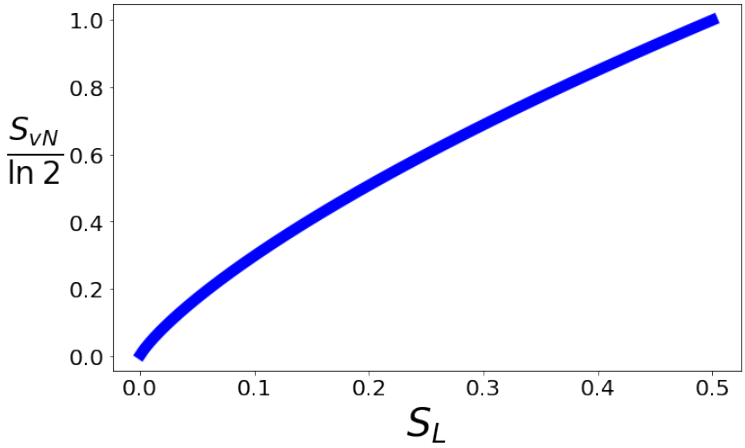

Figure 4.2. von Neumann entropy and linear entropy for spin-1/2 systems.

Consider a collection of N spins-1/2 with the corresponding spin operators $\mathbf{S}_i = (S_{ix}, S_{iy}, S_{iz})$ such that the dynamics of the total angular momentum $\mathbf{J} = \sum_{i=1}^{N} \mathbf{S}_i$ is governed by the Hamiltonian (4.1). In terms of the spin operators $\mathbf{S}_i$, the Hamiltonian can be re-written as

$$H(t) = \frac{\hbar\pi}{2\tau}\sum_{i=1}^{N} S_{iy} + \frac{\hbar\kappa}{2j}\left(\sum_{i=1}^{N} S_{iz}^2 + \sum_{i\neq j} S_{iz}S_{jz}\right)\sum_{n=-\infty}^{+\infty}\delta(t-n\tau). \tag{4.5}$$

Before each kick, each spin independently precesses around the y-axis by an angle $\pi/2$. Noting that $(\sum_{i=1}^{N} S_{iz}^2 + \sum_{i\neq j} S_{iz}S_{jz}) = J_z\,(\sum_{i=1}^{N} S_{iz})$, the kick can be understood as causing a sudden precession of each spin around the z-axis by an angle proportional to J_z/j, a collective variable of the system.

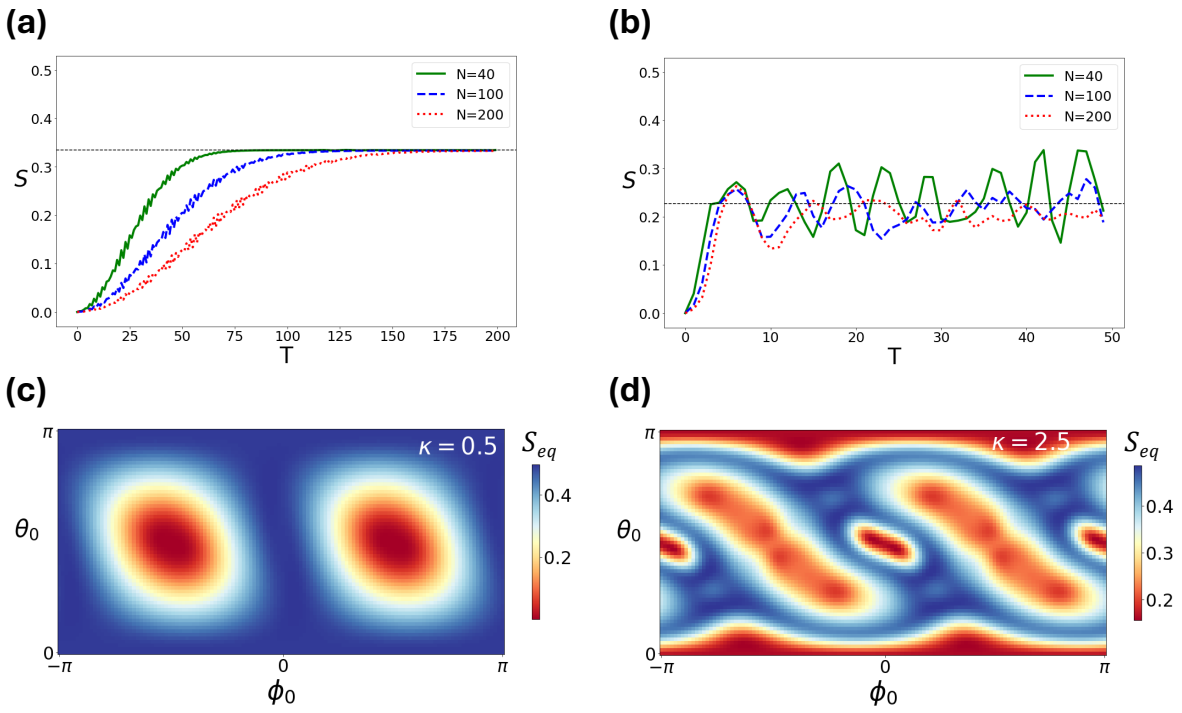

Figure 4.3. Linear entropy. Linear entropy of a single spin $S = 1 - \mathrm{Tr}_1(\rho_1^2)$ as a function of time steps T and initial orientation (θ_0, ϕ_0). (a) and (b) show the time dynamics of S with the initial orientation $(\theta_0 = 3\pi/4, \phi_0 = 3\pi/4)$ for $\kappa = 0.5$ and $\kappa = 2.5$ respectively. (c) and (d) display the equilibrium value S_{eq} of linear entropy as a function of the initial orientation (θ_0, ϕ_0) for $\kappa = 0.5$ and $\kappa = 2.5$ respectively. The system size is taken to be $N = 40$. S_{eq} is estimated by averaging S over an appropriate time interval after reaching saturation. For (c), the average is performed for $60 \leq T \leq 100$ whereas for (d), the average is computed over $20 \leq T \leq 40$. There is a striking resemblance of the plots (c) and (d) with the corresponding classical phase portraits shown in Figs. 4.1(a) and (c).

In this section, we recall the dynamics of bipartite entanglement generated by this Hamiltonian. We initialize the system in the spin-coherent state,

$$|\psi(t=0)\rangle = \bigotimes_{i=1}^{N} |\theta_0, \phi_0\rangle_i = \exp\{i\theta_0(J_x \sin\phi_0 - J_y \cos\phi_0)\}\,|j, j\rangle\,. \tag{4.6}$$

This is the minimum uncertainty angular momentum state pointing along a certain direction (θ_0, ϕ_0) for a given total angular momentum quantum number j. For N spins-1/2 pointing in the same direction, we have $j = N/2$. $|\theta_0, \phi_0\rangle$ is the spin-1/2 state pointing along (θ_0, ϕ_0)

on the Bloch sphere i.e. $|\theta_0, \phi_0\rangle = \cos(\theta_0/2)\,|\uparrow\rangle + e^{-i\phi_0}\sin(\theta_0/2)\,|\downarrow\rangle$. The initial state is completely separable, however, entanglement is generated as a result of the unitary evolution (4.2).

To track the dynamics of bipartite entanglement, we use linear entropy of a single spin-1/2 defined as $S = 1 - \mathrm{Tr}_1(\rho_1^2)$, where ρ_1 is the reduced density matrix for a single spin. $S = 0$ for a pure state, and is maximized at $S = 0.5$ for a completely mixed state. This measure is used only for convenience; qualitatively, the results are expected to be independent of the choice for pure states [21]. Even quantitatively, there is a nearly linear relationship between von Neumann entropy and linear entropy for spin-1/2 states as shown in Fig. 4.2.

In Figs. 4.3(a) and (b), we have plotted the time dynamics of entropy for the regular ($\kappa = 0.5$) and chaotic ($\kappa = 2.5$) scenarios, respectively. For both cases, the initial state is centered at ($\theta_0 = 3\pi/4, \phi_0 = 3\pi/4$). The dynamics has been plotted for three different system sizes $N = 40,\ 100,\ 200$. For both scenarios, entropy grows consistently before saturating after some time T_{eq}. For the regular case, T_{eq} increases with the size of the system N as $O(\sqrt{N})$. On the other hand, the increase is only logarithmic $O(\ln N)$ for the chaotic case [25]. Moreover, the rate of entropy growth in the regular case starts to slow down well before reaching saturation, signifying a logarithmic growth of entropy. However, for the chaotic case, the growth is linear at a rate given by the Lyuapunov exponent [25]. For larger times, the entropy undergoes sequences of collapses and revivals, which recede into the indefinite future as the system size approaches the thermodynamic limit.

In Figs. 4.3(c) and (d), equilibrium values of entropy S_{eq} have been plotted as a function of the initial orientations (θ_0, ϕ_0) for $N = 40$. S_{eq} is estimated by averaging the entropy over a chosen time interval after saturation. Remarkably, the plots of entanglement reflect the structure of the classical phase space in Figs. 4.1(a) and (c). For $\kappa = 2.5$ specifically, we find that the regions of chaos in classical phase space correspond to regions of higher entropy on the quantum side and the regions of regularity correspond to a lower entropy [24].

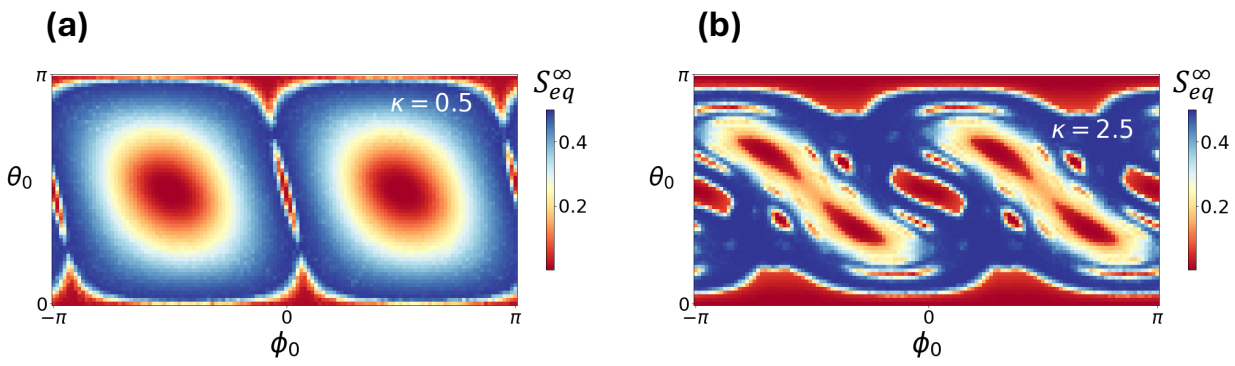

Figure 4.4. Linear entropy in the thermodynamic limit. We have estimated the equilibrium value of linear entropy in the thermodynamic limit S^{∞}_{eq} as a function of the initial orientation (θ_0, ϕ_0). For each (θ_0, ϕ_0), $S^{\infty} = \langle (\Delta X)^2 \rangle /2$ is computed classically by evolving 200 trajectories sampled from a region of angular spread $\sin\theta_0 \Delta\theta\Delta\phi = 1/j$ for $j = 100$ centered at (θ_0, ϕ_0). For both plots, S^{∞} is averaged between $400 \leq T \leq 500$.

Finally, to obtain an estimate of entropy in the thermodynamic limit, we note that linear entropy for a state symmetric with respect to all the spins can be expressed as [22],

$$S = 1 - \mathrm{Tr}_1(\rho_1^2) = \frac{1}{2}\Big[1 - \frac{1}{j^2}(\langle J_x\rangle^2 + \langle J_y\rangle^2 + \langle J_z\rangle^2)\Big]. \tag{4.7}$$

As $j \to \infty$, this becomes $S = \langle (\Delta X)^2 \rangle /2$ where $\langle (\Delta X)^2 \rangle = (\langle \mathbf{J}^2 \rangle - \langle \mathbf{J} \rangle^2)/j^2$. We can then compute $\langle (\Delta X)^2 \rangle$ in the classical limit to estimate S in the thermodynamic limit. The results for this calculation are shown in Fig. 4.4. For each (θ_0, ϕ_0), we evolved 200 trajectories initialized in a region of angular spread $\sin\theta_0 \Delta\theta\Delta\phi = 1/j$ centered at (θ_0, ϕ_0) to calculate $\langle (\Delta X)^2 \rangle$. These plots contain some extra minima regions (i.e. red regions) located around the fixed points of the classical phase space [Figs. 4.1(a) and (c)] that were not captured in Figs. 4.3(c) and (d).

4.4 Classical Mutual Information

In the *Introduction*, we have motivated a classical notion of nonseparability quantified by mutual information. In this section, we use that measure to track nonseparability in the

classical kicked top. Suppose we bipartition the system by dividing $\mathbf{J}$ into $\mathbf{J}_1$ and $\mathbf{J}_2$ so that $\mathbf{J} = \mathbf{J}_1 + \mathbf{J}_2$. The Hamiltonian (4.1) can then be re-expressed in terms of $\mathbf{J}_1$ and $\mathbf{J}_2$ as

$$H(t) = \frac{\hbar\pi}{2\tau}(J_{1y} + J_{2y}) + \frac{\hbar\kappa}{2j}(J_{1z}^2 + J_{2z}^2 + 2J_{1z}J_{2z}) \sum_{n=-\infty}^{+\infty} \delta(t - n\tau). \tag{4.8}$$

$\mathbf{J}_1^2$ and $\mathbf{J}_2^2$ are conserved quantities since $[\mathbf{J}_{1,2}^2, H(t)] = 0$. The unitary evolution operator over one cycle is $U = U_{z^2} U_{12} U_y$ where $U_{z^2} = e^{-i(\kappa/2j)J_{1z}^2} e^{-i(\kappa/2j)J_{2z}^2}$, $U_{12} = e^{-i(\kappa/j)J_{1z}J_{2z}}$ and $U_y = e^{-i(\pi/2)J_{1y}} e^{-i(\pi/2)J_{2y}}$. We can compute $\mathbf{J}_1' = U^\dagger \mathbf{J}_1 U$ to produce the following recursion relations for the update of angular momentum of subsystem 1 (see supplementary information S-I,)

$$\begin{aligned} J_{1x}' &= \frac{1}{2}(J_{1z} + iJ_{1y})\, \mathrm{e}^{-i\frac{\kappa}{j}(J_{1x} + J_{2x} + \frac{1}{2})} + \text{h.c.} \\ J_{1x}' &= \frac{1}{2i}(J_{1z} + iJ_{1y})\, \mathrm{e}^{-i\frac{\kappa}{j}(J_{1x} + J_{2x} + \frac{1}{2})} + \text{h.c.} \\ J_{1x}' &= -J_{1x}. \end{aligned} \tag{4.9}$$

For $\mathbf{J}_2'$, we only need to interchange the indices 1 and 2 in the above equations. Finally, defining $\mathbf{X}_{1,2} = \mathbf{J}_{1,2}/j$ and taking the classical limit $j \to \infty$ we get

$$\begin{aligned} X_1' &= \mathrm{Re}\{(Z_1 + iY_1)\, e^{-i\kappa(X_1 + X_2)}\} \\ Y_1' &= \mathrm{Im}\{(Z_1 + iY_1)\, e^{-i\kappa(X_1 + X_2)}\} \\ Z_1' &= -X_1. \end{aligned} \tag{4.10}$$

We take subsystem 1 to be the analogue of a spin-1/2, while subsystem 2 represents the rest of the system. This motivates our choice $\|\mathbf{J}_1\| = 1/2$ and $\|\mathbf{J}_2\| = j - \|\mathbf{J}_1\|$. We initialize the system in a completely separable distribution i.e. the distribution for the total system is simply a product of the marginal distributions for subsystems 1 and 2. Both marginal distributions are taken to be uniformly distributed around (θ_0, ϕ_0). For subsystem 2, the angular spread of the initial distribution is taken to be $\sin\theta_0 \Delta\theta \Delta\phi = 1/j$, in analogy with the quantum state (4.6). On the other hand, for subsystem 1, the initial angular spread is fixed at $\sin\theta_0 \Delta\theta \Delta\phi = 1/4$. We sample initial conditions from this initial distribution for the

total system, evolve them into trajectories and estimate the mutual information I_{12} between the variables $X_1 = J_{1x}/j$ and $X_2 = J_{2x}/j$ based on k-nearest neighbor statistics [44].

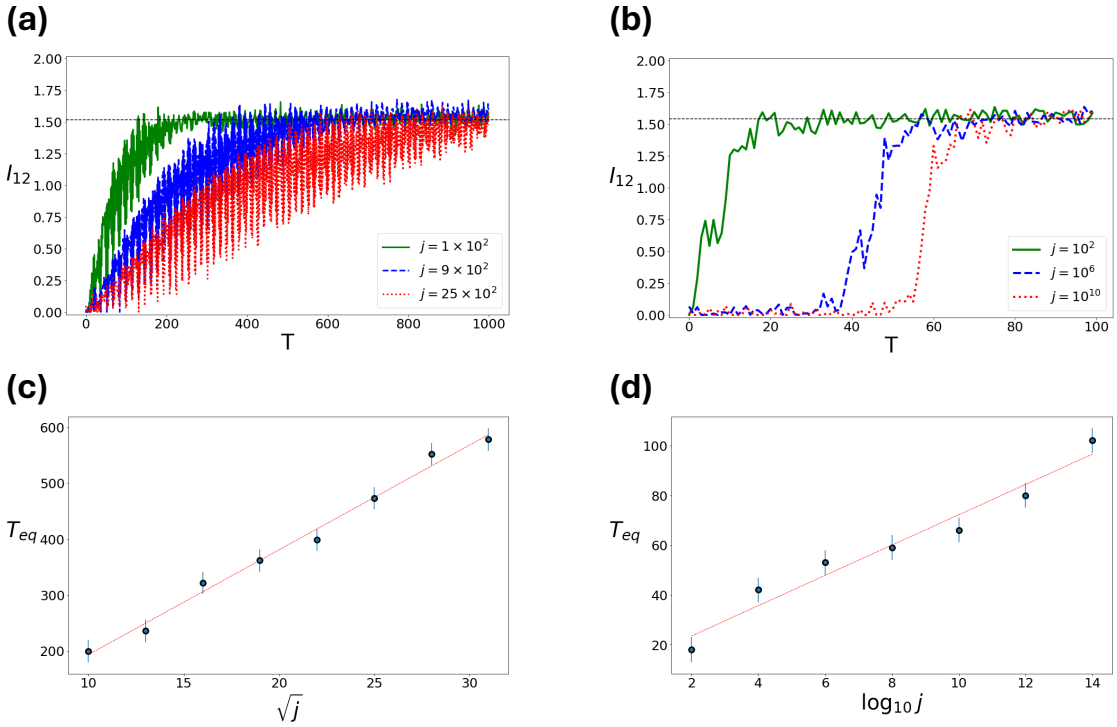

Figure 4.5. Mutual information growth and system size. Mutual information I_{12} between the variables $X_1 = J_{1x}/j$ and $X_2 = J_{2x}/j$ with initial orientation $(\theta_0 = 3\pi/4, \phi_0 = 3\pi/4)$ for $\kappa = 0.5$ [(a) and (c)] and $\kappa = 2.5$ [(b) and (d)], respectively. The system starts in a completely separable distribution with angular spread $\sin\theta_0 \Delta\theta\Delta\phi = 1/4$ for subsystem 1 and $\sin\theta_0 \Delta\theta\Delta\phi = 1/j$ for subsystem 2. A sample of 500 points is drawn from this distribution and the corresponding trajectories are evolved to compute the statistics. (a) and (b) show the growth of I_{12} with time, whereas, (c) and (d) display the advancement in saturation time T_{eq} with system size j.

In Fig. 4.5, we have shown the dynamics of I_{12} for different system sizes j (recall $j = N/2$.) Fig. 4.5(a) shows the growth of I_{12} for regular classical dynamics. The rate of growth decays with time, a signature of logarithmic growth. Moreover, as the system size j increases, the growth slows further as the system is expected to take longer to reach equilibrium. Plot (c) shows that the saturation time T_{eq} increases as $O(\sqrt{j})$ with j. All these trends are completely analogous to the growth of quantum entropy for classically regular phase space.

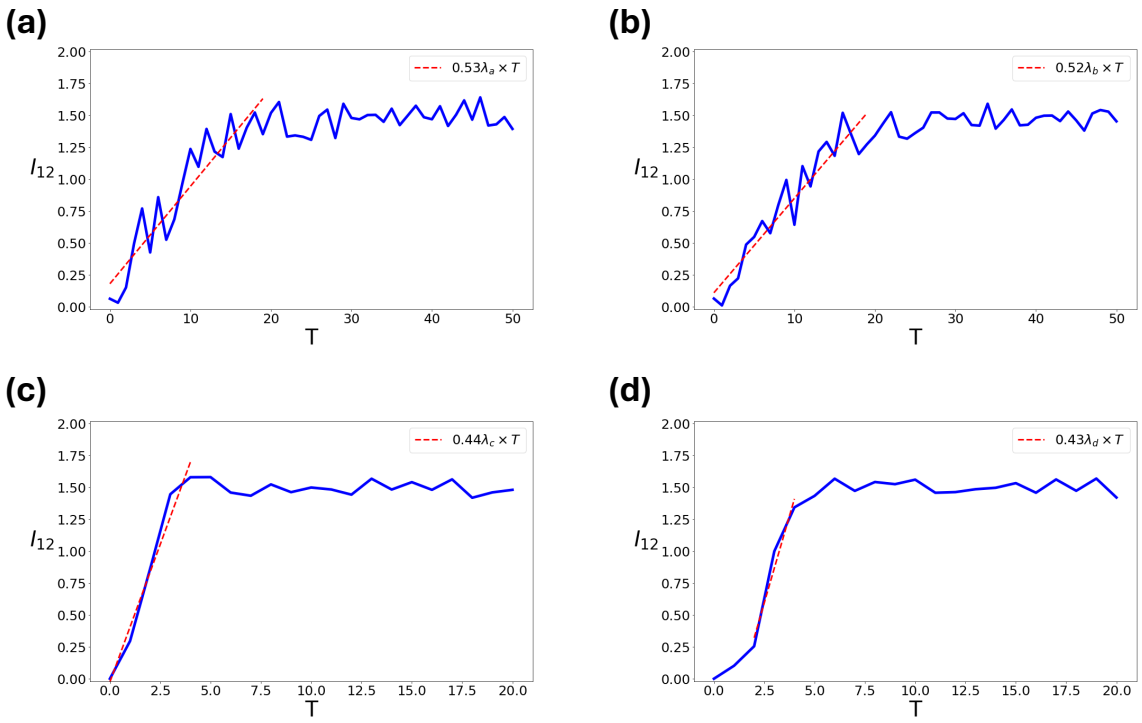

Figure 4.6. Mutual information growth and Lyuapunov exponents. A comparison of the growth rate of I_{12} with the corresponding Lyuapunov exponents for four different cases: (a) $\kappa = 2.5$, $(\theta_0 = 3\pi/4, \phi_0 = 3\pi/4)$, $\lambda_a = 0.145$; (b) $\kappa = 2.5$, $(\theta_0 = 1.0, \phi_0 = \pi/10)$, $\lambda_b = 0.143$; (c) $\kappa = 6.0$, $(\theta_0 = 3\pi/4, \phi_0 = 3\pi/4)$, $\lambda_c = 0.978$; (d) $\kappa = 8.0$, $(\theta_0 = 3\pi/4, \phi_0 = 3\pi/4)$, $\lambda_d = 1.254$. For all these scenarios, $j = 100$, and 200 samples are drawn from the initial distribution.

In Fig. 4.5(b), we have plotted the dynamics of I_{12} for chaotic classical dynamics. Clearly, I_{12} grows almost linearly once the initial transient subsides, during which it does not grow at all, for larger j. Moreover, plot (d) shows that the saturation time T_{eq} for I_{12}, just like quantum entropy, increases with j much more slowly as $O(\ln j)$ compared to the regular case. The uniform growth rate for quantum entropy under chaotic classical dynamics is known to be proportional to the positive Lyuapunov exponent[1] of the corresponding classical dynamics [25]. In Fig. 4.6, we present evidence that this holds for mutual information I_{12} too. We have compared the growth rate of I_{12} with the corresponding Lyuapunov exponents for four different cases. To estimate the Lyuapunov exponents, we used the standard algorithm of

[1]↑More generally, the growth rate is proportional to the sum of the positive Lyuapunov exponents, but for the kicked top, there is just one such exponent.

Benettin et al [25, 45–47] (see supplementary information S-II.) In all these cases, we find that the growth rate is $\sim 0.5 \times \lambda$, where λ is the positive Lyuapunov exponent corresponding to the point (θ_0, ϕ_0).

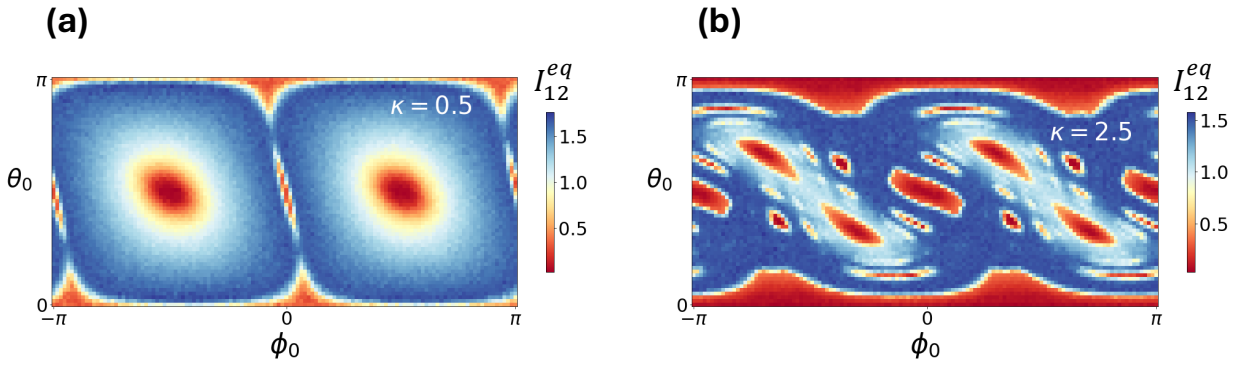

Figure 4.7. Equilibrium mutual information. Equilibrium value of mutual information I_{12}^{eq} is estimated as a function of (θ_0, ϕ_0) for: (a) $\kappa = 0.5$ and (b) $\kappa = 2.5$. For each (θ_0, ϕ_0), 200 trajectories are sampled to compute the statistics and $j = 100$ is used. To obtain I_{12}^{eq}, I_{12} is averaged between $400 \leq T \leq 500$ for both cases. The plots are remarkably similar to equilibrium entropy S_{eq} in Figs. 4.3 and 4.4.

Finally, in Fig. 4.7, we have plotted the equilibrium value of I_{12} as a function of the initial orientation (θ_0, ϕ_0) for regular $(\kappa = 0.5)$ and chaotic $(\kappa = 2.5)$ cases, respectively. The equilibrium value I_{12}^{eq} is estimated by averaging I_{12} in the time range $400 \leq T \leq 500$ for both cases. The plots obtained look remarkably similar to the plots of equilibrium entropy S_{eq} in Figs. 4.3 and 4.4. Like quantum entropy, classical mutual information as a function of the initial orientation is also able to reflect the structure of the classical phase space. So, the results in Figs. 4.5, 4.6 and 4.7 show that the signatures of chaos associated with entanglement have clear analogues in the statistical interpretation of classical mechanics.

4.5 Summary and Outlook

In this chapter, we have demonstrated that the signatures of chaos displayed by biparitite entanglement can also be observed through a classical statistical measure. Our measure is based on the mutual information between the marginal phase space densities of individual

subsystems. We have evolved this quantity dynamically using the kicked top Hamiltonian. Our results can be summarized as follows: (i) mutual information I_{12} grows logarithmically for regular classical dynamics, whereas, the growth is linear and the rate of growth is proportional to the Lyuapunov exponent for chaotic dynamics; (ii) the saturation time T_{eq} grows with system size $j = N/2$ as $O(\sqrt{j})$ for regular dynamics and $O(\ln j)$ for chaotic dynamics; (iii) the equilibrium mutual information I_{12}^{eq}, estimated by averaging I_{12}, is larger for initial conditions that produce chaotic trajectories than those that lead to regular motion for a mixed regular-chaotic phase space. All of these are well-known signatures of chaos in bipartite quantum entanglement [21–25].

Although this study has been conducted using a specific measure of classical nonseparability, we believe that the results should be independent of the choice of measure (for other measures, see references [7, 13, 18, 19]). Moreover, while the focus herein has been on bipartite entanglement, quantum entanglement is certainly not restricted to bipartite measures only. Multipartite entanglement measures such as quantum Fisher information are also known to exhibit signatures of chaos [25]. Therefore, an important direction for the future would be to extend this classical analogy to multipartite measures. Another important question that we leave for future exploration is whether this analogy carries over to more nontrivial states beyond the simple spin-coherent states considered in this work.

Finally, these results might also have implications for the foundations of classical and quantum mechanics. In recent years, Gisin et al. have advanced an alternative interpretation of classical mechanics as an attempt to bridge the conceptual gap between classical and quantum physics [48–54]. Their basic claim is that the orthodox understanding of classical mechanics takes for granted an assumption that they have called the *principle of infinite precision*; that physical quantities can be specified to an infinite number of digits. Once this assumption is relaxed, they have argued, many features exclusively attributed to quantum physics such as the fundamental role of measurement and the nonseparability of states appear analogously in classical physics too [54].

We have argued in this chapter that classical nonseparability certainly reveals new connections between classical and quantum realms. Gisin et al. go a step further and allow the possibility for classical nonseparability to be a physically real phenomenon. However,

the question will remain unresolved until experimental investigations are carried out. One possible route could be to monitor the motion of charged particles in classical and quantum wells [55]. Charges moving between parallel planar potential barriers under a magnetic field tilted with respect to the barriers exhibit chaotic dynamics. The emergence of chaos in this system is described by the kicked top map in certain regimes. In the classical version of the system, chaos is accompanied with a large energy transfer between the longitudinal and the cyclotron motion of the charges; however, this energy exchange is suppressed in the quantum limit [55]. Further analysis will be needed to investigate the possible experimental signatures of classical nonseparability in this system.

Bibliography

[1]L. E. Ballentine, "The emergence of classical properties from quantum mechanics: new problems from old," in *Fundamental problems in quantum physics*, edited by M. Ferrero and A. van der Merwe (Springer Netherlands, Dordrecht, 1995), pp. 15–28.

[2]M. V. Berry, "The Bakerian Lecture, 1987. Quantum chaology," Proc. R. Soc. Lond. A **413**, 183–198 (1987).

[3]M. C. Gutzwiller, *Chaos in Classical and Quantum Mechanics* (Springer New York, NY, 1990).

[4]F. Haake, *Quantum Signatures of Chaos*, 3rd ed. (Springer Berlin, Heidelberg, 2010).

[5]W. H. Zurek and J. P. Paz, "Decoherence, chaos, and the second law," Phys. Rev. Lett. **72**, 2508–2511 (1994).

[6]W. H. Zurek and J. P. Paz, "Quantum chaos: a decoherent definition," Physica D: Nonlinear Phenomena **83**, Quantum Complexity in Mesoscopic Systems, 300–308 (1995).

[7]R. Zarum and S. Sarkar, "Quantum-classical correspondence of entropy contours in the transition to chaos," Phys. Rev. E **57**, 5467–5471 (1998).

[8]K. Furuya, M. C. Nemes, and G. Q. Pellegrino, "Quantum dynamical manifestation of chaotic behavior in the process of entanglement," Phys. Rev. Lett. **80**, 5524–5527 (1998).

[9]P. A. Miller and S. Sarkar, "Entropy production, dynamical localization and criteria for quantum chaos in the open quantum kicked rotor," Nonlinearity **12**, 419 (1999).

[10]P. A. Miller and S. Sarkar, "Signatures of chaos in the entanglement of two coupled quantum kicked tops," Phys. Rev. E **60**, 1542–1550 (1999).

[11]A. K. Pattanayak, "Lyapunov exponents, entropy production, and decoherence," Phys. Rev. Lett. **83**, 4526–4529 (1999).

[12]D. Monteoliva and J. P. Paz, "Decoherence and the rate of entropy production in chaotic quantum systems," Phys. Rev. Lett. **85**, 3373–3376 (2000).

[13]A. Lakshminarayan, "The classical counterpart of entanglement," arXiv **quant-ph/0107078** (2001).

[14]A. Lakshminarayan, "Entangling power of quantized chaotic systems," Phys. Rev. E **64**, 036207 (2001).

[15]J. Gong and P. Brumer, "Intrinsic decoherence dynamics in smooth hamiltonian systems: quantum-classical correspondence," Phys. Rev. A **68**, 022101 (2003).

[16]J. N. Bandyopadhyay and A. Lakshminarayan, "Entanglement production in coupled chaotic systems: case of the kicked tops," Phys. Rev. E **69**, 016201 (2004).

[17]X.-W. Hou and B. Hu, "Decoherence, entanglement, and chaos in the dicke model," Phys. Rev. A **69**, 042110 (2004).

[18]R. Angelo, S. Vitiello, M. de Aguiar, and K. Furuya, "Quantum linear mutual information and classical correlations in globally pure bipartite systems," Physica A: Statistical Mechanics and its Applications **338**, 458–470 (2004).

[19]G. Casati, I. Guarneri, and J. Reslen, "Classical dynamics of quantum entanglement," Phys. Rev. E **85**, 036208 (2012).

[20]M. V. S. Bonan ça, "Lyapunov decoherence rate in classically chaotic systems," Phys. Rev. E **83**, 046214 (2011).

[21]X. Wang, S. Ghose, B. C. Sanders, and B. Hu, "Entanglement as a signature of quantum chaos," Phys. Rev. E **70**, 016217 (2004).

[22]S. Ghose, R. Stock, P. Jessen, R. Lal, and A. Silberfarb, "Chaos, entanglement, and decoherence in the quantum kicked top," Phys. Rev. A **78**, 042318 (2008).

[23]S. Chaudhry, A. Smith, B. Anderson, et al., "Quantum signatures of chaos in a kicked top," Nature **461**, 768–771 (2009).

[24]C. Neill, P. Roushan, M. Fang, et al., "Ergodic dynamics and thermalization in an isolated quantum system," Nature Phys **12**, 1037–1041 (2016).

[25]A. Lerose and S. Pappalardi, "Bridging entanglement dynamics and chaos in semiclassical systems," Phys. Rev. A **102**, 032404 (2020).

[26]F. Haake, M. Kuś, and R. Scharf, "Classical and quantum chaos for a kicked top," Z. Physik B - Condensed Matter **65**, 381–395 (1987).

[27]N. Lashkari, D. Stanford, M. Hastings, T. Osborne, and P. Hayden, "Towards the fast scrambling conjecture," J. High Energ. Phys. **2013**, 22 (2013).

[28]J. Maldacena, S. Shenker, and D. Stanford, "A bound on chaos," J. High Energ. Phys. **2016**, 106 (2016).

[29]P. Hosur, X.-L. Qi, D. A. Roberts, and B. Yoshida, "Chaos in quantum channels," J. High Energ. Phys. **2016**, 4 (2016).

[30]K. A. Landsman, C. Figgatt, T. Schuster, N. M. Linke, B. Yoshida, N. Y. Yao, and C. Monroe., "Verified quantum information scrambling," Nature **567**, 61–65 (2019).

[31]X. Mi, P. Roushan, C. Quintana, et al., "Information scrambling in quantum circuits," Science **374**, 1479–1483 (2021).

[32]J. M. Deutsch, "Quantum statistical mechanics in a closed system," Phys. Rev. A **43**, 2046–2049 (1991).

[33]M. Srednicki, "Chaos and quantum thermalization," Phys. Rev. E **50**, 888–901 (1994).

[34]M. Rigol, V. Dunjko, and M. Olshanii, "Thermalization and its mechanism for generic isolated quantum systems," Nature **452**, 854–858 (2008).

[35]A. M. Kaufman, M. E. Tai, A. Lukin, M. Rispoli, R. Schittko, P. M. Preiss, and M. Greiner, "Quantum thermalization through entanglement in an isolated many-body system," Science **353**, 794–800 (2016).

[36]C. Murthy and M. Srednicki, "Bounds on chaos from the eigenstate thermalization hypothesis," Phys. Rev. Lett. **123**, 230606 (2019).

[37]A. Einstein, B. Podolsky, and N. Rosen, "Can quantum-mechanical description of physical reality be considered complete?" Phys. Rev. **47**, 777–780 (1935).

[38]E. Schrödinger, "Discussion of probability relations between separated systems," Mathematical Proceedings of the Cambridge Philosophical Society **31**, 555–563 (1935).

[39]W. Myrvold, "Philosophical Issues in Quantum Theory," in *The Stanford encyclopedia of philosophy*, edited by E. N. Zalta, Fall 2022 (Metaphysics Research Lab, Stanford University, 2022).

[40]M. A. Nielsen and I. L. Chuang, *Quantum computation and quantum information: 10th anniversary edition* (Cambridge University Press, 2010).

[41]J. Preskill, *Lecture notes*, https://www.preskill.caltech.edu/ph219/index.html#lecture.

[42]D. F. Styer, M. S. Balkin, K. M. Becker, and others., "Nine formulations of quantum mechanics," American Journal of Physics **70**, 288–297 (2002).

[43]W. B. Case, "Wigner functions and Weyl transforms for pedestrians," American Journal of Physics **76**, 937–946 (2008).

[44]*mutual_info_regression in python package sklearn*, https://scikit-learn.org/stable/modules/generated/sklearn.feature_selection.mutual_info_regression.html.

[45]G. Benettin, L. Galgani, and J.-M. Strelcyn, "Kolmogorov entropy and numerical experiments," Phys. Rev. A **14**, 2338–2345 (1976).

[46]G. Benettin, L. Galgani, A. Giorgilli, and J.-M. Strelcyn, "Lyapunov characteristic exponents for smooth dynamical systems and for hamiltonian systems; a method for computing all of them. part 1: theory," Meccanica **15**, 9–20 (1980).

[47]G. Benettin, L. Galgani, A. Giorgilli, and J.-M. Strelcyn, "Lyapunov characteristic exponents for smooth dynamical systems and for hamiltonian systems; a method for computing all of them. part 2: numerical application," Meccanica **15**, 21–30 (1980).

[48]N. Gisin, "Time really passes, science can't deny that," in *Time in physics*, edited by R. Renner and S. Stupar (Springer International Publishing, Cham, 2017), pp. 1–15.

[49]F. Del Santo and N. Gisin, "Physics without determinism: alternative interpretations of classical physics," Phys. Rev. A **100**, 062107 (2019).

[50]N. Gisin, "Mathematical languages shape our understanding of time in physics," Nat. Phys. **16**, 114–116 (2020).

[51]N. Gisin, "Real numbers are the hidden variables of classical mechanics," Quantum Stud.: Math. Found. **7**, 197–201 (2020).

[52]N. Gisin, "Indeterminism in physics, classical chaos and bohmian mechanics: are real numbers really real?" Erkenn **86**, 1469–1481 (2021).

[53]N. Gisin, "Indeterminism in physics and intuitionistic mathematics," Synthese **199**, 13345–13371 (2021).

[54]F. Del Santo and N. Gisin, "Which features of quantum physics are not fundamentally quantum but are due to indeterminism?" Quantum **9**, 1686 (2025).

[55]D. L. Shepelyansky and A. D. Stone, "Chaotic landau level mixing in classical and quantum wells," Phys. Rev. Lett. **74**, 2098–2101 (1995).

Supplementary Information

S-I Update of Angular Momentum

To compute $\mathbf{J}_1' = U^\dagger \mathbf{J}_1 U$, we first note that $U_{z^2}^\dagger \mathbf{J}_1 U_{z^2}$ is as follows [26]

$$\begin{aligned} U_{z^2}^\dagger J_{1x} U_{z^2} &= \frac{1}{2}(J_{1x} + iJ_{1y})\, \mathrm{e}^{i\frac{\kappa}{j}(J_{1z}+\frac{1}{2})} + \text{h.c.} \\ U_{z^2}^\dagger J_{1y} U_{z^2} &= \frac{1}{2i}(J_{1x} + iJ_{1y})\, \mathrm{e}^{i\frac{\kappa}{j}(J_{1z}+\frac{1}{2})} + \text{h.c.} \\ U_{z^2}^\dagger J_{1z} U_{z^2} &= J_{1z}. \end{aligned} \tag{4.11}$$

On the other hand, $U_{12}^\dagger \mathbf{J}_1 U_{12}$ simply rotates $\mathbf{J}_1$ in the following way

$$\begin{aligned} U_{12}^\dagger J_{1x} U_{12} &= J_{1x} \cos\left(\kappa \frac{J_{2z}}{j}\right) - J_{1y} \sin\left(\kappa \frac{J_{2z}}{j}\right) \\ U_{12}^\dagger J_{1y} U_{12} &= J_{1x} \sin\left(\kappa \frac{J_{2z}}{j}\right) + J_{1y} \cos\left(\kappa \frac{J_{2z}}{j}\right) \\ U_{12}^\dagger J_{1z} U_{12} &= J_{1z}. \end{aligned} \tag{4.12}$$

Combining (4.11) and (4.12), we get

$$\begin{aligned} U_{12}^\dagger U_{z^2}^\dagger J_{1x} U_{z^2} U_{12} &= \frac{1}{2}(J_{1x} + iJ_{1y})\, \mathrm{e}^{i\frac{\kappa}{j}(J_{1z}+J_{2z}+\frac{1}{2})} + \text{h.c.} \\ U_{12}^\dagger U_{z^2}^\dagger J_{1y} U_{z^2} U_{12} &= \frac{1}{2i}(J_{1x} + iJ_{1y})\, \mathrm{e}^{i\frac{\kappa}{j}(J_{1z}+J_{2z}+\frac{1}{2})} + \text{h.c.} \\ U_{12}^\dagger U_{z^2}^\dagger J_{1z} U_{z^2} U_{12} &= J_{1z}. \end{aligned} \tag{4.13}$$

Finally, performing the rotation around the y-axis gives us the following answer for $\mathbf{J}_1' = U^\dagger \mathbf{J}_1 U = U_y^\dagger U_{12}^\dagger U_{z^2}^\dagger \mathbf{J}_1 U_{z^2} U_{12} U_y$,

$$\begin{aligned} J_{1x}' &= \frac{1}{2}(J_{1z} + iJ_{1y})\, \mathrm{e}^{-i\frac{\kappa}{j}(J_{1x}+J_{2x}+\frac{1}{2})} + \text{h.c.} \\ J_{1x}' &= \frac{1}{2i}(J_{1z} + iJ_{1y})\, \mathrm{e}^{-i\frac{\kappa}{j}(J_{1x}+J_{2x}+\frac{1}{2})} + \text{h.c.} \\ J_{1x}' &= -J_{1x}. \end{aligned} \tag{4.14}$$

S-II Calculation of Lyuapunov Exponents

In this section, we apply the procedure of Benettin et al. [25, 45–47] to estimate the Lyuapunov exponents for the kicked top map (4.4). Suppose our initial point is $\mathbf{X}_0 = (\sin\theta_0\cos\phi_0, \sin\theta_0\sin\phi_0, \cos\theta_0)$. First, we pick two independent tangent vectors $(\mathbf{W}_0^{(1)}, \mathbf{W}_0^{(2)})$ at the point $\mathbf{X}_0$ on the unit sphere. These vectors can be chosen at random. For our calculations, we choose

$$\mathbf{W}_0^{(1)} = \begin{bmatrix} \cos\theta_0\cos\phi_0 \\ \cos\theta_0\sin\phi_0 \\ -\sin\theta_0 \end{bmatrix}; \qquad \mathbf{W}_0^{(2)} = \begin{bmatrix} \sin\phi_0 \\ -\cos\phi_0 \\ 0 \end{bmatrix}. \tag{4.15}$$

$\mathbf{X}_i$ is updated through $\mathbf{X}_{i+1} = (F_X[\mathbf{X}_i], F_Y[\mathbf{X}_i], F_Z[\mathbf{X}_i])$ where F_X, F_Y and F_Z are given in eqs. (4.4). The tangent vectors are updated using the map $\mathbf{W}_{i+1}^{(1)} = \mathbf{A}[\mathbf{X}_i]\,\mathbf{W}_i^{(1)}$ where

$$\mathbf{A}[\mathbf{X}_i] = \begin{bmatrix} \partial_{X_i}F_X[\mathbf{X}_i] & \partial_{Y_i}F_X[\mathbf{X}_i] & \partial_{Z_i}F_X[\mathbf{X}_i] \\ \partial_{X_i}F_Y[\mathbf{X}_i] & \partial_{Y_i}F_Y[\mathbf{X}_i] & \partial_{Z_i}F_Y[\mathbf{X}_i] \\ \partial_{X_i}F_Z[\mathbf{X}_i] & \partial_{Y_i}F_Z[\mathbf{X}_i] & \partial_{Z_i}F_Z[\mathbf{X}_i] \end{bmatrix}. \tag{4.16}$$

The procedure to obtain the Lyuapunov exponent is as follows [25]:

1. Evolve the tangent vectors $(\mathbf{W}_{(i-1)s}^{(1)}, \mathbf{W}_{(i-1)s}^{(2)})$ for s time steps to $(\mathbf{W}_{is}^{(1)}, \mathbf{W}_{is}^{(2)})$.

2. Apply the Gram-Schmidt procedure:

$$\alpha_i = |\mathbf{W}_{is}^{(1)}|, \quad \mathbf{V}^{(1)} = \mathbf{W}_{is}^{(1)}/\alpha_i; \tag{4.17}$$

$$\beta_i = |\mathbf{W}_{is}^{(2)} - (\mathbf{V}^{(1)}\cdot\mathbf{W}_{is}^{(2)})\mathbf{V}^{(1)}|, \quad \mathbf{V}^{(2)} = \frac{1}{\beta_i}[\mathbf{W}_{is}^{(2)} - (\mathbf{V}^{(1)}\cdot\mathbf{W}_{is}^{(2)})\mathbf{V}^{(1)}]. \tag{4.18}$$

3. Reinitialize $\mathbf{W}_{is}^{(1)} = \mathbf{V}^{(1)}$ and $\mathbf{W}_{is}^{(2)} = \mathbf{V}^{(2)}$.

Then, for large n, an estimate of the postive Lyuapunov exponent λ is obtained through

$$\lambda^{(n,s)} = \frac{1}{ns}\sum_{i=1}^{n}\ln\alpha_i. \tag{4.19}$$

This expression converges to λ in the limit $n \to \infty$. Fig. 4.8 shows the convergence of Lyuapunov exponents for the four scenarios of Fig. 4.6.

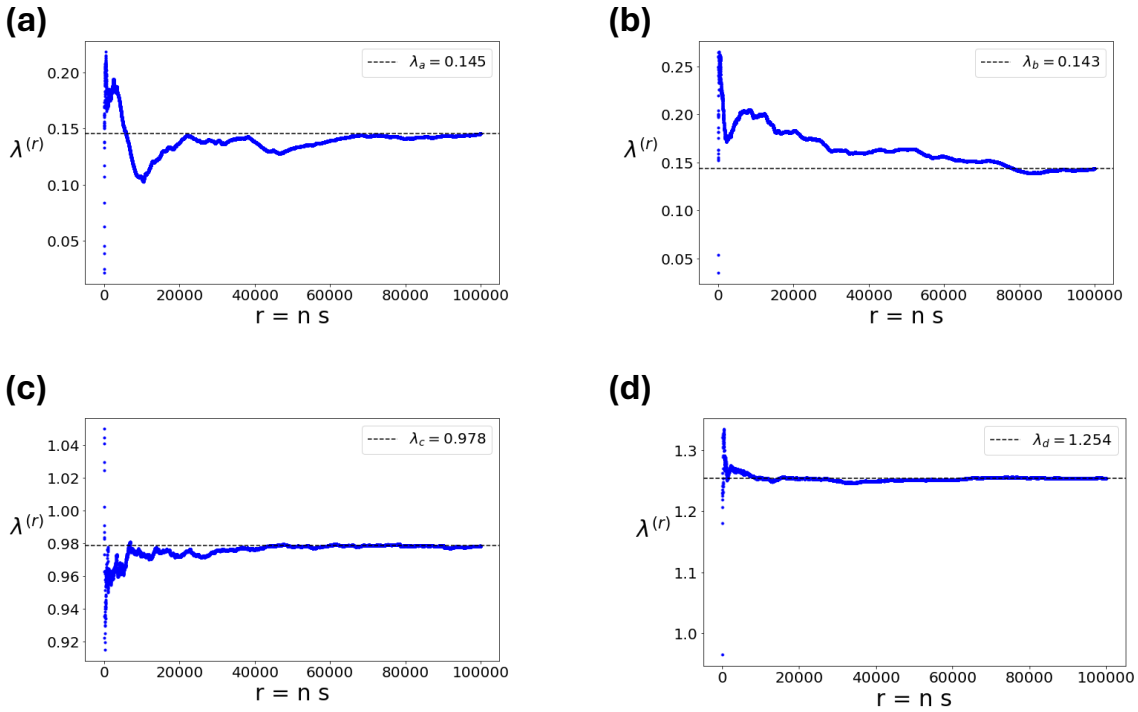

Figure 4.8. Convergence of Lyuapunov exponents. Convergence of Lyuapunov exponents for the four scenarios of Fig. 4.6.: (a) $\kappa = 2.5$, $(\theta_0 = 3\pi/4, \phi_0 = 3\pi/4)$, $s = 5$; (b) $\kappa = 2.5$, $(\theta_0 = 1.0, \phi_0 = \pi/10)$, $s = 5$; (c) $\kappa = 6.0$, $(\theta_0 = 3\pi/4, \phi_0 = 3\pi/4)$, $s = 10$; (d) $\kappa = 8.0$, $(\theta_0 = 3\pi/4, \phi_0 = 3\pi/4)$, $s = 10$.

5. OUTLOOK

The entire edifice of modern physics can be understood as resting upon five pillars: classical mechanics, quantum mechanics, relativity, statistical mechanics, and condensed matter physics. Other modern fields of study such as quantum information and computing, quantum field theory, quantum gravity etc. arise from the interactions between these foundational subjects. Now, the health of any structure depends not only on the individual strength of each of the foundations supporting it but also on their mutual affinity. If the overall organization lacks coherence, the stability of the entire structure is compromised.

For the case of physics, the foundational subjects individually are backed up by rigorous historical developments. Moreover, they generally show a good deal of compatibility with each other. However, there are instances where coherence is missing; and the consequent risk for the overall health of physics makes these instances all the more worthy of our attention. One such incompatibility is found in the well-established discord between classical and quantum mechanics. The *problem of interpretation* in quantum mechanics is a direct manifestation of this divide. Arguably, this is also reflected in the *problem of quantum gravity* – the problem of reconciling quantum mechanics and relativity, which is another example of such incompatibility – since relativity inherits some very prominent features of classical mechanics.

Roughly speaking, physical processes occurring on the scale of our everyday reality are understood using classical mechanics. On the other hand, quantum mechanics is concerned with phenomena on the scale of electrons, atoms and molecules. Quantum mechanics has had extraordinary success in this domain. However, what is quite perplexing about quantum theory is that despite its extraordinary empirical success, a coherent conceptual understanding of the theory has eluded us so far [1], as aptly summarized by Richard Feynman, "I think I can safely say that nobody understands quantum mechanics [2]." This is the *problem of interpretation* in quantum mechanics. This problem essentially reflects a lack of coherence between the "quantumness" of the microscopic realm and the "classicality" of our everyday reality as they are currently formulated.

Table 5.1. A comparison of the mathematical formalisms of classical and quantum mechanics.

	Classical	**Quantum**
Mathematical Framework	Calculus	Functional analysis/Linear algebra (for states) + Calculus (for dynamics)
State	The state for an N-particle system is specified by providing the real-valued positions and momenta for all the N particles i.e. the state is a point in the $6N$-dimensional phase space.	The state of a system is a vector in a Hilbert space that is associated to that system. The Hilbert space $\mathcal{H}$ for an N-particle system is simply the tensor product of the Hilbert spaces $\mathcal{H}_i$ associated to each particle i.e. $$\mathcal{H} = \bigotimes_{i=1}^{N} \mathcal{H}_i.$$
Dynamics	The time evolution of the state $\{x_i, p_i\}$ is given by the Hamilton's equations, $$\dot{q_i} = \{q_i, H\} = \frac{\partial H}{\partial p_i},$$ $$\dot{p_i} = \{p_i, H\} = -\frac{\partial H}{\partial q_i},$$ where H is the Hamiltonian of the system.	The time evolution for any state ψ is given by the Schrödinger's equation, $$i\hbar \frac{\partial \psi}{\partial t} = H\psi,$$ where H is the Hamiltonian (operator) of the system. Alternatively, in the Heisenberg picture, the time evolution for an observable O is given by, $$i\hbar \frac{dO}{dt} = [O, H].$$

Table 5.2. A brief sketch of the prominent distinguishing features across the classical-quantum divide.

Classical	**Quantum**
Derivative	Fundamental
Deterministic	Probabilistic
States are separable	States are nonseparable
Local	Nonlocal?
Waves and particles are distinct categories	Wave-particle duality
No role for observer	Observer is central to physics

One of the main concerns of the question of interpretation is the process of *measurement*. A quantum object under ordinary circumstances can be in a *superposition* of states, but as soon as it comes into contact with a measurement device (belonging to the classical realm) the superposition is lost and the state "collapses" onto a single value for the variable being measured. What is there in a measurement that makes quantum objects lose their "quantumness?" What counts as a measurement and what does not? These are some of the central questions in the foundations of quantum mechanics. Other questions are related to the nature of the *wavefunction* and *non-locality*. For example, is the wavefunction a complete description of the system or is it merely a convenient statistical approximation reflecting our lack of information? Does quantum theory imply non-locality etc. [1]?

Quantum interpretations have been hotly debated for the last century. The icons of 20th century physics such as Neils Bohr, Albert Einstein, Werner Heisenberg, John S. Bell and others have each developed their unique accounts to wrestle with quantum "bizarreness." Nevertheless, the physics community has never appeared to come any closer to a consensus. A common feature, though, of the vast majority of approaches to quantum interpretation is that they were developed in the early years of quantum mechanics. Thus, they do not take into account developments that have come to light only in recent decades, such as those related to *emergence* and *chaos*. In previous chapters, we have already presented some technical investigations into these themes. Now, in this last chapter, our goal will be to outline the possible implications of emergence and chaos for the more comprehensive problem of the *classical-quantum correspondence*.

5.1 A comparison of "Classicality" and "Quantumness"

In order to compare the prominent features of classical and quantum mechanics, it will be helpful to recall the mathematical formalisms of the two theories. Table 5.1 presents a short summary of the two formalisms. Perhaps, the most notable difference between the two is found in their respective definitions of the state of a system. While classical states are simply collections of real-valued variables, the structure of quantum states seems to be a bit

more intricate (see also Fig. 1.1.) It is this elaborate structure of the state that underlies the many "bizarre" features of quantum mechanics.

Keeping Table 5.1 in view, the main distinguishing features of the two theories can be identified as follows:

1. **Derivative vs. Fundamental**

   Quantum mechanics is employed to understand phenomena occurring on the atomic and sub-atomic scales. Classical mechanics, on the other hand, describes physical processes taking place in the everyday world around us. According to the *reductionist* approach prevalent in physics, the physics of a macroscopic object should be completely explicable in terms of the physics of its microscopic constituents. Such a paradigm necessarily implies that quantum mechanics is the more fundamental theory of the two. In this view, classical mechanics becomes merely a limiting case of quantum mechanics.

2. **Deterministic vs. Probabilistic**

   Classical mechanics is widely held to be fully deterministic. Given the present state of a system, all its past and future states can be precisely determined using Hamilton's equations (see Table 5.1.) While a quantum state also evolves deterministically under ordinary circumstances, the process of measurement disrupts this determinism. Quantum mechanics, at best, can only tell us the probabilities of possible outcomes in a measurement.

3. **Separability of states**

   The state of a classical system is completely specified by defining the states of all its constituents. There is essentially no difference between the state of the whole and the states of the parts. On the other hand, the state of a quantum system is, in general, *nonseparabale* in terms of the states of its constituents due to the property of *quantum entanglement*.

4. **Locality**

   Classical mechanics adheres to the principle of locality. According to this principle,

all physical interactions result from local pushes and pulls. That is, objects cannot influence each other from afar, they have to be brought into contact directly or by exchange of information between them through a third body that comes into contact with both of them. However, the issue of locality has been quite controversial in quantum mechanics. Nevertheless, the "wholeness" of composite quantum systems seems to suggest that quantum mechanics supports nonlocality since a measurement performed on one subsystem can immediately "collapse" the state of another subsystem an arbitrary distance away that was entangled to the first subsystem[1]. Einstein famously called this *spooky action at a distance* [1, 3].

5. **Waves vs. Particles**

   In classical mechanics, waves and particles are taken to be distinct categories. A classical particle doesn't exhibit wave-like behavior and vice versa. On the other hand, in quantum mechanics, a single object can demonstrate both particle-like and wave-like characteristics. Matter can act like waves and waves can act like matter. This is known as the *wave-particle duality*.

6. **Role of observer**

   In classical mechanics, the observer has no active role to play in the physics of the system. In quantum mechanics, the interaction of the system with the observer is a crucial component in its physical description. It is precisely this interaction that brings about the "collapse" of the quantum state. However, the set of attributes that constitutes an observer is not clear [1].

This comparison has been summarized in Table 5.2.

5.2 The Quantum Interpretation Problem

As stated earlier, the central concern of the quantum interpretation problem is to make sense of the "quantumness" of the microscopic realm in light of the "classicality" of our everyday experience. Or in other words, to come to terms simultaneously with the two columns

[1]↑Note that quantum entanglement entails both nonseparability and nonlocality.

of Table 5.2 in a coherent worldview. The questions involved in these interpretational issues can be broadly classified into three categories:

1. The first category of questions pertains to the issue of *completeness* of the quantum description of a system. Some examples of these questions are [1]:
   - *Is the quantum state a complete description of a physical system or is it merely an effective statistical representation?*
   - *Is it possible to complement the quantum state with some hidden variables for a more comprehensive account of the system?*
2. The quantum state of a system evolves linearly according to Schrödinger's equation under normal circumstances (see Table 5.1). However, when the system comes into contact with a measurement device, the state of the system suddenly "collapses" to one of the eigenstates of the measured observable in a nonlinear fashion. The friction between these two different kinds of dynamics is referred to as the *measurement problem*. Some issues involved in this problem are [1]:
   - *Why does the linearly evolving quantum state suddenly "collapse" upon measurement?*
   - *Which physical processes can be considered as measurements and what properties must a measurement device possess?*
   - *Is the "collapse" of the quantum state a real physical process?*
   - *What is the role of the observer in "collapse" of the quantum state?*
3. The last set of questions is concerned with *quantum entanglement* i.e. the *nonseparable* and *nonlocal* nature of the quantum state. Examples are [1, 3]:
   - *Does the nonseparability of quantum states imply true nonseparability in the physical world?*
   - *Does quantum mechanics imply nonlocality?*

– *What consequences does quantum nonlocality have for spacetime structure and causality?*

Numerous viewpoints have been put forward in the history of quantum mechanics to address these issues; the most prominent ones being: Copenhagen interpretation, Everett's many-worlds interpretation, Bohmian mechanics and dynamical collapse theories. Nevertheless, all of them undertake the same fundamental strategy. They accept without criticism the classical worldview and try to explain the existence of "quantumness" in light of that; that is they all attempt to justify the second column in Table 5.2 given the first. So, all the activity occurs on the quantum side of the correspondence, and no possibility for a revision of the classical side is considered. While this makes sense in the historical context of these developments since most of these approaches were formulated in the early years of quantum mechanics; however, this attitude towards the classical is no longer tenable today due to the incredible 20th century developments in classical mechanics which have completely revised our understanding of the subject [4, 5].

5.3 Implications of Emergence and Chaos

The revolutions of quantum mechanics and relativity overshadowed all the other 20th century developments in physics. However, while these nascent fields were attracting all the attention, classical mechanics was silently undergoing a revolution of its own [6]. Henri Poincaré had already observed the divergence of the perturbation series for the three-body problem around the end of the 19th century. But it was realized only after the 1950s that these difficulties were due to a fundamentally new type of dynamical behavior in systems satisfying Newton's laws. It was discovered that the vast majority of classical systems exhibited what was called *instability of motion*; two phase space trajectories starting arbitrarily close would diverge greatly in time [4, 5]. This dynamical behavior of classical systems has been termed as *chaos* (see also Sec. 1.3).

The discovery of unpredictability at the heart of classical mechanics, which throughout history has been the cornerstone of scientific determinism, is truly revolutionary. The still prevalent deterministic view of classical mechanics implicitly assumes that the initial condi-

tions for a given system can, in principle, be specified to an infinite precision. However, this assumption has been challenged on both ontological (the nature of reality) and epistemological (the nature of knowledge) grounds [7–15]. Once this assumption is relaxed, it has been argued, the features that have been held to be exclusively quantum (see second column in Table 5.2) start to become visible in classical mechanics too [15].

Max Born is noted to have said as early as 1955 that, "statements like 'a quantity x has a completely definite value' (expressed by a real number and represented by a point in the mathematical continuum) seem to me to have no physical meaning [8]". In fact, this seems to be one of the key messages of *Heisenberg's uncertainty principle* as well; it rules out the possibility of identifying the state of a system with an infinitely precise phase space point. In recent years, Gisin et. al. have presented an information-theoretic approach to this issue. They have argued that real numbers cannot be physically real since they contain an infinite number of bits but a finite volume of space can only hold a finite amount of information [9–15]. However, regardless of whether real numbers are real or not, practically there is no measurement in the world that can determine any physical quantity to infinite precision [7]. Thus, even classical mechanics can, at best, make only probabilistic predictions for the long time behavior of physical systems. Moreover, once a probabilistic interpretation of classical mechanics is admitted, it too has to deal with its own version of the *measurement problem* [10] i.e. to explain how potential outcomes become actual; thus, potentially allowing the observer a more active participation in the physics of the system.

In the absence of infinite precision, classical states are more faithfully represented by *phase space distributions* instead of points in phase space. Naturally, classical mechanics in terms of phase space distributions is expected to show greater affinity with quantum mechanics since both phase space distributions and quantum states admit statistical interpretations. Firstly, such a formulation of classical mechanics is more likely to display wavelike characteristics than the traditional version since phase space distributions stretch across a region of phase space like quantum states. Moreover, phase space distributions by virtue of being probability distributions are nonseparable, by definition i.e. the distribution for a system cannot, in general, be written as a product of the distributions for the corresponding subsystems. This enables the possibility for genuine nonseparability in classical mechanics [15].

We have already discussed some of its implications in Chapter 4. Furthermore, if these correlations are real, the natural question to ask next is whether these correlations survive as the parts of the system are separated in space akin to quantum entanglement [15]. Not only does this give an opportunity to investigate potential nonlocal physics in classical mechanics but an answer to this question can also help in clarifying the conundrums surrounding nonlocality in quantum mechanics.

Finally, we turn to the implications of emergence. We have already discussed that a reductionist approach to physics necessitates the understanding of classical mechanics as a limiting case of quantum mechanics. Emergence is an alternative paradigm that allows for the appearance of genuinely new laws and properties as we move up on the scale of complexity (see Sec. 1.2.) We have already seen examples of this in the study of phases of matter and phase transitions in the preceding chapters. The advantage of this viewpoint for the classical-quantum correspondence is that it doesn't merely reduce one side of the duality into the other; instead it allows us to appreciate classical mechanics as a fundamental description of nature in its own right [16, 17]. Just like chemistry is not mere applied physics, and biology not applied chemistry [16], so classical mechanics is not mere applied quantum mechanics.

Emergence and chaos are still in their infancy despite all the details that have so far been discovered about them. A comprehensive understanding of both the principles of emergence and the manifestations of chaos beyond simple classical systems is still missing. However, the preceding discussion makes clear that whatever little we know about them already demonstrates great promise in addressing the divisions that permeate physics. These new paradigms outline a roadmap to carry these problems beyond old discussions that despite their extraordinary value have ended up deepening these divisions and led to an overall disinterest in these issues as expressed in the popular maxim "shut up and calculate!" In the words of Prof. Ballentine [18]: "The ongoing debates about the interpretation of quantum mechanics have often taken place in forums such as the measurement problem and Schrödinger's cat paradox. I urge that we move beyond those old forums, and consider instead the more general problem of how classical properties emerge from quantum mechanics. Quantum chaos appears as a special case of this general problem, being the study of the emergence of classical

chaos from QM." We hope that the optimism surrounding emergence and chaos is realized and further developments along these lines spark new revolutions in physics.

Bibliography

[1]W. Myrvold, "Philosophical Issues in Quantum Theory," in *The Stanford encyclopedia of philosophy*, edited by E. N. Zalta, Fall 2022 (Metaphysics Research Lab, Stanford University, 2022).

[2]R. P. Feynman, *The character of physical law* (M.I.T. Press, 1967) Chap. 6.

[3]J. Berkovitz, "Action at a Distance in Quantum Mechanics," in *The Stanford encyclopedia of philosophy*, edited by E. N. Zalta, Spring 2016 (Metaphysics Research Lab, Stanford University, 2016).

[4]J. Lighthill, J. M. T. Thompson, A. K. Sen, A. G. M. Last, D. T. Tritton, and P. Mathias, "The recently recognized failure of predictability in newtonian dynamics [and discussion]," Proceedings of the Royal Society of London. Series A, Mathematical and Physical Sciences **407**, 35–50 (1986).

[5]I. Prigogine, *From being to becoming: time and complexity in the physical sciences* (W. H. Freeman and Company, New York, 1980) Chap. 2.

[6]H. S. Dumas, *The kam story* (WORLD SCIENTIFIC, 2014).

[7]C. S. Peirce, *The Collected Papers of Charles Sanders Peirce, Vol. I: The Principles of Philosophy*, English, edited by C. Hartshorne and P. Weiss (Harvard University Press, Cambridge, 1931) Chap. 3: Notes on Scientific Philosophy.

[8]M. Born, "Is classical mechanics in fact deterministic?" In *Physics in my generation* (Springer, New York, NY, 1969).

[9]N. Gisin, "Time really passes, science can't deny that," in *Time in physics*, edited by R. Renner and S. Stupar (Springer International Publishing, Cham, 2017), pp. 1–15.

[10]F. Del Santo and N. Gisin, "Physics without determinism: alternative interpretations of classical physics," Phys. Rev. A **100**, 062107 (2019).

[11]N. Gisin, "Mathematical languages shape our understanding of time in physics," Nat. Phys. **16**, 114–116 (2020).

[12]N. Gisin, "Real numbers are the hidden variables of classical mechanics," Quantum Stud.: Math. Found. **7**, 197–201 (2020).

[13]N. Gisin, "Indeterminism in physics, classical chaos and bohmian mechanics: are real numbers really real?" Erkenn **86**, 1469–1481 (2021).

[14]N. Gisin, "Indeterminism in physics and intuitionistic mathematics," Synthese **199**, 13345–13371 (2021).

[15]F. Del Santo and N. Gisin, "Which features of quantum physics are not fundamentally quantum but are due to indeterminism?" Quantum **9**, 1686 (2025).

[16]P. W. Anderson, "More is different," Science **177**, 393–396 (1972).

[17]R. B. Laughlin, *A different universe: reinventing physics from the bottom down* (Basic Books, New York, 2005).

[18]L. E. Ballentine, "The emergence of classical properties from quantum mechanics: new problems from old," in *Fundamental problems in quantum physics*, edited by M. Ferrero and A. van der Merwe (Springer Netherlands, Dordrecht, 1995), pp. 15–28.